UPPSALA UNIVERSITY

Radio Frontend Integration Techniques: CAD Models and Applications

Dhanesh G-Kurup

December 2000

SIGNALS AND SYSTEMS
UPPSALA UNIVERSITY
UPPSALA, SWEDEN

Submitted to the Faculty of Science and Technology, Uppsala University in partial fulfillment of the requirements for the degree of Technical Licentiate in signal processing.

Abstract

The thesis treats the electromagnetic CAD modeling of some important components useful for designing multilayered radio front-ends and active antennas. The models developed are flexible to use and computationally efficient for optimization together with active circuits. The steps leading to the development of accurate CAD models of antennas suitable for designing active antennas is presented. We considered edge fed and aperture coupled microstrip antennas. The implementation of the program is based on accurate cavity and transmission line models. The CAD models of the antenna are also extended to incorporate micro-machined antennas. Simulations are compared with real experiments.

An efficient method for analysis of slots in the ground plane of transmission lines based on a spectral domain method is also introduced. The application of non-resonant slots in the matching of microwave amplifiers showed improved noise and gain characteristics when compared to traditional transmission line matching techniques. Based on transverse resonance techniques CAD models of sandwich-slotlines were developed. Simulations indicate good performance for silicon based sandwich-slotlines. Nonradiative dielectric (NRD) connectors is another interesting candidate for designing multilayered integrated circuits. The coupling between NRD connectors and microstrip lines is studied by incorporating a transmission line model. Moreover a dual polarised NRD plug based antenna structure is presented.

Flexibility of use is one important design issue considered in the development of the models. Since object oriented programming is used in the development of the CAD models, the models of different components can be coupled by means of powerful optimization tools and active circuit simulators.

Acknowledgements

I wish to express sincere gratitude to my supervisor Professor Anders Rydberg for his guidance and keen interest at all stages during my Licentiate studies. I am also thankful to him for broadening my vision from a narrow field to areas of practical interest. I also wish to express my thankfulness to Professor Anders Ahlén for accepting me as a PhD student in his homely and creative group and also for his valuable remarks for the improvement of the thesis. I also thank Dr. Tommy Öberg and Dr. Mikael Sternad for their interest in the work and the discussions with them. I would also like to thank staff administrator Ylva Johansson, computer system manager Ove Ewerlid, other members of the group, past and present PhD students, thesis students and visiting members for their help and friendship. In particular, I miss the lunch time chats with former PhD student Dr. Staffan Bruce and retired staff members of the group Bjarne Norman and Charlie(Karl-Erik Sundström). Finally I thank my parents, brother and above all my wife Sindhulakshmi for their support.

The work was supported by Personnel Computing and Communications (PCC) research program sponsored by Foundation for strategic research, Sweden.

Contents

Chapter 1

Introduction

1.1 Background

During the last decade the wireless communication market has grown tremendously all over the world [1]. The aim of research and development in wireless communications is to provide low cost access of information of various types to everyone, everywhere and any time. It is expected that in the near future, individuals will be equipped with a single device capable of local computing and communications handled by many equipments today [2][3]. To meet these objectives new frequency bands as well as novel technologies and system architectures will become available. However due to spectrum congestion at lower frequency bands, traditional approaches are being replaced by wideband synthesized solutions up to millimeter-wave frequencies [4]. Such systems are aimed to accommodate different services such as voice and multimedia. Also for incorporating emerging technologies such as adaptive antennas and diversity techniques (to accommodate more number of users in the system and to achieve error free communication) we need a large number of radio channels and novel antennas together with complex signal processing circuits [5]. To meet these challenges, highly efficient devices and integrated circuits with low-power consumption have to be developed. Therefore fundamental assumptions in the signal processing area will have a large impact on the development of the hardware. On the other hand what can be implemented in hardware and what cannot be implemented will be a valuable feedback in the development and optimization of signal processing algorithms subject to constraints imposed by the hardware.

Over the years tremendous progress has been made in digital circuit technology resulting in circuits with low power consumption and large scale integration. On the other hand microwave and millimeter-wave (RF) integrated circuits have not evolved as well as their digital counterparts [6]. One reason for this fact is the domination of the military industry in the past with performance being the major criteria on RF designs rather than system integration. Also for the design of complex RF integration circuits there is a need for proper simulation tools. The design of such RF simulation tools suffers from the large gap between the two key areas into which it can be divided namely the passive and active RF parts. The passive RF part in general comprises components such as antennas, filters and wave guiding structures and the active part consists of circuits such as amplifiers, oscillators and mixers. The design of the passive part, which is in the electromagnetic domain, requires the solution of Maxwell's equations subjected to appropriate boundary conditions, whereas the active part solutions are in the electrical domain involving only Kirchoff's laws. Key issues such as device technology and performance criteria such as harmonic generation, inter-modulation etc. makes the active microwave circuits a vibrant research area of its own. Passive microwave and millimeter-wave circuits, which provide the back-bone and building technique have become important in the last decade due to the increased demand for integrated wireless systems. However due to the electromagnetic nature of passive part, the design process can be a painstakingly slow and computationally intensive which in turn requires powerful computers [7].

The computationally intensive RF part in the electromagnetic domain and the nonlinear/linear circuit part consisting of active devices in the electrical domain, makes the microwave/millimeter-wave design problem into a hybrid nature. Thus, different analytical approaches involving passive and active parts, makes it extremely difficult to avail of attractive optimization techniques. An example of hybrid active-passive design is the class of antennas which integrates active circuits and the antenna, so called active antenna [8]. Apart from the advantage of achieving a small size overall system, active antennas have several attractive features such as superior noise characteristics, high bandwidth and decreased mutual coupling between the antenna elements. Active antennas can also be used for implementing high performance millimeter-wave amplifiers using the technique of spatial power combining [9]. The later application is particularly important because of fundamental limitations of solid state amplifiers at millimeter-wave frequencies. Even though the demand for active antennas is gaining momentum,

proper design tools for integrated active antennas are constrained by non availability of efficient CAD. The reason for the problem is attributed to the fact that the antenna and active circuits are difficult to design in a single environment. Even though the commercially available full wave electromagnetic solvers can solve the antenna part with good accuracy, the fact that they need complex meshing and many iterations makes them difficult to be used for optimization involving the antenna and active circuits.

Another trend in antenna design is the design of multi-tuned and multi-beam antennas of small size. Such antennas fulfill requirements of frequency and space diversity to combat bit error rates in systems such as wireless LAN. The Biconical antenna in [10] is one example where the difference in radiation patterns of different waveguide modes can be used to achieve space diversity using a single antenna. Future systems will need similar antennas of small size and constructing such antennas will be a challenge in antenna design.

The technology of silicon and gallium arsenide (GaAs) based monolithic integrated circuits has been very popular for the development of microwave integrated circuits [11]. The advantages of silicon based integrated circuits are that, they are cheap due to the high volume wafers fabricated and the ability to integrate RF circuits with other analog and digital circuits. The most important advantage of gallium arsenide integrated circuit is the high performance of the RF circuits. Although both silicon and GaAs technology has its own merits and demerits, the addition of a large number of functionalities makes monolithic circuits dense and difficult to design. Several aspects such as mutual coupling between different building blocks then become an issue. Multilayer integration techniques is an effective way of designing high density microwave and millimeter-wave integrated circuits. In a multilayered integrated circuit the RF functionalities are divided among two or more different substrates. Coupling between different substrates are only established at certain specific points and at other places they are effectively isolated using a ground plane.

One of the drawbacks in millimeter-wave RF design is that, critical dimensions of passive devices decrease with increase in frequency. In this context, micro-machining offers a new and unconventional way in designing millimeter-wave and sub-millimeter-wave devices. Usually high ohmic silicon wafers are used as the base material in micro-machining and the wafer is then etched to shape different devices. In [12] horn antennas has been man-

ufactured by micro-machined stacked silicon wafers. A similar technique has been used in [13] for fabricating micro-machined millimeter-wave slot coupled antenna compatible with active devices.

To address the design of these complex passive devices the design tools has not evolved much, since most of the tools today rely on electromagnetic simulators based on full-wave methods which handles large sets of unknowns with poor interfaces to the active circuit simulators. Therefore the success of RF design tools in the future depends on the efficiency of the interface between the passive and active circuit simulators. Also the optimization of the full layout of the complete RF circuit including passive and active device circuits has to be taken care of with less computational complexity. The optimization tools also has to take care of a large number of unknown parameters involving active and passive devices with linear/nonlinear objective functions. Since a large number of parameters of hybrid nature are involved in the design, global optimization tools are preferred.

1.2 Outline of the thesis

This thesis outlines techniques to generate efficient models of some representative passive electromagnetic structures for designing multilayered RF front-ends and its applications. The step by step procedure used in the modeling can be described as follows:

- Divide the complex structure to be analysed into sub components.
- Model each sub component using appropriate electromagnetic theory.
- Combine the electromagnetic models of sub components to form the model of the complex structure.

The advantages of the method lie in its increased computational efficiency compared to the commercial electromagnetic simulators for the same structure. Also the method is more compatible with active device simulators for a large scale optimization of RF circuits. The accuracy of the method can be improved by identification of inferior sub components and replace them with more accurate electromagnetic methods.

The thesis is divided into following chapters.

Chapter 2. deals with efficient antenna modeling techniques useful for designing active antennas. The antennas considered are those compatible with active circuits such as aperture coupled and edge fed microstrip antennas. An efficient method for analysis of micro-machined slot coupled antennas is also introduced. The CAD programs developed are computationally efficient and can be combined with active circuit simulators for optimization.

Chapter 3 describes a spectral domain analysis of slots in the ground plane of a microstrip line. A new way of using the exact wave number of slotlines when describing the electric field in the slot is introduced in this chapter. Further, the application of slots in active circuits area is investigated by matching a microwave amplifier based on non-resonant slot matching. Steps leading to the development of a computer program for analysis of general sandwich-slotlines in a multilayered structures is also described.

Chapter 4 presents an analysis of nonradiative dielectric(NRD) waveguides using a transmission line model. A novel way of using NRD waveguides as plugs in a multilayered structure is introduced. The application of NRD plugs in a multilayered structure is further investigated by designing a dual polarized microstrip antenna.

1.3 Contributions

Parts of the material in this thesis are presented in the following publications:

Chapter 2: Dhanesh G-Kurup and Anders Rydberg, " Equivalent network models for active antenna design", *Conference proceedings EMB 98-Electromagnetic computations for analysis and design of complex systems 1998*, Linköping, Sweden, November 17-18, pp.195-202.

Erik Öjefors, Jan Lindblom, Anders Rydberg, Dhanesh G-Kurup, Ylva Bäcklund, Federico Municio, Tapani Ryhanen and Hans Otto Scheck, "High gain micro-machined slot coupled patch antennas for 60 GHz WLAN application", *Proceedings COST-268*, Rennes, France, October 1-3, 2000.

Chapter 3: Dhanesh G-Kurup and Anders Rydberg "Design of microwave amplifiers using non resonant slot matching", *Electronics letters*, Vol.36, No. 7, March 2000, pp.602-603.

Dhanesh G-Kurup and Anders Rydberg "Slots as impedance transformers in microwave circuit designs", *Symposium proceedings GHz2000*, Göteborg, Sweden, March 13-14, 2000, pp.407-410.

Chapter 4: Dhanesh G-Kurup, Anders Rydberg and Thomas Johansson, "Nonradiative dielectric interconnect for compact radio front ends", *Conference proceedings RVK 99-Radio Vetenskap och Kommunications*, Karlskrona, Sweden, June 14-17.

Dhanesh G-Kurup and Anders Rydberg, "Dielectric connectors for multilayered RF integration ", *Microwave and optical technology letters*, Vol.23, No. 4, November 1999, pp.230-233.

Chapter 2

CAD models for design of active microstrip antennas

In this chapter, the CAD for active microstrip antennas using accurate cavity and transmission line models is presented. The antenna candidates considered in the development of CAD tools are single substrate and aperture coupled microstrip antennas [14]. The flexibility of the programs developed is demonstrated by studying the conventional feeding techniques as well as inset fed and offset feeding techniques. Inset and offset feeding technique provide a wide range of impedance characteristics suitable for the active antenna design. The theory is extended to include H-slot coupled silicon micro-machined antennas and the accuracy of the program is tested by comparing the simulated and experimental results.

Efficient CAD for design of active antennas needs less computationally intensive design tools for the antenna part. Although the fullwave simulators based on numerical electromagnetic methods such as finite elements and moment method are accurate, the interface between active circuit simulators and those methods are inefficient because of computational complexity for the analysis of the antenna. On the other hand for full optimization and tradeoffs between active circuit parameters and the antenna we need accurate and computationally efficient CAD for simulation of the antenna part. The most important property which makes microstrip antennas ideally suited for active antenna designs is that the fabrication can be done with the same printed circuit technology used for active circuits. Microstrip antenna also offers advantages such as small size, lightweight, low cost and conformity

to a given surface. Since active circuits performs well on high permittivity substrates due to its decreased radiation loss and antenna part performs well on lower permittivity substrate, aperture coupled antennas [15] offers the additional advantage of using higher permittivity substrate for active circuits and lower permittivity substrate for antenna. Thus the radiative part and non radiative part can be isolated by ground plane. These properties helps in achieving improved bandwidth and radiation performance for aperture coupled microstrip antenna compared to single layered case.

The robustness of the CAD for active antenna depends on the method followed in the analysis of the active circuits including antenna. The most computationally intensive part in the design is the analysis of the antenna and passive components. One way to tackle the problem for passive components is to have a dictionary of models of passive circuits derived using neural networks [16] and full wave simulations.

We can conclude therefore that the performance of active antenna simulator depends on the method followed and the efficiency with which the block diagram, shown in Figure 2.1, is realized. Analysis of microstrip antennas

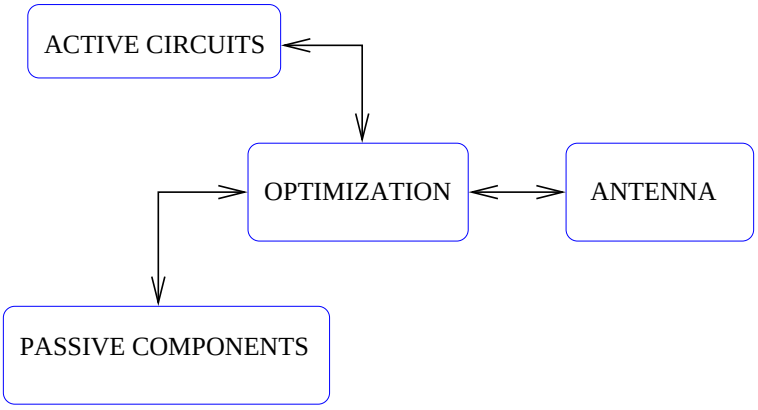

Figure 2.1: Simulation of the Active Antenna.

in commercially available simulators are usually based on the method of moments and finite element methods. These methods are computationally slow and memory intensive, which makes them difficult to use in designing active antennas. Transmission line models in [17],[18] and cavity models [19] of microstrip antenna mitigates most of the draw backs of full wave electromagnetic solvers as they are reasonably accurate and computation-

ally efficient. They are also easily adaptable to active circuit simulators. The flexibility of the transmission line and cavity models followed in this chapter is demonstrated by coupling the programs developed to a Genetic algorithm optimization tool in [20].

2.1 Microstrip antenna on a single substrate

2.1.1 Transmission line model

Consider a microstrip antenna of length L and width W and its transmission line model shown in Figure 2.2. Let the feed point of the antenna be (x_0, y_0). In the transmission line model, the microstrip antenna is represented by sec-

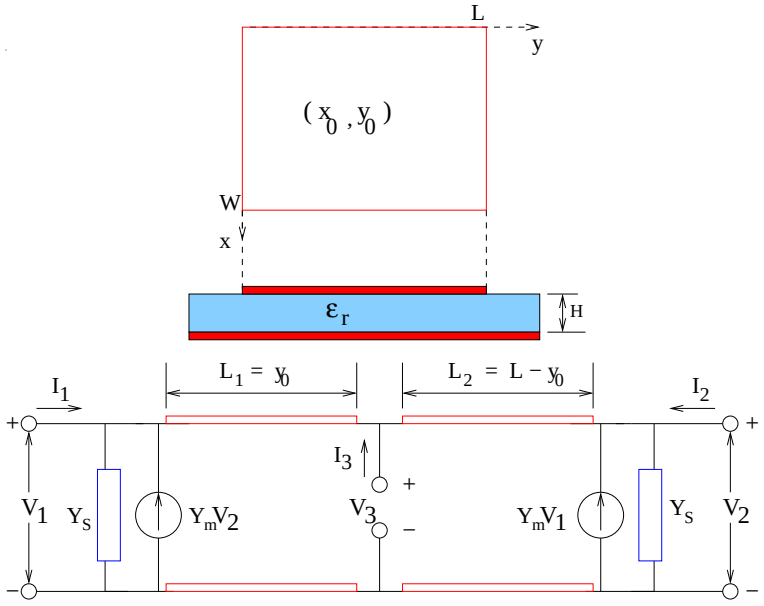

Figure 2.2: Rectangular microstrip patch and its transmission line model.

tions of transmission lines of length L_1 and L_2, where L_1 and L_2 depends on feed position. For example, if the patch is edge fed ($x_0 = W/2$, $y_0 = 0$) then $L_2 = L$ and $L_1 = 0$ also $I_2 = I_3 = 0$. Following the transmission line model [17] the radiation from the antenna is analyzed as the radiation from two TE exited narrow aperture of length W_{eff} and width $\triangle L$ in the infinite ground, where W_{eff} and $L + 2\triangle L$ are the effective width and length of microstrip patch respectively. It is to be noted that $\triangle L$ and $W_{eff} - W$ are accounted for by the fringing fields of the patch. The narrow aperture

located at the ends of patch, $y = 0$ and $y = L$ has self and mutual admittance, $Y_s = G_s + jB_s$ and $Y_m = G_m + jB_m$ respectively. The expression for the radiation conductance, G_s of each slot can be derived as [17],

$$G_s = \frac{1}{\pi^2 \eta_0} \int_0^{\pi} \int_0^{\pi} \frac{\sin^2 (w \cos\alpha/2)}{\cos^2 \alpha} \frac{\sin^2 (s \sin\alpha \cos\beta/2)}{(s \sin\alpha \cos\beta/2)^2} \, d\alpha \, d\beta \qquad (2.1)$$

where $w = k_0 W_{eff}, s = k_0 (L + \triangle L), k_0$ is the free space wave number corresponding to the operating frequency. Numerical expression for (2.1) is given in [21]. The radiation suceptance B_s of the slots is the reactance offered by open microstrip line of length ΔL and propagation constant β_{eff} given by,

$$B_s = \tan (\beta_{eff} \triangle L) / Z_c \qquad (2.2)$$

where $\beta_{eff} = k_0 \sqrt{\epsilon_{eff}}$, is the effective propagation constant, ϵ_{eff} is the effective dielectric constant of the substrate and Z_c is the characteristic impedance of the microstrip patch. The method followed in finding the mutual conductance is by first deriving an auxiliary coupling function, F_g between the slots as,

$$F_g = J_0(l) + \frac{s^2}{24 - s^2} J_2(l) \qquad (2.3)$$

where $l = k_0(L + \Delta L)$, is the normalized distance between the center of the slots. G_m is can be derived as,

$$G_m = G_s F_g \qquad (2.4)$$

In (2.3) $J_m(x)$ is the Bessel function of the first kind and order m. It has been shown in [17] that the mutual suceptance of the slots can be approximated as,

$$B_m = B_s \frac{\pi}{2} \left(\frac{Y_0(l) + \frac{s^2}{24 - s^2} Y_2(l)}{\ln(s/2) + C_e - 1.5 + \frac{s^2/12}{24 - s^2}} \right) \left(1 - e^{-.21w}\right) \qquad (2.5)$$

where $Y_m(x)$ is the Bessel function of the second kind and order m. C_e is the Euler's constant.

The accuracy of the transmission line model is thus dependent on the accuracy with which the parameter set $\{W_{eff}, \epsilon_{eff}, Z_c, \Delta L\}$ is derived. Over the years considerable effort has been put for finding these parameters, for

microstrip line as well as microstrip antenna [18][21]. In the case of a microstrip antenna the results in [21] is very accurate. For edge fed microstrip antennas the input admittance measured to a microstrip line of width w_m can be derived from the transmission line model of Figure 2.2 as,

$$Y_{in} = Y_s\left(1 - \frac{W_m}{W_{eff}}\right) + \frac{Y_c^2 - Y_m^2 + Y_s Y_c \coth(\gamma_p L) - 2Y_m Y_c / \sinh(\gamma_p L)}{Y_s + Y_c \coth(\gamma_p L)} \tag{2.6}$$

where $Y_c = 1/Z_c$, $Y_s = G_s + jB_s$ and $Y_m = G_m + jB_m$. The term $Y_s\left(1 - \frac{W_m}{W_{eff}}\right)$ accounts for the change in input impedance due to the finite width W_m of microstrip line.

2.1.2 Cavity model

In the cavity model analysis the microstrip patch antenna is modeled as a rectangular cavity bounded by a ground plane, a patch and four magnetic walls. The improved cavity model in [19] is very flexible and can be easily adopted to a CAD program for active antenna.

In the cavity method all the losses in the patch are used to evaluate an effective loss tangent δ_{eff}. The losses are the radiation loss P_r, the dielectric loss P_d and the conductor loss P_c. δ_{eff} is then given by,

$$\delta_{eff} = \frac{P_r + P_d + P_c}{\omega(w_e + w_h)} \tag{2.7}$$

where w_e and w_m are the electric and magnetic energy stored in the cavity and $\omega = 2\pi f$. Near the resonant frequency the effective loss tangent can be analytically derived as,

$$\delta_{eff} = \delta + \frac{\triangle}{H} + \frac{64}{3} K \gamma^{1.5} \frac{H}{a}(F_1 + F_2) \tag{2.8}$$

$$F_1 = 1 - 4.72\gamma(1 + .14K) + 10.85\gamma^2(1 + 0.27K + 0.034K^2)$$
$$F_2 = -8.29\gamma^3(1 + 0.42K + 0.2K^2 + 0.015K^3)$$
$$K = (\frac{a}{b})^2, \gamma = (\frac{b}{\lambda_0})^2$$

where δ and $\triangle$ are the loss-tangent and skin depth of the substrate, $a = W_{eff}$ and $b = L + 2\triangle L$. W_{eff} and $\triangle L$ are calculated as described in

[21].

The final expression of the input impedance can then be computed using the solutions of the TM_{p0} modes of the patch [22]. From the top view of the patch and feed point (x_0, y_0) shown in Figure 2.2, the electric field (assumed to have only z- component) can be derived as,

$$E_z(x, y^{'}) = \sum_{p=0}^{\infty} A_p \cos\left(\frac{p\pi x}{a}\right) \frac{\cos(\beta_p(y^{'} - v))}{\cos(\beta_p v)} \tag{2.9}$$

where $y^{'} = y - y_0$ and $v = b - y_0$, $y^{'} > 0$ and $v = -y_0$ for $y^{'} < 0$. y_0 and x_0 are the inset and offset positions of the feed. A_p is the solution of time harmonic electromagnetic fields with the assumption that electric source is of density J. The expression for effective propagation constant β_p can be written as,

$$\beta_p^2 = k_0^2 \epsilon_r (1 - j\delta_{eff}) - (p\pi/a)^2 \tag{2.10}$$

For microstrip line feed the input impedance, Z_i of the patch, can be derived by modeling the feed as a current sheet with the density $J = I/d$, located between $x_0 + d/2$ and $x_0 - d/2$, where d is the effective width of microstrip line and I is the intensity of the current in the feed. Then A_p $(p > 0)$ can be written as,

$$A_p = \frac{4}{\pi p} F_{po} \cos\left(\frac{p\pi x_0}{a}\right) \tag{2.11}$$

A_0 is given by,

$$A_0 = \frac{d}{a} F_{po} \tag{2.12}$$

where,

$$F_{po} = \frac{j\omega\mu_0 J}{\beta_p \left[\tan(\beta_p[b - y0])) + \tan(\beta_p[b - y_0])\right]} \tag{2.13}$$

The input impedance of the patch can then be derived as,

$$Z_i = -\frac{-H}{Id} \int_{x_0 - d/2}^{x_0 + d/2} E_z(x, 0)\, dx \tag{2.14}$$

It has been noted that to get the correct results for edge fed patch $x_0 = 0$ should be changed to $x_0 = \triangle L$. This accounts for the fringing fields at the ends of the patch.

2.1.3 Results

Figure 2.3 shows the simulated results of cavity and transmission line models of a microstrip line fed antenna. It can be seen that there is close agreement between the return loss for both the methods and the experimental results of [17]. The maximum return loss for the transmission line model is at the frequency 2.99814 GHz and for cavity modal at 3.002 GHz. The return loss

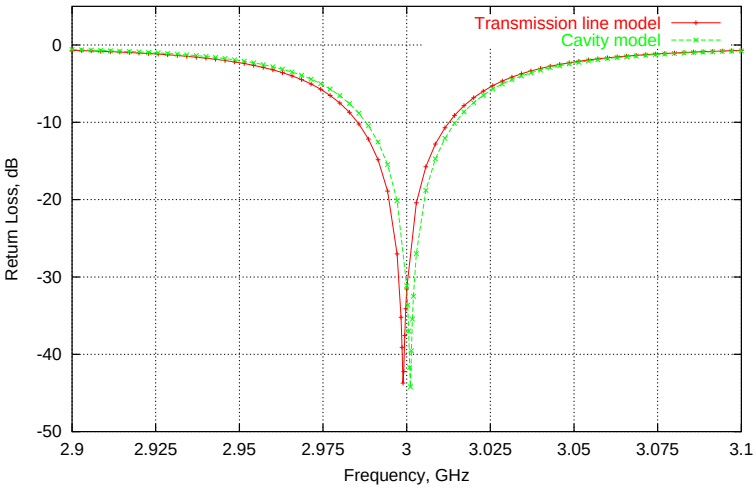

Figure 2.3: Return Loss characteristics of rectangular microstrip antenna: W=33.165mm, L=33.147mm, H=0.7874mm. ϵ_r=2.2,$\tan\delta$ = 0.0009 (Quarter wave microstrip transformer (width=0.473mm,length=20mm.) Reference: 50Ω.)

at these frequencies are 40.8398 dB for transmission line model and 43.0408 dB for cavity model. The frequencies for maximum return loss has a slight deviation from the zero reactance frequency for the patch which are 2.9975 for transmission line model and 3.001 for cavity model. For the properly tuned antenna these factors should be same. The deviations in the present case is because of the lumped reactances due to the transitions in width. As a further improvement of the program, analytical expressions given in [23][24] may be included.

Figure 2.4 shows the simulated results of the normalized patch resistance and reactance as a function of frequency. It can be seen that results of the transmission line model and cavity model agree well.

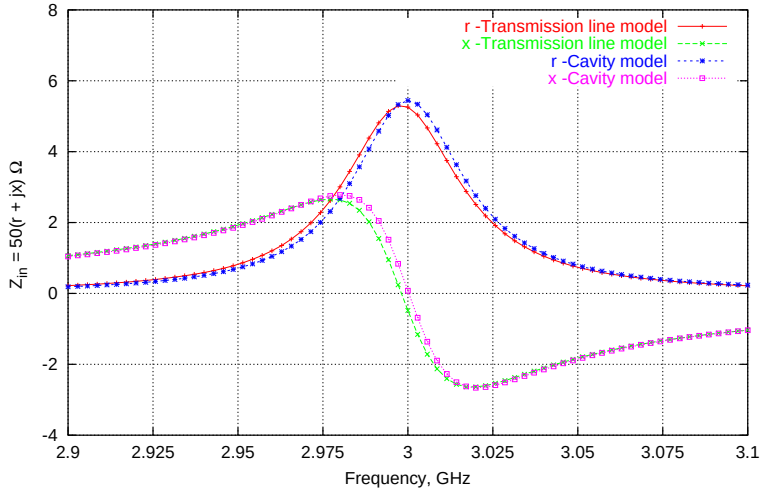

Figure 2.4: Normalized resistance and reactance at the the patch: Data same as that of Figure 2.3.

For the active antenna designs it is desirable to avoid matching circuits between the antenna and the amplifiers as they tend to increase the losses and decrease the operating bandwidth. Figure 2.5 shows the simulated results of the input impedance of a patch as a function of the feed inset from end of the patch. The feed is centered across the width. The simulations are carried out using the cavity model. It can be seen that the input resistance of the patch varies widely as a function of the inset position. It is also seen from Figure 2.5 that the reactance variation is less compared to the change in resistance. This indicate the possibility of achieving a match for the output impedance of an amplifier without the need of extra transmission line matching circuits. However care should be taken to minimise perturbations in the radiation pattern due to the inset. Figure 2.6 shows the cavity model analysis of offset fed microstrip antenna as a function of offset from the center of the patch width. The antenna parameters are same as that of Figure 2.5. It can be seen that for the offset fed case, the variation of resistance is less compared to the variation in reactance. The frequency for zero crossing of reactance is 2.203133 GHz at an offset of 41.8mm. The same antenna has been investigated experimentally for the offset of 41.8mm or 30.2mm from end of the patch in [25] and we see that the simulated and experimental results agree well.

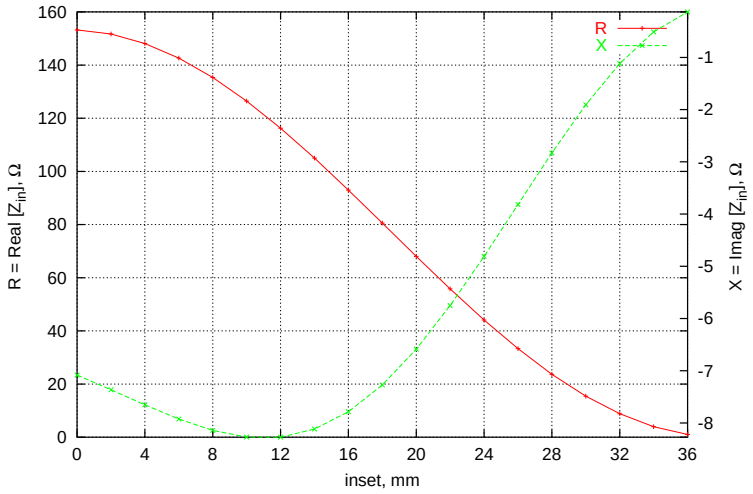

Figure 2.5: Effect of the inset feeding on input impedance Z_{in} of a microstrip patch: (Microstrip line 50Ω width=4.3mm) Patch Data: W=144mm, L=76mm, H=1.59mm, ϵ_r=2.62, $\tan\delta$=0.001.

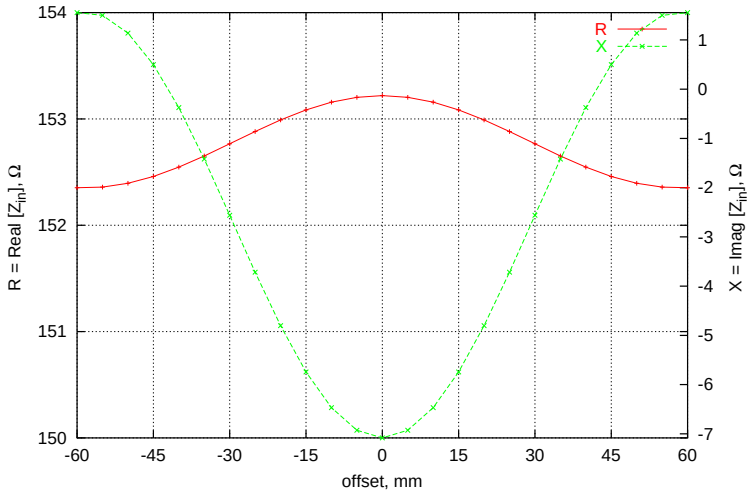

Figure 2.6: Effect of offset feeding: All data same as that of Figure 2.5.

2.2 Aperture Coupled Microstrip Antennas

2.2.1 Transmission line model

The geometry of an aperture coupled microstrip antenna is shown in Figure 2.7. Instead of exiting the patch at the patch surface for the case of single

layered antennas, the excitation of the aperture coupled patch antennas is done via a rectangular aperture in the ground plane. By representing the resonant behavior of a patch operating in the TEM mode it is possible to simplify the analysis of the aperture coupled patch antennas using a transmission line model [26].

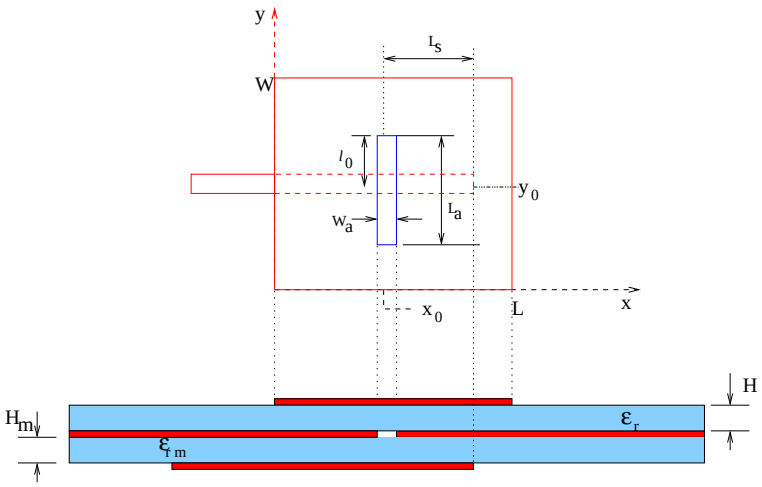

Figure 2.7: Aperture Coupled Patch.

To apply the transmission line model for the aperture coupled patch antennas, the steps followed are,

- An accurate transmission line model is used to derive the self susceptance, $Y = G + jB$ at the edges of the patch. Neglecting mutual coupling between the slots G and B can be taken as G_s and B_s respectively (2.1) and (2.2).
- The aperture impedance, Y_{ap} is represented as a parallel combination of two shorted slotlines of lengths $L_a - l_o$ and $L_a + l_o$ where l_o is the microstrip line offset from the center of aperture. The slotline wave number k_a is evaluated using a modification of Cohn's method [27] as described in [22][28] (see Chapter 3).
- The discontinuity of voltages in the patch and the microstrip line feed at the aperture are represented by two transformers of turns ratio N_1 and N_2.

Thus the transmission line model of the patch can be represented as shown in Figure 2.8. The aperture admittance can be written as the admittance

of two short circuited slotlines connected in parallel as,

$$Y_{ap} = -jY_{0S}\frac{\tan(k_a(L_a/2-l_o))+\tan(k_a(L_a/2+l_o))}{\tan(k_a(L_a/2+l_o))\tan(k_a(L_a/2-l_o))} \tag{2.15}$$

Y_{0S} is the characteristic admittance of a slotline of width W_a. It is to be noted that maximum time for the computations is devoted to the evaluation of k_a and Y_{0S} which involves the application of the transverse resonance technique. More about k_a and Y_{0S} will be addressed in chapter 3. The electric field distribution using the exact slot wavelength of a rectangular slot (k_a), can be written as [29],

$$\mathbf{E}^a = \frac{V_0}{W_a}\frac{\sin\left(k_a(L_a/2-|y-y_o|)\right)}{\sin\left(k_aL_a/2\right)}\hat{x} \qquad |x| \le W_a/2 \quad |y| \le L_a/2 \tag{2.16}$$

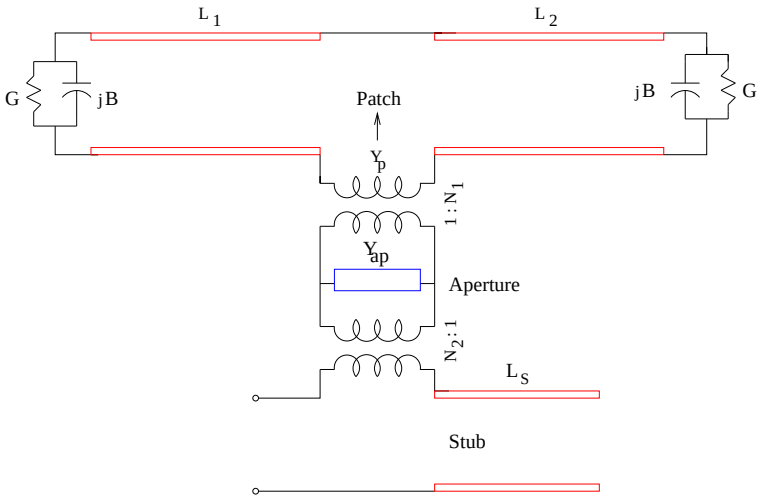

Figure 2.8: Network Model of Aperture Coupled Patch.

In the transmission line model shown in Figure 2.8, L_1 and L_2 for the center fed patch are given by, $L_1 = L_2 = (L - W_a)/2 + \triangle L$. The transformer ratios N_1 and N_2 are given by,

$$N_1 = \frac{L_a}{W_{eff}} \tag{2.17}$$

where W_{eff} is the effective width of the patch.

$$N_2 = \int_{x=-W_a/2}^{W_a/2}\int_{y=-W_{eff}^m/2}^{W_{eff}^m/2} H_y^m\frac{E_a^x}{V_0}\,dx\,dy \tag{2.18}$$

where H_y^m is the y magnetic field component in the microstrip stub approximated by,

$$\mathbf{H}^m = \frac{1}{\sqrt{W_{eff}^m H_{stub}}}\hat{y} \qquad |y| \leq W_{eff}^m/2 \tag{2.19}$$

where W_{eff}^m is the effective width of microstrip line. For the usual case when $L_a > W_{eff}^m$, N_2 is given by,

$$N_2 = \frac{2}{\sqrt{W_{eff}^m H_m}} \frac{\cos(k_a(L_a - W_{eff}^m)/2) - \cos(k_a L_a/2)}{k_a \sin(k_a L_a/2)} \tag{2.20}$$

Finally the input impedance of the antenna at the reference plane which is the center of the slot can be written as,

$$Z_{in} = \frac{N_2^2}{N_1^2 Y_p + Y_{ap}} - jZ_{0M}\cot(k^m L_s) \tag{2.21}$$

In (2.20) and (2.21) L_s,k^m, Z_{0M} are the length, wave number and characteristic impedance of the stub. Y_p is the total patch impedance. Y_p can be calculated as series combination of input impedances due to load $Y = G+jB$ at the ends of transmission line sections L_1 and L_2 (see Figure 2.8).

2.2.2 Cavity model

Consider the aperture coupled patch antenna shown in Figure 2.7. To apply the cavity model analysis for aperture coupled patch antennas[29] the equivalence principle is applied to find the magnetic current density. The assumed slot field distribution is the same as given in (2.16).

$$\mathbf{J}_m = J_y^m\hat{y} = \frac{2V_0}{HW_a}\frac{\sin\left(k_a(L_a/2 - |y - y_o|)\right)}{\sin\left(k_a L_a/2\right)}\hat{y} \qquad |x| \leq W_a/2 \quad |y| \leq L_a/2 \quad 0 \leq z \leq H \tag{2.22}$$

For TM_{mn} modes, the time harmonic field equations with a magnetic source J_m^y results in the following expression for the y-component of the magnetic field H^y.

$$H^y = \sum_m \sum_n A_{mn} \sin\left(m\pi x/a\right) \cos\left(n\pi y/b\right) \tag{2.23}$$

where $a = L + 2\triangle L$ and $b = W_{eff}$. The coefficients can be found using the field equations of TM^z modes as,

$$A_{mn} = \frac{j\omega\epsilon \int_{x=0}^{a}\int_{y=0}^{b} J_m^y \sin(m\pi x/a)\cos(n\pi y/b)\,dx\,dy}{\beta_{mn}^2 \int_{x=0}^{a}\int_{y=0}^{b} \left(\sin(m\pi x/a)\cos(n\pi y/b)\right)^2\,dx\,dy} \tag{2.24}$$

The coefficients A_{mn} for the single mode is given in [29], and for all the modes similar expression can be derived using (2.24). The expression for the effective propagation constant β_{mn} can be written as,

$$\beta_{mn}^2 = k_0^2\epsilon_r(1 - j\delta_{eff}) - \left((m\pi/a)^2 + (n\pi/b)^2\right) \tag{2.25}$$

The effective loss tangent δ_{eff} remains the same as that of cavity model for single layer case and is given by (2.8) with $b = L + 2\triangle L$ and $a = W_{eff}$.

The integrals in (2.24) can be analytically solved as,

$$A_{mn} = \frac{j\omega\epsilon}{\beta_{mn}^2}\frac{A^{(2)}}{A^{(1)}} \tag{2.26}$$

where,

$$A^{(1)} = \frac{ab}{4}(1 + sinc(2n\pi) - sinc(2m\pi) - sinc(2n\pi)sinc(2m\pi)) \tag{2.27}$$

$$A^{(2)} = \frac{-2F_m b^2 k_a \cos(n\pi y_0/b)\left[cos(k_a L_a/2) - cos(n\pi L_a/(2b))\right]}{(n\pi)^2 - (k_a b)^2} \tag{2.28}$$

$$F_m = \frac{-2\sin(m\pi x_0/a)sinc(m\pi W_a/(2a))}{H\sin(k_a L_a/2)} \tag{2.29}$$

The admittance, Y_p of the radiating patch offered to the source J_m^y can be written as,

$$\begin{aligned} Y_p &= -\iiint_V H^y J_m^y\,dv \\ &= -\sum_m\sum_n H A_{mn} A^{(2)} \end{aligned} \tag{2.30}$$

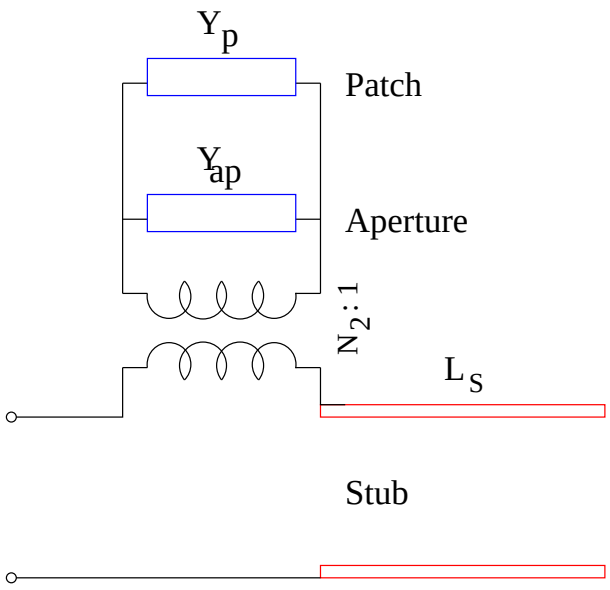

Figure 2.9: Cavity Model representation of Aperture Coupled Patch.

The input impedance of the antenna becomes,

$$Z_{in} = \frac{N_2^2}{Y_p + Y_{ap}} - j Z_{0M} \cot(k^m L_s) \tag{2.31}$$

The analysis of the transformer ratio N_2 remains the same as that of the transmission line model, see (2.20). The cavity model of aperture coupled antenna can therefore be represented as shown in Figure 2.9.

2.2.3 Results

Figure 2.10 shows the cavity model and the transmission line model analysis of an aperture coupled antenna. It can been seen that the resonance frequency, resistance and reactance variations agree well with experiments of [30]. The difference in resonance frequency between the cavity model analysis compared to transmission line model is less than 0.02GHz.

Figure 2.11 shows the sensitivity on the resonant frequency as a function of slot length. It can be seen that for a change of about 5mm in slot length, the resonant frequency shifts by about 100MHz. The variation in resonant frequency with slot length agree well with the results in [30] for the same antenna. Figure 2.12 shows corresponding variation of resistance at resonance

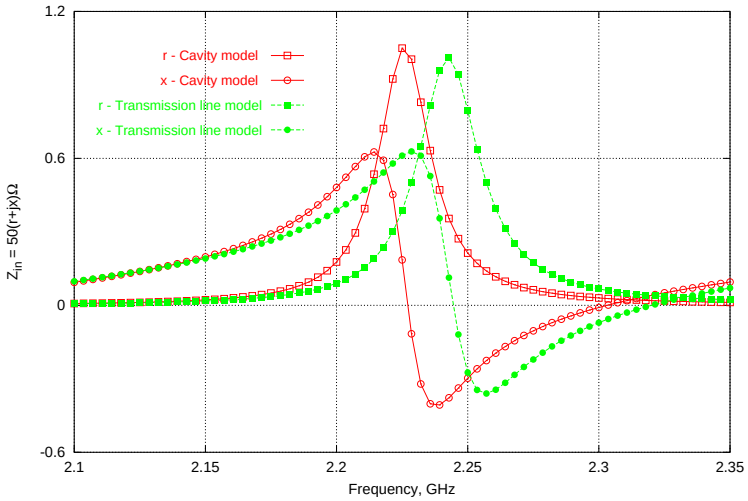

Figure 2.10: Input impedance of an aperture coupled patch, Patch data: W=30mm, L=40 mm, ϵ_{r1} =2.54, H=1.6mm. Stub data: ϵ_{r2}=2.54, H_m=1.6mm, W_m=4.42mm, L_s=20mm. Aperture data: W_a=1.55mm, L_a=11.2mm (See figure 2.7.)

with the change in slot length. It can be seen that there is good agreement between the resistance at resonance between cavity and transmission line models with the experiments of [30].

Figure 2.13 shows the effect of an offset in the slot position measured from the center along the length of the patch. The dimension of the parameters are same as that of Figure 2.10 and the frequency for the simulation is resonant frequency of Figure 2.10. It can be seen that resistance and reactance has large variations with the offset. As has been indicated under single substrate case these variations are useful in matching active circuits. It can be seen that for the zero offset case the resistance and reactance are same as that of Figure 2.12

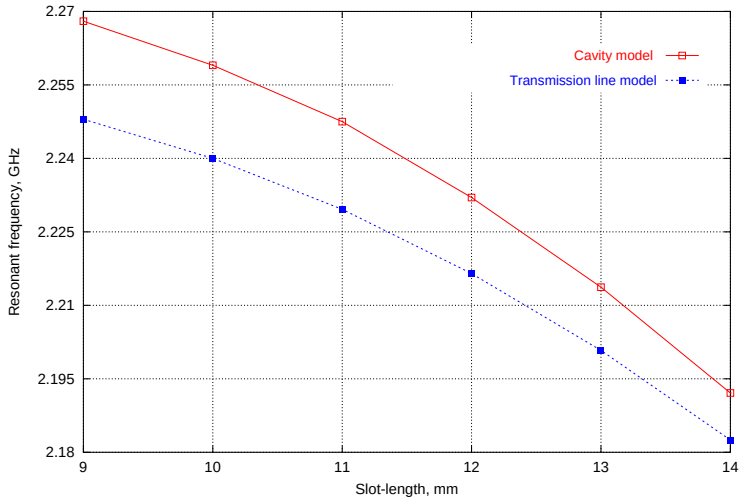

Figure 2.11: Aperture coupled antenna: sensitivity of resonant frequency with respect to slot length: W_m=4.95mm. Other data same as that of Figure 2.10.

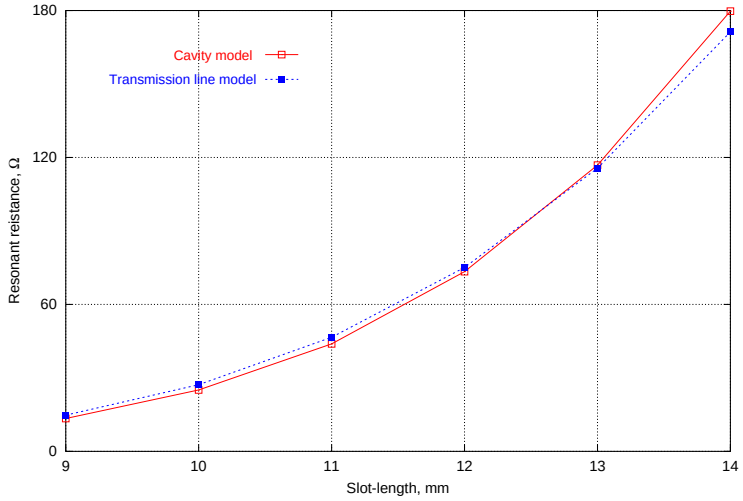

Figure 2.12: Aperture coupled antenna: Sensitivity of the input resistance at resonant frequencies with respect to slot length: All the data same as that in Figure 2.11.

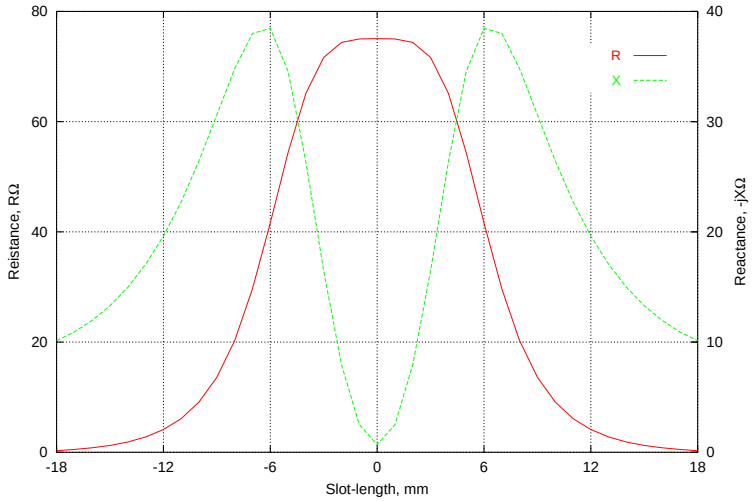

Figure 2.13: Aperture coupled antenna: Sensitivity of input impedance with respect to offset in slot position, slot-length=12mm, all other data same as that of Figure 2.10.

2.3 Micro-machined aperture coupled microstrip antenna

The micro-machined antenna realised on silicon wafer is shown in Figure 2.14. It consists of two high resistivity silicon wafers one on each side of

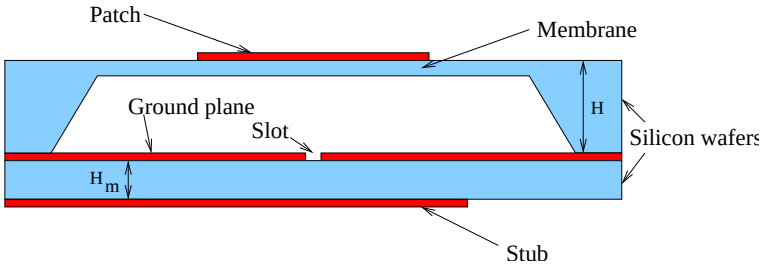

Figure 2.14: Micro-machined H-slot coupled microstrip antenna.

a ground plane. The radiating patch is etched on the top wafer and the microstrip line is etched on the bottom wafer. The microstrip line couples to the radiating patch through an aperture. To increase the coupling and to reduce the back-lobe from the aperture, an H-shaped aperture is used

as shown in Figure 2.15. Part of the silicon in the top wafer is etched away to form an air filled cavity. As shown in Figure 2.14, the top side of the cavity is separated from the metalisation forming the patch by a thin silicon membrane. This procedure in fabrication helps in achieving a good electrical performance of the antenna since the effective ϵ_r of the top substrate is reduced. Also the thin membrane provides mechanical support for the metalisation forming the patch. If the processing for the top wafer uses wet etching, then the cavity will get a pyramidal shape where the angle between the side walls and the bottom surface is defined by the crystal planes. In the antenna considered dry etching has been used which gives the cavity a rectangular shape. The detailed processing steps followed in the fabrication of the antenna is discussed in [31].

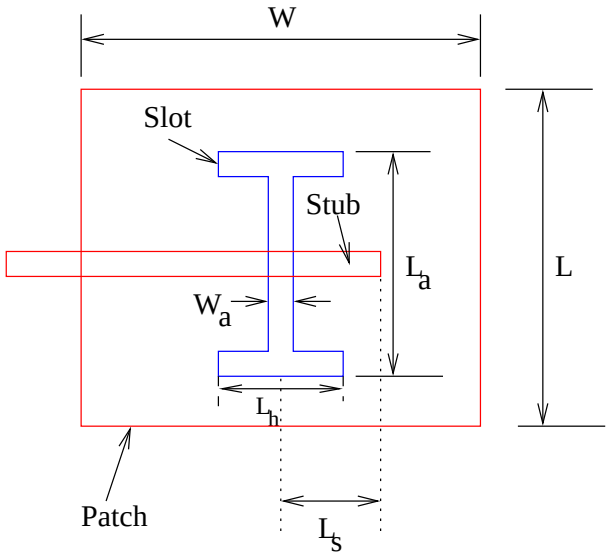

Figure 2.15: Top view of micro-machined H-slot coupled antenna.

2.3.1 Transmission line model for micro-machined aperture coupled antenna

The analysis followed for the micro-machined aperture coupled antenna is essentially the same as that of an ordinary aperture coupled patch antenna, discussed in section 2.2.1. But the determination of the effective dielectric constant, derivation of suitable expression for self impedance of the H-slot and the modification for aperture field distribution from I-slot distribution

has to be added to the analysis .

Effective dielectric constant of patch substrate

The most crucial part in the analysis of the micro-machined antenna is the derivation for the expression of effective dielectric constant of the top substrate forming the cavity. In [32] follows a capacitor model, where the effective dielectric constant of the cavity is analysed as a the dielectric constant of combination of two capacitors with silicon and air respectively. The results of [32] can be written as follows,

$$\epsilon_c = \frac{\epsilon_r}{1 + (\epsilon_r - 1)\frac{b}{a+b}} \tag{2.32}$$

where b is the height of air cavity and a is the thickness of the membrane supporting the patch. A more accurate way of finding the effective dielectric constant of the cavity follows the results for suspended-substrate microstrip lines derived in [33][34]. Consider the suspended microstrip line shown in Figure 2.16 where the substrate of dielectric constant ϵ_r and thickness a is suspended below the microstrip. The remaining region between the substrate and ground plane is assumed to be air having a thickness b. By

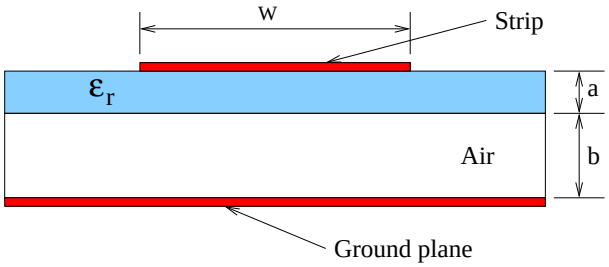

Figure 2.16: Suspended-substrate microstrip line.

the least square curve fitting method together with the computationally intensive spectral domain analysis, it has been shown in [33][34] that the expression for effective dielectric constant (ϵ_e) of the substrate can be written as,

$$\epsilon_e = \left[1 + \frac{a}{b}\left(a_1 - b_1 \ln \frac{W}{b}\right)\left(\frac{1}{\sqrt{\epsilon_r}} - 1\right)\right]^{-2} \tag{2.33}$$

where,

$$a_1 = \left(0.8621 - 0.1251 \ln \frac{a}{b}\right)^4 \tag{2.34}$$

$$b_1 = \left(0.4986 - 0.1397 \ln \frac{a}{b}\right)^4 \tag{2.35}$$

The above expressions has been used as the starting value in the following way to derive the final expressions of effective dielectric constant.

1) Substitute $a = H - h_{air}$ and $b = h_{air}$ in the above equations where h_{air} is the height of the air cavity shown in Figure 2.14.

2) The quasi-static expression for the effective dielectric constant of the microstrip line [35] is then used to find the dielectric constant ϵ_c of uniform cavity of height H bounded by a strip of width W. The following equation can then be iteratively solved to find ϵ_c,

$$\epsilon_e - \left(\frac{\epsilon_c + 1}{2} + \frac{\epsilon_c - 1}{2} \frac{1}{\sqrt{1 + 12H/W}}\right) = 0 \tag{2.36}$$

Thus by changing ϵ_r to ϵ_c in Figure 2.7, we follow the same analysis as for a transmission line model of aperture coupled patch.

Further accuracy in the determination of ϵ_e (see 2.33) may be achieved using the complex CAD models described in [36]. According to the analysis of [36],

$$\epsilon_e = (1 - f_1 f_2)^{-1} \tag{2.37}$$

where,

$$f_1 = 1 - \frac{1}{\sqrt{\epsilon_r}} \tag{2.38}$$

$$f_2 = \sum_{i=0}^{3} c_i \left(\frac{W}{b}\right)^i \tag{2.39}$$

where,

$$c_i = \sum_{j=0}^{3} d_{ij} \left(\frac{b}{a}\right)^j \tag{2.40}$$

More details and the polynomial coefficients $d_{ij}, i = 0..3, j = 0..3$ are given in appendix-C.

Self impedance of the H-slot

It is to be noted that in section 2.2.1 for the derivation of the aperture impedance Y_{ap}, the aperture is assumed as a parallel combination of two slotted lines, and the final expression for the aperture impedance is given in (2.15). The H-slot used in the micro-machined antenna can be considered as a combination of six different slotted lines, each representing one arm of the slot and referenced to the slot center. The wave number of the slot is derived as discussed in section 2.2.1. The expression for the H-slot impedance can then be written as follows [37],

$$Y_{ap}^{h} = -jY_{0S}\frac{2\tan(k_a(L_a - W_a)/2) - \cot(k_a L_h/2)}{2 + \cot(k_a L_h/2)\tan(k_a(L_a - W_a)/2)} \tag{2.41}$$

Modification of the slot electric field

Since the H-slot causes a different electric field distribution compared to I-slot distribution (2.16), the following modification may be used,

$$\mathbf{E}^a = \frac{V_0}{W_a}\frac{\left|e^{(jk_a(L_a - 2|y-y_o|))} + \Gamma_h\right|}{\left|e^{(jk_a L_a)} + \Gamma_h\right|}\hat{x} \qquad |x| \le W_a/2 \quad |y| \le (L_a - W_a)/2 \tag{2.42}$$

where Γ_h is the reflection coefficient of one side arm referenced to the main arm of the H-slot (see Figure 2.15) given by,

$$\Gamma_h = \frac{2j\tan(k_a L_h/2) - 1}{2j\tan(k_a L_h/2) + 1} \tag{2.43}$$

By substituting (2.42) in (2.18) the transformation ratio N_2 given in (2.18) can be numerically solved.

2.3.2 Results

Two set of antennas are fabricated using silicon based micro-machining technology. The silicon wafers ($\epsilon_r = 11.7$) has a thickness of $254\mu m$ (substrate for patch) and $100\mu m$ (substrate for microstrip line). The thickness of ground planes are approximately $1\mu m$. See Figure 2.14 and 2.15. The thickness of membrane is $50\mu m$. The patch dimensions for first set is $W = L = 1514\mu m$ and for the second one $W = L = 1714\mu m$. The H-slot dimensions are $W_a = 100\mu m$ and $L_h = 596\mu m$. For the microstrip stub the width is $w_m = 84\mu m$ and the stub-length is, $L_s = 450\mu m$. To accurately represent the model, microstrip open end effects has been included. Experiments

were conducted for two different slot length L_a, namely $L_a = 996\mu m$ and $L_a = 1100\mu m$. The transmission line model has been used in the analysis for both the suspended substrate microstrip line model(SSM) and capacitor model(CM). Figure 2.17 shows the comparison of the simulated and

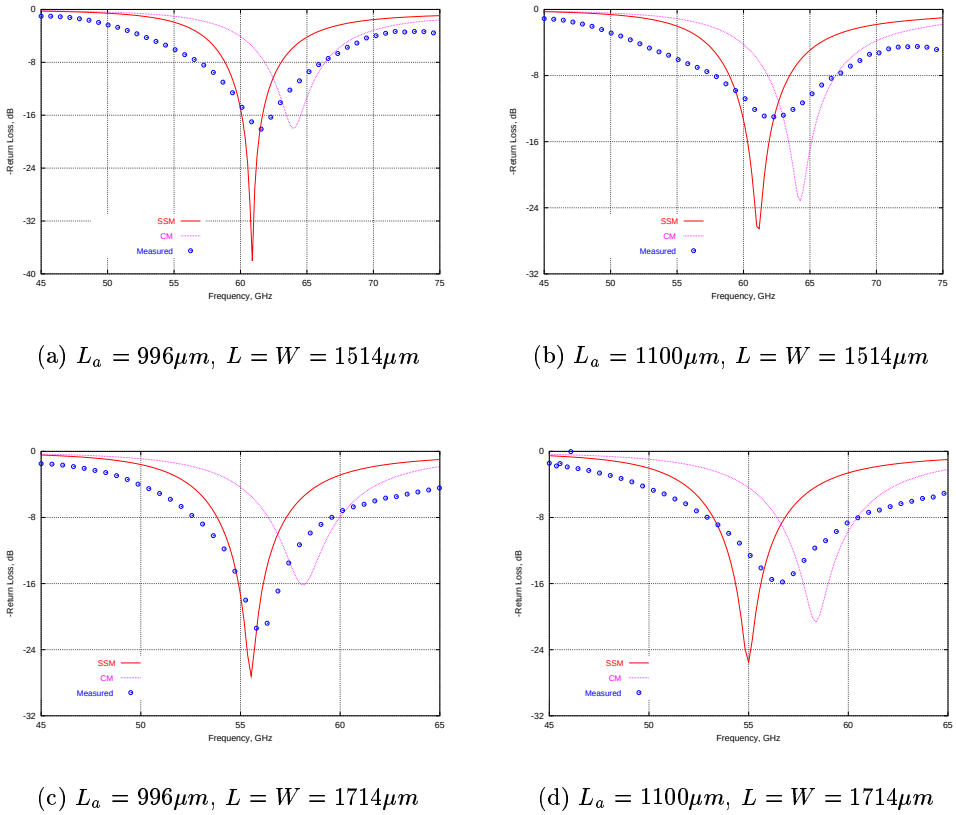

(a) $L_a = 996\mu m$, $L = W = 1514\mu m$

(b) $L_a = 1100\mu m$, $L = W = 1514\mu m$

(c) $L_a = 996\mu m$, $L = W = 1714\mu m$

(d) $L_a = 1100\mu m$, $L = W = 1714\mu m$

Figure 2.17: Return loss characteristics of the micro-machined H-slot coupled microstrip antenna.

experimental results for the micro-machined antenna . The return loss measurements [31] were made using a wafer-probing system described in [38]. It can been seen from Figure 2.17 that the resonant frequency for the experimental and the suspended substrate microstrip line model(SSM) are about the same. For the capacitor model the tuning frequency for the antenna is always higher. It can be seen from Figure 2.17 that the tuning frequency is not very sensitive to small changes in slot length L_a. However the tuning

frequency and the return loss characteristics has a large change with the increase of size of the patch from $W = L = 1514\mu m$ to $W = L = 1714\mu m$. The calculated effective dielectric constant using the suspended substrate microstrip model is approximately 1.48 and with capacitor model described in [39] the value is approximately 1.21 for both $W = L = 1514\mu m$ and $W = L = 1714\mu m$. In a future work accurate expressions for effective loss tangent may be included in the model. It is to be noted that parameters such as the thickness of ground plane has been taken to be zero in the present analysis. Also the losses in the microstrip line and cavity has been neglected to make the analysis simple. As a future work improvements of the model incorporating the above parameters may be carried out. Simulations for the entire frequency sweep with 168 frequency point took only about one minute on a personal computer. This can be considered extremely fast considering the time taken by commercial simulators employing the full wave electromagnetic methods for the same problem. It is also to be noted that there may be fabrication errors and measurement errors because of the small dimensions used in the design at millimeter-wave frequencies.

2.4 Conclusions

Transmission line and cavity model analysis is applied to generate a computer program for active microstrip antenna. The performance of the program has been tested on different antennas. The transmission line model has then been extended to incorporate a suspended substrate microstrip line model for analysis of millimeter-wave micro-machined antenna. Suitable modifications for the H-slot field distribution is introduced and simulated and experimental results are compared. Further improvements in the model is possible by incorporating the losses and the finite thickness of a slot in the ground plane. Excellent computational efficiency and less memory usage indicates that the method can be easily coupled to active circuit simulator and an optimization tool. In a future work the method will be extended to the design of active microstrip antennas.

Chapter 3

Spectral domain analysis of slots and slot matching for designing microwave amplifiers

In this chapter a computationally efficient method is introduced to analyse slots in the ground plane of microstrip line. The proposed method combines the spectral domain method derived in [40] and the transverse resonance technique derived in [27]. In [40], the unknown slot fields are represented as a linear combination of basis functions with unknown coefficients. The method of moments was then used to deduce the coefficients of each basis function. In representing the slot fields, piece wise sinusoidal(PWS) modes has been used as basis functions and it was concluded that at least three modes are needed to accurately analyse the slot. It is concluded in the present work that the source of error in the representation of slot electric field in [40], arises from the error in the wave number of PWS. It will be demonstrated in this chapter that by using the correct wave number of a single PWS mode it is possible to achieve the same results as in [40]. Thus the method being proposed is computationally more efficient since the time required in finding exact wave number of single PWS is small [27]. The potential for such fast analysis of slots is demonstrated by designing a low noise amplifier based on non resonant slot matching. Although the slots considered in the design of amplifier are different from the normal rectangular slot in the spectral domain analysis, the same analysis is planned in the future to be extended to non rectangular slots.

The motivation of non resonant slot matching in designing microwave amplifiers [41] arises from the disadvantages of transmission line matching using microstrip lines. For many applications the disadvantages of planar transmission lines, such as large area consumption and conductor losses are undesirable. The results of [40] points to the fact that the reactance to resistance value of the slot impedance can be very low provided that the slot is operated in the non-resonant region. Similar results for wide rectangular slots are reported in [42]. The low resistive part of the slot impedance at the operating frequency ensures minimum radiation losses. Simulated and experimental results of this chapter indicate that the gain and noise figure characteristics of the slot matched amplifier is superior to that of microstrip matched amplifier. Various sections in this chapter are connected as follows:

The properties of sandwich-slotlines will be examined in section-3.1 with emphasis on derivation of slotline wavelength. The detailed analysis however has been carried out using transverse resonance technique in appendix-D for different classes of sandwich-slotlines. Exact slotline wavelength is then used to carry out a spectral domain analysis of rectangular slots in section-3.2. Application of non-resonant slots in designing microwave amplifier is then described in section-3.3.

3.1 Sandwich-slotlines

Since the spectral domain analysis of slots followed in this chapter needs determination of exact wave number in the corresponding slot line, we first examine the properties of the general sandwich-slotline shown in Figure 3.1. In spite of interesting properties such as ease in fabrication and connectivity with active circuits the slotlines are not popular compared to planar transmission such as microstrip lines. One of the main reasons for the above situation arises from the computational complexity involved in extracting parameters such as propagation constant and characteristic impedance. Moreover for optimum performance such as minimum radiation loss, the slotline wavelength should be very small compared to free space wavelength. This is accomplished by using a high permittivity substrate which can be expensive. The classic paper by Cohn [27] explores the properties of slotlines using single substrate by means of transverse resonance technique. In [27] the guided wavelength of the slot is expressed as the transverse resonance wavelength between the junction of waveguides with electric walls across the slotline separated by half the slotline wavelength. The characteristics of single sub-

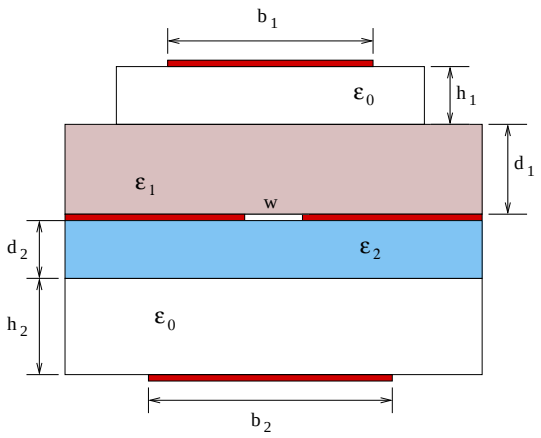

Figure 3.1: Sandwich-slotline of width w between two dielectric substrates in the presence of parallel conducting strips of width b_1 and b_2.

strate slotline is further investigated in [43] using a spectral domain method which is more complex to use compared to [27]. In single layered slotline the parameters such as propagation constant and characteristic impedance is limited by the choice of substrate dielectric constant and width of the slot. Sandwich-slotline [28] provides an additional substrate on top of the slotline. Thus the characteristics of a single substrate slotline can be further varied by using the parameters of the new substrate such as its thickness and dielectric constant. Since the use of multilayer techniques in microwave circuit design is gaining momentum, the use of extra substrate is not an added problem for the use of sandwich-slotline. An interesting variation of this new approach is using conducting strip on top of the substrates. It is seen in [28] that the strip has a much larger effect on the propagation characteristics compared to mere variation of the substrate properties. Appendix-D investigates the properties of a sandwich-slotline in the presence of parallel conducting strip using transverse resonance technique and specific cases such as sandwich-slotline on silicon wafer is investigated. The technique followed is the same as that in [27], except extensions which take care of additional substrates and strips [28]. In the following section simulated results based on the analysis of appendix-D for various classes of slotlines will be presented.

Results

Slotline on single substrate

The first structure simulated is a single substrate slotline with no conducting strip (see Figure 3.2). The transverse resonance technique with magnetic walls separated by 75mm has been used in the simulation. The dielectric constant and thickness of the substrate are $\epsilon_{r2} = 20$ and $d_2 = 3.425mm$ respectively where $\epsilon_i = \epsilon_{ri}\epsilon_0$. The width of the slotline, $w = 0.625mm$. It can be seen that there is wide variation in propagation characteristics for both the effective dielectric constant and propagation constant. The same structure has been simulated and measured in [27]. It can be seen that the results agree well.

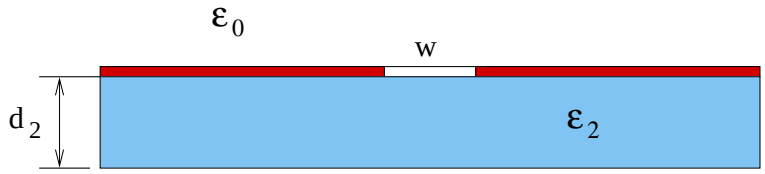

Figure 3.2: Slotline on single substrate.

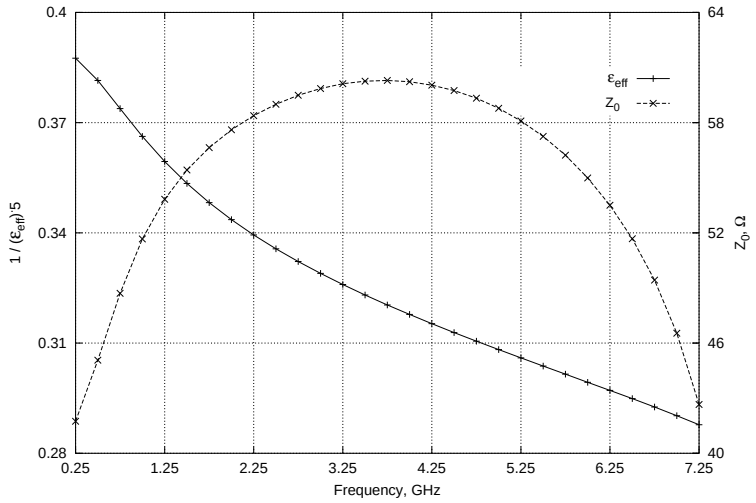

Figure 3.3: Dispersion characteristics of slotline on single substrate.

Sandwich-slotline with a parallel conducting strip

The structure studied is shown in Figure 3.4. The width of the slotline is $w = 1mm$. The variable is the width of the conducting strip b_2. The thickness of the substrates are $d_1 = 0.8mm$, $d_2 = 0.8mm$. Dielectric constants of both the substrates are $\epsilon_{r1} = \epsilon_{r2} = 2.17$. For the modeling, the magnetic walls in the top layer is separated by $3\lambda_0$ while the conductor backed layer has the magnetic wall separation of b_2.

Figure 3.5 shows the simulated results. The same structure has been simulated in [28] but only for 2.5GHz. It can be seen that both the results agree well. From the results of Figure 3.5 we see that the size of the conducting strip has a large influence on both the characteristic impedance and effective dielectric constant. It can be seen that when b_2 increases the characteristic impedance drops sharply until about $b_2 = 0.4\lambda_0$, but for sufficiently large b_2 characteristic impedance remains constant.

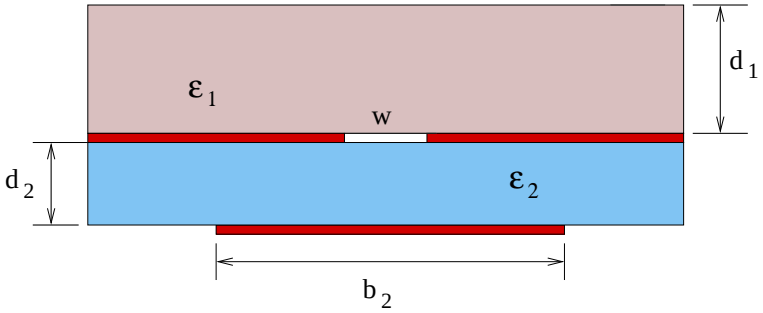

Figure 3.4: Sandwich-slotline backed by a parallel conducting strip.

To study the dispersion characteristics, results are simulated for two more frequencies namely 1GHz and 5.5GHz. The differences in characteristics between the three frequencies indicates the strong non-TEM nature of the wave propagation.

Sandwich-slotline with two parallel conducting strips

Micro-machining technology for RF components using silicon is a new research area [44]. In this simulation we investigate the properties of a micro-machined slotline sandwiched between a silicon wafer and air gap. Such a structure may be more convenient to manufacture compared to the coplanar line, at the same time resulting in large difference between slotline wavelength and free space wavelength. The later property enhances the perfor-

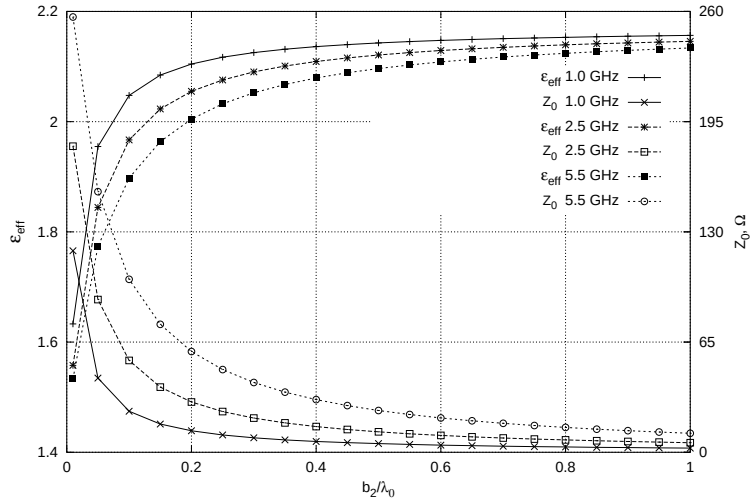

Figure 3.5: Sandwich-slotline backed by a parallel conducting strip: effect of the width of the strip on the characteristics.

mance of the slotline. In the present simulation it is assumed that conducting strips are present in each layer. See Figure 3.6, the data assumed are, width

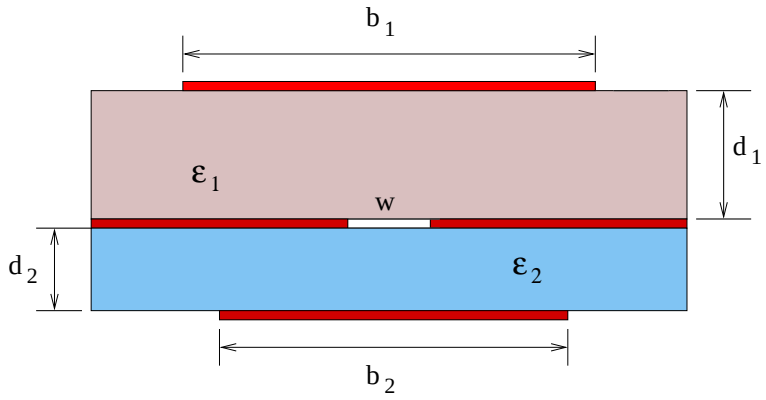

Figure 3.6: Sandwich-slotline backed two parallel conducting strips.

of the slot, $w = 50\mu m$ and for the silicon wafer the dielectric constant and thickness are, $\epsilon_{r1} = 1, \epsilon_{r2} = 11.7$, and $d_2 = 200\mu m$ respectively. The width of the conducting strips b_1 and b_2 are $1500\mu m$ and $500\mu m$ respectively. The large widths are deliberately chosen to simulate it as the ground plane. Figure 3.7 shows the simulated results of the structure. The effective dielectric

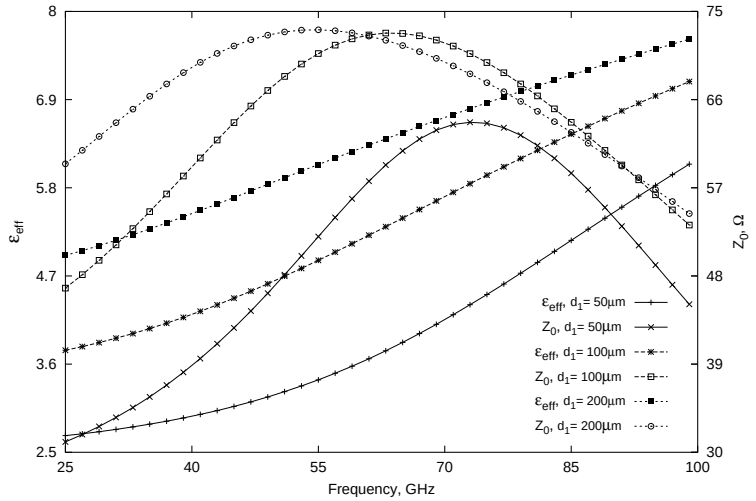

Figure 3.7: Sandwich-slotline backed two parallel conducting strips.

constant varies almost linearly with a positive slope with respect to d_1. The characteristic impedance first increases and then decreases. It can be seen that the characteristic impedance is around 50Ω for all the cases. The increase in d_1 from 100 to 200μm results in small change in characteristics compared to the change from 50 to 100μm. This indicates the reduction of influence of conducting strip with the distance.

3.2 Spectral domain analysis of slots

3.2.1 Application of reciprocity theorem.

Figure 3.8 shows the geometry of microstrip line fed rectangular slot of length L and width W. Let the admittance of the slot be Y^e. Since microstrip line of small width can be accurately described by its quasi TEM representation, only that mode is used to represent it as a transmission line. The discontinuity in voltages between slot and microstrip line is represented, similar to that of aperture coupled antenna in Chapter 1 by a transformer. In order to derive Y^e and transformer ratio the reciprocity theorem can be used by assuming a known slot field representation but with unknown amplitudes.

Refer Figure 3.8. Consider the electromagnetic fields of microstrip line refer-

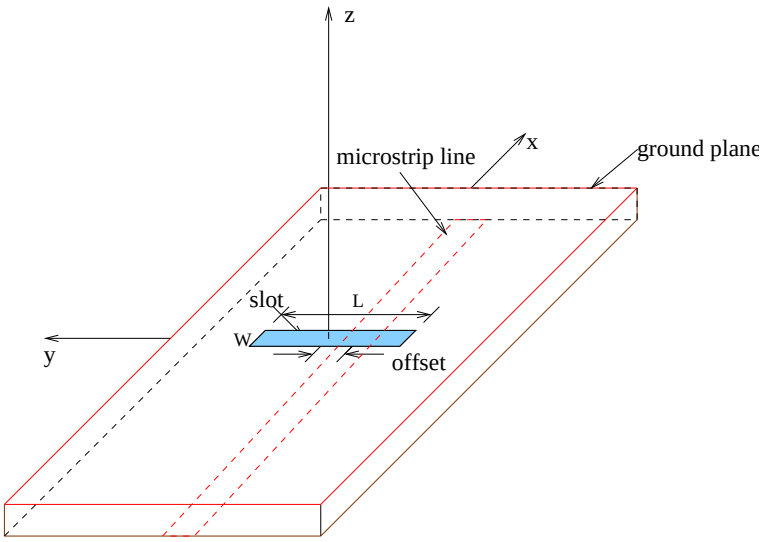

Figure 3.8: Rectangular slot with a microstrip feed.

enced to the center of slot ($x = 0$). Let $\bar{E}^+, \bar{H}^+$ and $\bar{E}^-, \bar{H}^-$ be the incident and transmitted electric and magnetic field vectors respectively. Then total fields can be written as,

$$\bar{E} = \begin{cases} \bar{E}^+ + R\bar{E}^-, & \text{for } x < 0 \\ T\bar{E}^+, & \text{for } x > 0 \end{cases} \tag{3.1}$$

$$\bar{H} = \begin{cases} \bar{H}^+ + R\bar{H}^-, & \text{for } x < 0 \\ T\bar{H}^+, & \text{for } x > 0 \end{cases} \tag{3.2}$$

$$\begin{aligned} \bar{E}^\pm &= (e_y\hat{y} + e_z\hat{z})\, e^{\pm\beta x} \\ \bar{H}^\pm &= \pm\,(h_y\hat{y} + h_z\hat{z})\, e^{\pm\beta x} \end{aligned} \tag{3.3}$$

where β is the effective propagation constant of the microstrip line. The following normalisation criterion is used for the representation of microstrip fields,

$$\int_{y=-\infty}^{\infty}\int_{z=0}^{\infty} \bar{e} \times \bar{h} \cdot \hat{x}\, dy\, dz = 1 \tag{3.4}$$

where $\bar{e} = e_y\hat{y} + e_z\hat{z}$ and $\bar{h} = h_y\hat{y} + h_z\hat{z}$.

A single piecewise sinusoidal mode is used to represent aperture electric field.
For $|x| < W/2, |y| < L/2$, the aperture field is then given by,

$$\bar{E}^a = e^a(x,y)\hat{x} \tag{3.5}$$

where the only PWS mode used in this chapter is represented by,

$$e^a(x,y) = V_0 \frac{\sin k_e(L/2 - |y|)}{W \sin k_e L/2} \tag{3.6}$$

By applying the reciprocity theorem,

$$\int_S \bar{E} \times \bar{H}^+ \cdot d\bar{s} = \int_S \bar{E}^+ \times \bar{H} \cdot d\bar{s} \tag{3.7}$$

$$\int_S \bar{E} \times \bar{H}^- \cdot d\bar{s} = \int_S \bar{E}^- \times \bar{H} \cdot d\bar{s} \tag{3.8}$$

where S is the closed surface bounded by the effective cross section of the microstrip line, the aperture surface and the walls of microstrip line [40]. For the quasi TEM mode being considered in this chapter $e_y = h_z = 0$ for microstrip line. Then (3.1),(3.2) and (3.7) yields,

$$R = \triangle V = \int_{S^a} e^a(x,y) h_y(x,y)\, ds \tag{3.9}$$

Similarly (3.1),(3.2) and (3.8) yields,

$$T = 1 - \frac{V_0}{2} \int_{S^a} e^a(x,y) h_y(x,y)\, ds = 1 - R \tag{3.10}$$

There are three unknowns namely R, T and V_0 in the last two equations. Therefore we need one more equation for the solution of the three quantities. Enforcing the continuity of H_y over the aperture,

$$H_y^e = H_y^f + H_y^i \tag{3.11}$$

where H_y^e and H_y^i are the exterior ($z > 0$) and interior field ($z < 0$) due to aperture field. H_y^f is the interior field ($z > 0$) due to feed line modes.
At $x = 0^-$ the feed line magnetic field can be written as,

$$H_y^f = (1 - R) h_y \tag{3.12}$$

Defining Green function G_{yy}^{HM} (Appendix-A) to account for H_y fields on both sides of aperture($z = 0$) due to a y directed magnetic aperture current,

$$H_y^e - H_y^i = V_0 \int_{S_a} G_{yy}^{HM}(x, y : x_0, y_0) \cdot e^a(x_0, y_0)\, ds_0 \tag{3.13}$$

Here, G_{yy}^{HM} can be interpreted as the magnetic field H_y at $(x, y, 0)$ due to $\hat{y}$ directed unit magnetic current element at $(x_0, y_0, 0)$. From (3.11), (3.12) and (3.13) we can write,

$$\begin{aligned} V_0 \int_{S_0} G_{yy}^{HM}(x, y; x_0, y_0) e^a(x_0, y_0)\, ds_0 \\ = (1 - R) h_y(x, y), \text{ for } |x| < W/2, |y| < L/2 \end{aligned} \tag{3.14}$$

Multiplying the above equation by $e^a(x_0, y_0)$ and integrating over S_a we get,

$$\begin{aligned} V_0 \int_{S_a} \int_{S_a} G_{yy}^{HM}(x, y; x_0, y_0) e^a(x_0, y_0)\, ds\, ds_0 \\ = (1 - R) \int_{S_a} e^a(x, y) h_y(x, y)\, ds \end{aligned} \tag{3.15}$$

$$V_0 Y^e = \triangle V (1 - R) \tag{3.16}$$

where

$$Y^e = \int_{S_a} \int_{S_a} e_x^a(x, y) G_{yy}^{HM}(x, y; x_0, y_0) \cdot e_x^a(x_0, y_0)\, ds\, ds_0 \tag{3.17}$$

The three unknowns V_0, R, T can now be written in terms of Y^e and $\triangle V$ as,

$$V_0 = \frac{2\triangle V}{\triangle V^2 + 2Y_e},\ R = \frac{\triangle V^2}{\triangle V^2 + 2Y_e},\ T = \frac{2Y^e}{\triangle V^2 + 2Y_e} = (1 - R) \tag{3.18}$$

The impedance of the slot, Z transferred to microstrip line with characteristic impedance, Z_C can now be written as,

$$Z = Z_C \frac{2R}{1 - R} = Z_C \frac{\triangle V^2}{Y^e} \tag{3.19}$$

Thus the microstrip fed rectangular slot can be represented by a transmission line model as shown in Figure 3.9. In the Figure 3.9, $N = \triangle V \sqrt{Z_C}]$.

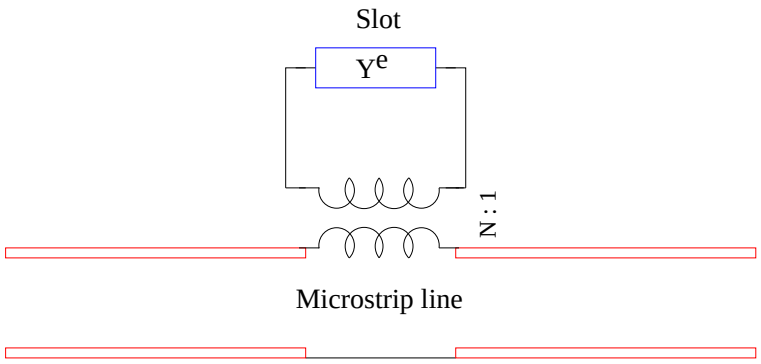

Figure 3.9: Transmission line model of a rectangular slot with microstrip feed.

3.2.2 Spectral domain representation of slot impedance

The integral given in (3.17) can now be written in spectral domain as,

$$Y^e = \frac{1}{4\pi^2}\int_{k_x=-\infty}^{\infty}\int_{k_y=-\infty}^{\infty}\left[\tilde{E}^a(k_x,k_y)\right]^2 \tilde{G}_{yy}^{HM}\, dk_x\, dk_y \tag{3.20}$$

where $\tilde{G}_{yy}^{HM}$ and G_{yy}^{HM} [see (3.17 and Appendix-A] constitutes a Fourier transform pair [40]. $\tilde{E}^a(k_x,k_y)$ represents the Fourier transform of the slot electric field [see (3.6)] given by,

$$\tilde{E}^a(k_x,k_y) = \frac{k_e L^2}{4\sin\frac{k_e L}{2}} sinc\left[\frac{(k_e+k_y)L}{4}\right] sinc\left[\frac{(k_e-k_y)L}{4}\right] sinc\left[\frac{k_x W}{2}\right] \tag{3.21}$$

where $sinc(x) = \sin x/x$. The transformation ratio of the slot $\triangle V$ [see(3.9)] can be written in terms of the spectral domain Greens function $\tilde{G}_{yx}^{HJ}$ [see Appendix-A] as,

$$\triangle V = \frac{1}{2\pi\sqrt{Z_C}}\int_{k_y=-\infty}^{\infty} \tilde{E}^a(k_x=-\beta,k_y)\tilde{G}_{yx}^{HJ}(k_x=-\beta,k_y)\tilde{H}_(k_y)cos(k_y y_{off}) \tag{3.22}$$

where y_{off} is the offset of the microstrip line from the center of the slot (Figure 3.8) and $\tilde{H}(k_y)$ is the Fourier transform of the $\hat{y}$ component of microstrip magnetic field. For this field, parallel plate model has been used to define a pulse magnetic field function of height $1/W_{eff}$ [40] where, W_{eff}

is the effective width of microstrip line.

$$\tilde{H}(k_y) = sinc\left(\frac{k_y W_{eff}}{2}\right) \tag{3.23}$$

To facilitate the evaluation of (3.20) we can substitute $k_x = \gamma\cos\theta$ and $k_y = \gamma\sin\theta$. Then using Appendix-A, (3.20) can be written in the following form.

$$Y^e = \int_{\theta=0}^{2\pi}\int_{\gamma=0}^{\infty}\left[\tilde{E}^a(\gamma,\theta)\right]^2 \tilde{G}_{yx}^{HJ}(\gamma,\theta)\,\gamma d\gamma\, d\theta \tag{3.24}$$

where from Appendix-A $\tilde{G}_{yy}^{HM}(\gamma,\theta)$ attains the following form.

$$\tilde{G}_{yy}^{HM}(\gamma,\theta) = \frac{N(\gamma,\theta)}{D(\gamma)} \tag{3.25}$$

Thus the denominator D of $\tilde{G}_{yy}^{HM}$ is a function of only γ. $\therefore$ we have to consider the poles of $D(\gamma)$ for integration. The method followed is to split the integrand of γ into singular and nonsingular part. The non singular part can be integrated numerically. Cubpack++ an efficient and free C++ package has been used for the numerical integrations[45]. The integrations over non singular part is discussed in Appendix-A

3.2.3 Results

Figure 3.10 shows the comparison of spectral domain method described here and the method of moments technique in [40]. It can be seen that there is a good agreement between both the methods. Dielectric constant and thickness of the substrate are $\epsilon_r = 2.2$ and $d = 1.6mm$. The slot width and length are $W = 7mm$ and $L = 40.2mm$ respectively. The width of the microstrip line is $5mm$. It is seen that effective dielectric constant of the slot calculated using [27], which has been followed here, varies between 1.29 and 1.32 in the frequency range. But using the method followed in [40] the value is 1.6. It can be thus seen that the reason for achieving correct results here lies in using exact value of effective dielectric constant of slot. We can therefore conclude that computational time can be drastically reduced by having one correct PWS mode instead of using approximations for the effective dielectric constant (or effective wave number) together with many basis functions in [40].

Figure 3.11 shows the simulated resistance characteristics of an offset fed

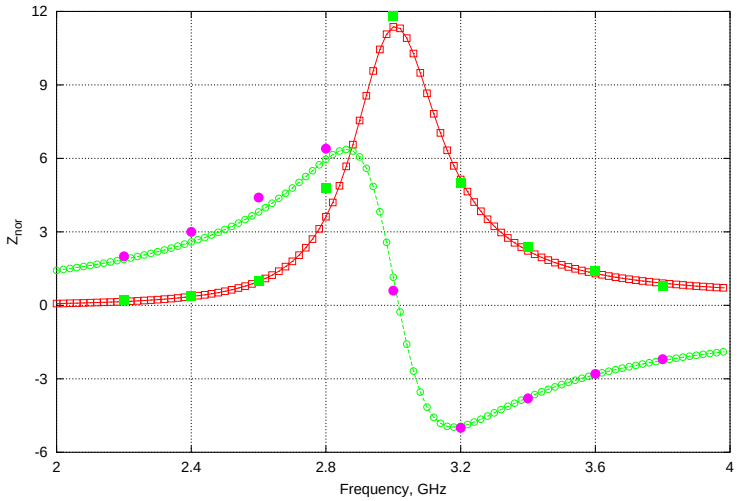

Figure 3.10: Slot with microstrip line feed: comparison with moment method [40]: ∘-Im[Z_{nor}]simulated, shaded ∘- Im[Z_{nor}] in [40]. □- Re[Z_{nor}] simulated, shaded □-Re[Z_{nor}] in [40].

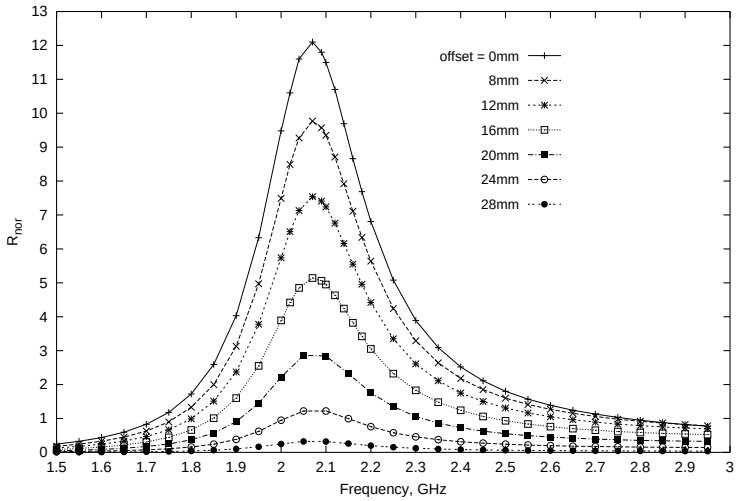

Figure 3.11: : Resistance characteristics of slot with offset microstrip line feed (see Figure 3.8 as a function of offset).

slot. The width and length of the slot are $W = 2mm$ and $L = 60mm$ re-

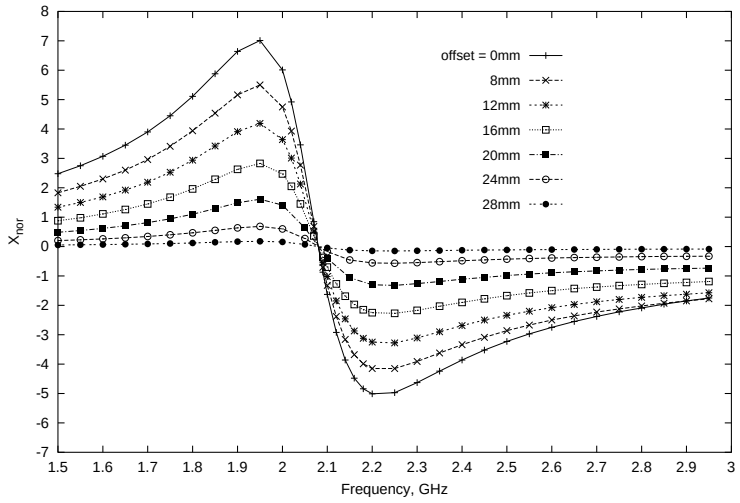

Figure 3.12: Slot with offset microstrip line feed (See Figure 3.8): Reactance characteristics of slot as a function of offset.

spectively. The substrate dielectric constant and height are 2.2 and $1.597mm$ respectively. It can be seen that as the offset y_{off} (see Figure 3.8) increases the resistance decreases due to less coupling to slot. The variations are exactly similar to the experimental results of [46]. It is to be noted that the resonant frequency for all the offset values remains the same and is equal to about $2.075GHz$. Simulated results for reactance characteristics is shown in Figure 3.12. It can be seen that for the offset range used, the change in resistance is almost twice as that of the change in reactance in the non resonant region. Thus offset fed slots provides an effective way of reducing the resistance of a resonant slot. Therefore the method has potential applications for matching active circuits as will be discussed in the next section.

3.3 Design of low noise amplifier based on slot matching

3.3.1 Series slot matching using non-resonant slots

The results of previous section indicate that a slot in the ground plane of microstrip line can be represented as a series impedance. By adjusting the resistive part of the slot impedance to a small value we can implement matching circuits, for instance in amplifier designs. The low resistance of

the slot ensures minimum radiation losses. This is the principle of slot matching. Offset feeding is one way of reducing the resistance as has been demonstrated in the previous section. It should also be noted that since the equivalent impedance of the slot is in series with microstrip line, the principle of matching is the series reactance matching technique, which is not possible with usual transmission line stubs such as microstrip lines.

3.3.2 Amplifier design using nonresonant slots

The series slot matching is implemented for the output and input of a low noise amplifier operating at a frequency of 1GHz. The transistor used is ATF-10136 [47] in a common source configuration .

In the design, we have considered L-slot and dog bone slots for matching the input and output respectively. The layout representation of the transis-

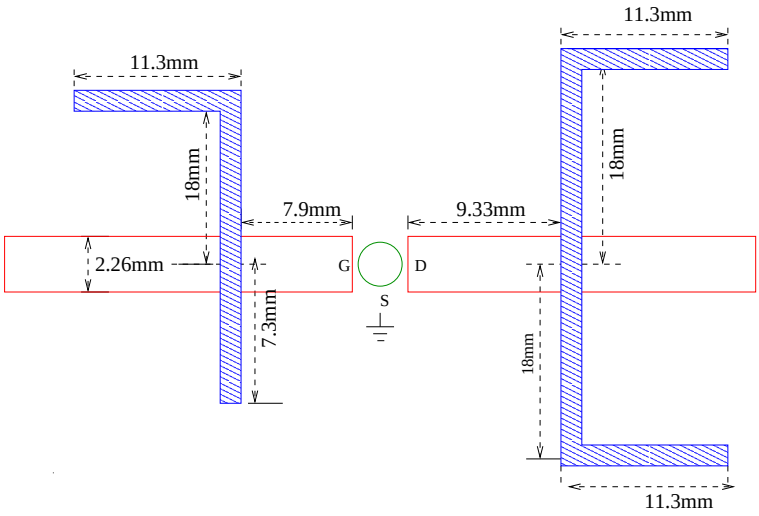

Figure 3.13: Layout representation of the common source LNA (hatched portion is slots used for matching) width of slots=0.6mm, substrate:-Teflon, $\epsilon_r = 2.53, thickness = 0.8mm$.

tor amplifier is shown in Figure 3.13. The optimum dimensions of the slot has been derived from the performance criteria of the amplifier, which is a gain of 18dB at noise figure of 1.5dB. The characterization of the slots were done using a method of moments based CAD program [48]. The following steps has been used for the designing the slot matched amplifier.

- The amplifier input and output reflection coefficients were first determined for the assumed gain and noise figure.
- Planar simulator [48] is then used to design the slots as per the requirements of the amplifier.
- The scattering matrix of the slots are then implemented in a circuit simulator.
- The complete amplifier comprising of the transistor and slot combination is then simulated in an active circuit simulator and the gain and noise figure characteristics are verified.

As a future work the theoretical approach followed in the previous section can be coupled to the active circuit simulator, thus speeding the design of the slot matched amplifier.

3.3.3 Results

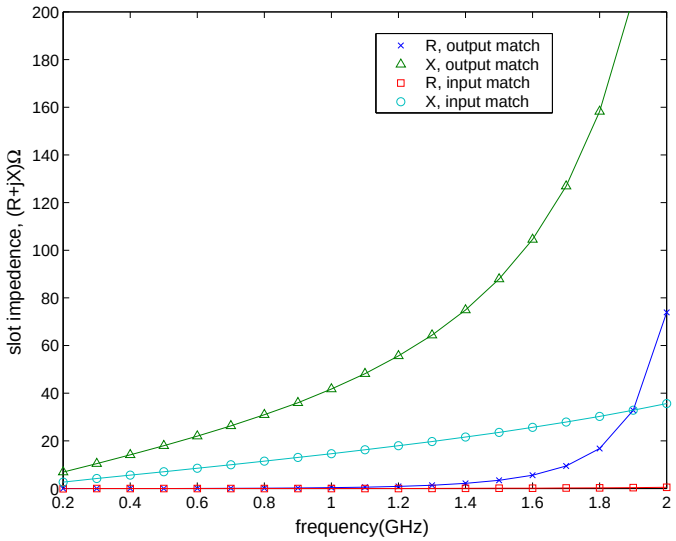

Figure 3.14: Slot impedance for the input and output match in series as a function of frequency.

Figure 3.14 shows the simulated results of the slot impedances used for input and output matching. It can be seen that the resistance is very small

at an operating frequency of 1GHz. For the input match, since the transverse length of slot is much less than the resonant length, the resonant resistance is almost zero. This ensures minimum radiation losses from the circuit. To compare the performance of the slot based amplifier, a shunt stub matched amplifier was designed for the same specifications as above. Figure 3.15 shows the comparison for the performance of LNA designed using slot matching and shunt stub matching. It can be seen from Figure 3.15 that there is close agreement between simulated and experimental results. It can also be seen that the bandwidth and noise-figure characteristics is

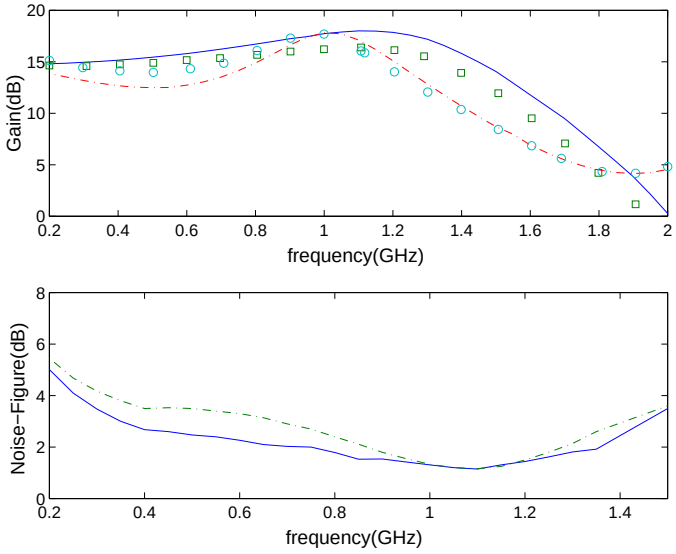

Figure 3.15: Performance characteristics of LNA.: solid line:= slot amplifier (simulated), dashed line:= stub amplifier (simulated) , ∘ ∘:=stub amplifier (measured) and □ □:=slot amplifier (measured).

better for slot amplifier compared to stub amplifier. It is also worth while here to point out that overall size of the circuit is approximately half that of the traditional microstrip stub amplifier. Further size reduction of the slot amplifier is possible by controlling the resonant length of slots by dielectric loading on the other side of ground plane and strips for further control of slot characteristics. This is discussed in section-3.1.

3.4 Conclusions

A combination of the spectral domain method and the transverse resonance technique is applied to analyse a slot in the ground plane of a microstrip line. The simulated results agree well with method of moments technique. The proposed method requires less computational resources compared to method of moments.

It has been shown that the resistance and reactance values of a slot can be controlled by the amount of offset between the feed and the center of the slot. This technique may therefore be useful for designing matching circuits. The application of slots in matching active circuits has been studied by designing the low noise amplifier. Improved characteristics for an LNA has been achieved using the slot matching. The size of the LNA designed using slot matching is nearly half than that of a traditional stub based amplifier. The proposed method could be used designing microwave and millimeter-wave active integrated circuits.

Chapter 4

Nonradiative Dielectric Waveguides and applications

In this chapter applications of nonradiative dielectric(NRD) waveguides [49] for multilayer integration technology are investigated. A new way of using the NRD waveguide as a plug between two substrates is studied by using the transmission line model. The application of NRD plugs as feeds for antennas is further investigated by implementing a dual polarised NRD fed microstrip antenna.

The interest in NRD waveguides stems from their suitability for implementation of multilayered integrated circuits and from advantages such as low cost fabrication and loss loss characteristics. The low loss of the NRD waveguide particularly at millimeter-wave makes it a more suitable waveguide compared to coplanar lines and microstrip lines. The NRD waveguide has previously been used in the design of a feed network for slot antennas in [50], as a leaky wave feed for planar antennas in [51] and in the design of a millimeter-wave oscillator in [52]. NRD guide based interconnects may be extremely useful for the obvious reason that they are non radiative compared with traditional interconnects which are radiative unless carefully designed and posing challenges to EMC.

One of the key problems in the design of circuits involving NRD is the coupling of electromagnetic energy in and out of the NRD waveguide. In [49] a rectangular waveguide has been used as the feed for the NRD guide.

Since most applications nowadays is based on planar technology, the rectangular waveguide feed as used in [49] may tend to increase the overall size of the system whereby loosing advantages of planar technology such as small size· In [53] stripline feed has been used for the NRD guide feed, where the feed structure also suffers from drawbacks such as large size and complexity in design. The hybrid integration technology proposed in [54] where the NRD guide serves as an interconnect between two different layers with energy coupled via an aperture is an attractive option in this context. Also, since the interconnect is three dimensional, considerable space is released for mounting active components between different layers. To analyse the NRD connectors a transmission line model has been introduced [55]. The method proposed speeds up the design phase of NRD guide based systems as commercial simulators are not efficient for multilayer designs. In the present analysis we consider only the dominant NRD mode, however further improvement in the accuracy of the model can be achieved by extending the general framework proposed in this chapter to higher order modes. In practice the initial design achieved using the transmission line model can be further refined using a full-wave simulator rather than using the fullwave simulator from the beginning, thereby saving time in the design.

4.1 Dielectric connectors based on NRD waveguides

The dielectric connectors studied in this chapter is depicted in Figure 4.1 and 4.2. The difference between Figure 4.1 and Figure 4.2 is that in Figure 4.2 the slots lie one over the other so that the effective length of the guide is reduced.

Since the microwave and millimeter-wave integrated circuits on single substrates are becoming more and more complex, the NRD guides can serve as effective building blocks for integrating two planar integrated circuits one on each side of the NRD. In the above process the NRD guide also fulfills the requirements of connectors such as minimum radiation from the transitions and less losses. It has also been proved that compared with other transmission lines such as coplanar lines and microstrip lines, radiation losses are small from junctions and curved portions of the NRD guide [49].

The possible modes of the NRD are the longitudinal section magnetic and

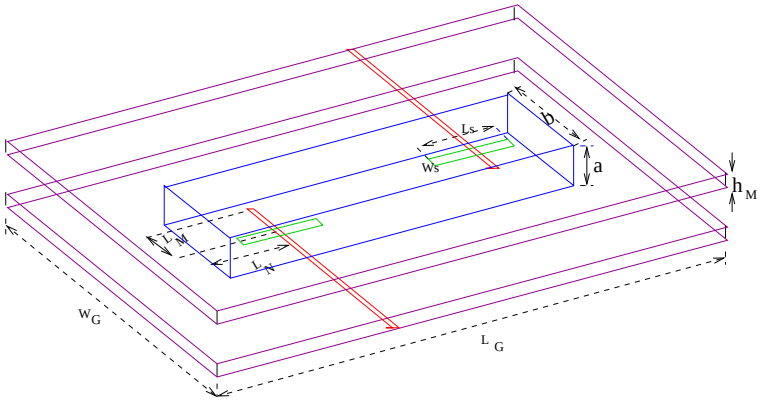

Figure 4.1: NRD waveguide based multilayer structure.

longitudinal section electric modes. Appendix-B gives the electromagnetic analysis of an NRD guide of height a and width b. The fundamental criterion to be satisfied for nonradiative operation of the NRD guide is that distance between the ground planes is less than half the free space wavelength $(\lambda_0/2)$.Therefore the NRD guide has to be operated between the launch of the fundamental mode and higher modes with the constraint that the distance between the ground planes, a, has to be less than $\lambda_0/2$.

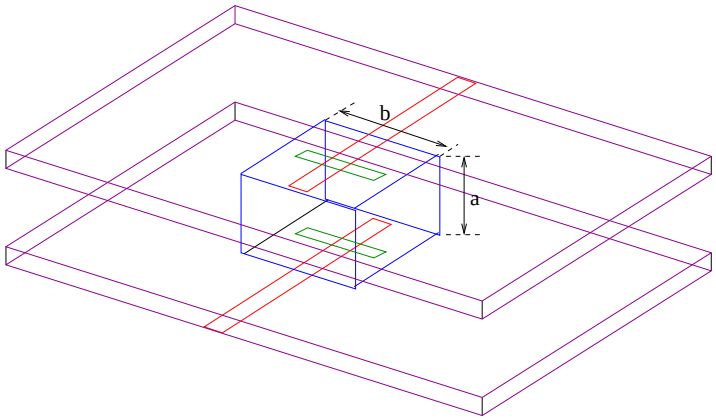

Figure 4.2: Multilayer structure based on NRD plug.

A diagram showing the possible a,b combinations for operation as mentioned above is called the operational diagram. Figure 4.3 shows the operational

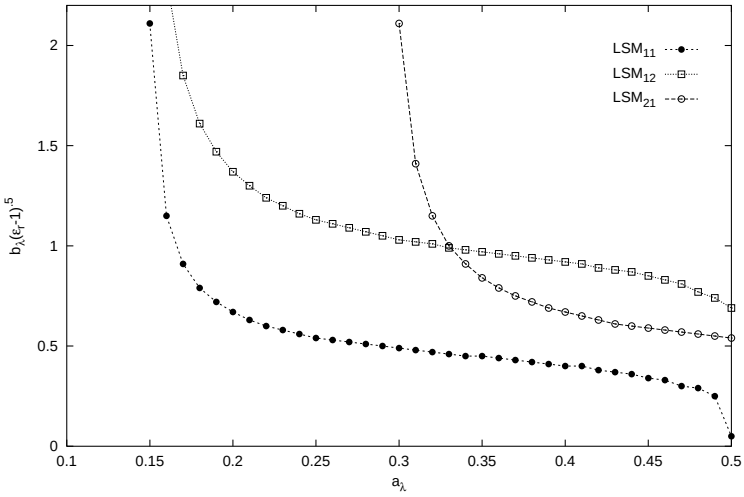

Figure 4.3: Operational diagram for an NRD guide based on silicon, $\epsilon_r = 11.7$.

diagram of an NRD guide based on silicon. The normalised height a_λ (normalised with respect to wavelength) is shown on the x-axis and the product of normalised width b_λ and $\sqrt{\epsilon_r - 1}$ is shown on the y-axis. Each point on a particular modal curve on the operational diagram denotes a particular width-height combination to launch the mode. As usual with any waveguide, we have to limit the operation of the waveguide to its fundamental mode. To meet this objective in the case of the NRD guide, its operational diagram is very convenient as it simplifies the understanding of the otherwise complex propagation characteristics. Thus we can see from Figure 4.3 that, for single mode operation the width-height combination needed is confined between the upper portion of the fundamental mode curve LSM_{11} and the lower portions of higher order LSM_{12} and LSM_{21} mode.

From the derivations in appendix-B we can see that the propagation constant of the fundamental symmetric mode, LSM_{11} and the second higher

order symmetric mode, LSM_{21} satisfies the following eigen system,

$$\beta_{yn} \tan\left(\frac{\beta_{yn} b}{2}\right) = \epsilon_r \zeta_n \tag{4.1}$$

where

$$\begin{aligned} \zeta_n^2 &= k_0^2(\epsilon_r - 1) - \beta_{yn}^2 \\ \beta_{mn}^2 &= k_0^2 \epsilon_r - (m\pi/a)^2 - \beta_{yn}^2 \end{aligned} \tag{4.2}$$

β_{yn} is the y-directed propagation constant in the dielectric region and ζ_n is the corresponding attenuation constant in the air region. For propagation the phase constant β_{mn} should be real and positive. It should be noted that $\beta_{yn} b/2$ is between $(n-1)\pi/2$ and $n\pi/2$ for the mn^{th} mode. Similarly, for the evaluation of the propagation constant of the antisymmetric mode LSM_{12} we have to solve the following eigen system.

$$\frac{\beta_{yn}}{\tan\left(\frac{\beta_{yn} b}{2}\right)} = -\epsilon_r \zeta_n \tag{4.3}$$

To prevent the launch of higher order LSM_{21} mode, which results in a

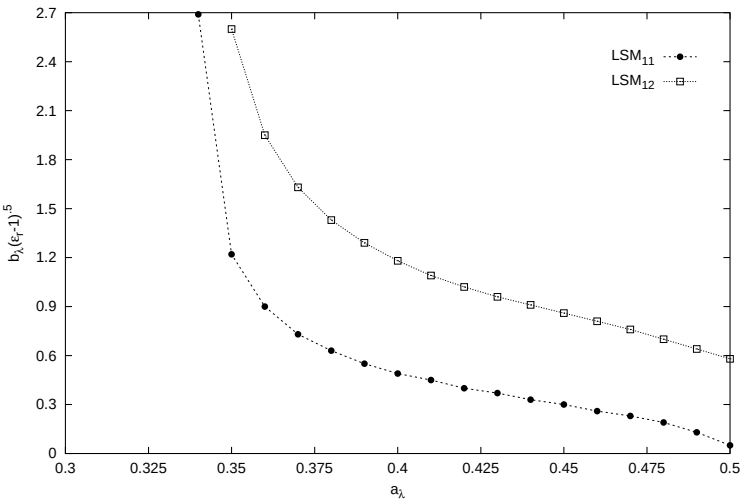

Figure 4.4: Operational diagram for NRD guide based on Teflon, $\epsilon_r = 2.04$.

larger frequency range for single mode operation, ϵ_r should be low. Thus

the propagation characteristics are enhanced by less costly low dielectric constant materials. Figure 4.4 shows the operational diagram for NRD guide with teflon ($\epsilon_r = 2.04$) as the dielectric material. It can be seen that LSM_{21} is absent throughout the operating region where $a_\lambda < 0.5$ resulting in a higher operational bandwidth. Thus we can conclude that the operational diagram is indispensable for selecting a material for implementing the NRD guide. Of the losses in the NRD guide, the dielectric losses are more predominant as most energy of the wave is concentrated in the dielectric region. Hence ideally loss tangent should be as small as possible. Conduction losses for the dominant LSM_{11} is very small since the electric field is predominantly parallel to the conducting plates.

4.2 Development of the transmission line model

The transmission line model of the NRD guide based multilayer structure (see Figure 4.1) is shown in Figure 4.5. As can be seen in the transmission line model, the slots have been efficiently described by two transformers and the self-impedance across the slot. For the development of the transmission line model of the structure, it is assumed that the dominant LSM_{11} is the propagating mode of the NRD guide. The transformation ratios of the slots, N_1 and N_2, can be found as the ratio of the modal voltage induced in the microstrip line and the NRD respectively to the slot voltage respectively. jX in Figure 4.5 account for stored energy at the slot due to higher order modes of the NRD guide.

The following electric field representation has been assumed in the slot for deriving the transformer ratios.

$$\bar{E}_s = \frac{V_0 \sin(k_a(\frac{L_s}{2} - |y|))}{W_s \sin(\frac{k_a L_s}{2})} \hat{y} \tag{4.4}$$

Where V_0 represents the voltage at the center of the slot. W_s and L_s are the width and length of the slot. The slot wave number (k_a) which is different from the free space wave number (k_0) can be derived applying the Cohn's method [27] modified to account for the presence of a conducting strip of the NRD guide at the distance H_N from the slot. This method is explained in appendix-D and section-3.1.

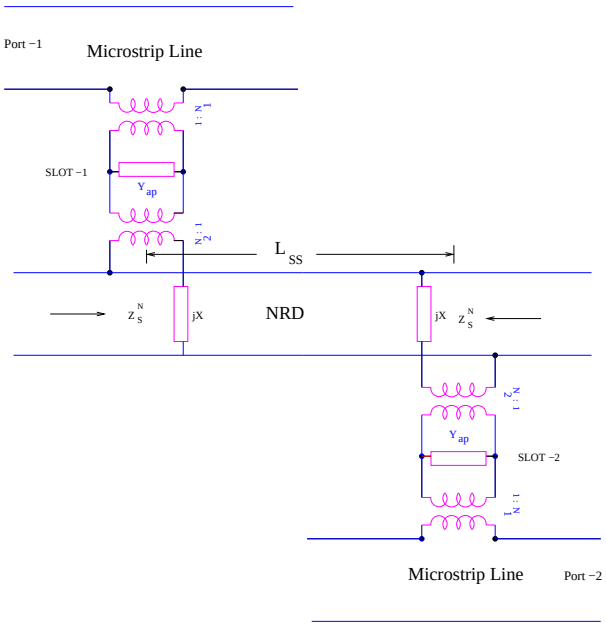

Figure 4.5: Equivalent network model of the NRD guide-microstrip line transition (see Figure 4.1).

Then transformer ratio from the slot to the NRD guide and from slot to the microstrip line can be found as follows,

$$N_g = \frac{V_g}{V_0} \tag{4.5}$$

where g=1 and 2 for the microstrip line and the NRD guide respectively. V_g represents the modal voltage induced in guide 'g ' which can be found by the following equation as,

$$V_g = \int\int_S \hat{n} \times \bar{E}_s \cdot \bar{h_w}\, dS \tag{4.6}$$

From the representation of the LSM_{11} fields in the case of the NRD guide (Appendix-A) and the representation of quasi TEM fields for the microstrip line the normalised modal magnetic field $\bar{h_w}$ can be determined satisfying the following normalization criteria,

$$\int\int_{S_g} \bar{e_N} \cdot \bar{e_N}\, dS_g = 1 \tag{4.7}$$

Here $\bar{e_N}$ represents the orthogonal electric modal vector in the coupled guide which is the NRD or the microstrip line. S_g denotes the guide crosssection. The transformation ratios can thus be derived as,

$$N_1 = \frac{\cos\left(k_a Ls/2 - k_a W_{eff}/2\right) - \cos\left(k_a L_s/2\right)}{W_s k_a \sqrt{W_{eff} h_M}\sin\left(k_a L_s/2\right)} \tag{4.8}$$

$$N_2 = \frac{4\pi k_a \sin\left(W_s \beta_{y1}/2\right)\left(\cos\left(\beta_{11} L_s/2\right) - \cos\left(k_a L_s/2\right)\right)}{TaW_s\beta_{11}\beta_{y1}\left({\beta_{11}}^2 - {k_a}^2\right)\cos\left(bbeta_{y1}/2\right)\sin\left(k_a L_s/2\right)} \tag{4.9}$$

As shown in Figure 1, h_M represents the height of the microstrip line substrate and b and a are the width and height of NRD guide. W_{eff} is the effective width of the microstrip line. T, which essentially is a normalization term can be derived as,

$$T = \sqrt{\frac{a(b\beta_{y1} + \sin(b\beta_{y1}))}{4\beta_{y1}\cos^2(b\beta_{y1}/2)} + \frac{{\epsilon_r}^2 a}{2\zeta_1}} \tag{4.10}$$

β_{y1} and ζ_1 represents the transverse wave numbers of the fundamental NRD mode satisfying the eigen system,

$$\beta_{y1}\tan\left(\frac{b\beta_{y1}}{2}\right) = \epsilon_r \zeta_1 \tag{4.11}$$

where β_{11}, the fundamental LSM_{11} mode propagation constant is given by,

$${\beta_{11}}^2 = \epsilon_r {k_0}^2 - {\zeta_1}^2 \tag{4.12}$$

The development of a transmission line model of two-layer aperture-coupled antenna in chapter 2 follow a similar analysis. Open ends of the NRD guide in the present analysis has been modeled as a perfect open, however for precise design of the structure using a transmission line model, the open ends may be analysed using the modal analysis as a transition from the LSM_{11}

mode to the parallel plate mode. For simplicity the higher order modes which account for the jX in the transmission line model (see Figure 4.5) are neglected in the analysis.

Finally, the input impedance of the structure can be written as,

$$Z_i = \left(\frac{Z_S^N \parallel Z_{SS}}{N_2^2} \parallel Z_{ap} \right) N_1^2 + Z_S^M \tag{4.13}$$

where,

$$Z_i \parallel Z_j = Z_i Z_j / (Z_i + Z_j) \tag{4.14}$$

Z_{ap} is the slot self impedance across the transformers and Z_{SS} is a function of the distance between the slots L_{SS}, (see Figure 4.5) as follows,

$$Z_{SS} = Z_0^N \frac{Z_T + j Z_0^N \tan(\beta_{11} L_{SS})}{Z_0^N + j Z_T \tan(\beta_{11} L_{SS})} \tag{4.15}$$

where Z_T is given by,

$$Z_T = \left(\frac{Z_S^M + Z_0^M}{N_1^2} \parallel Z_{ap} \right) N_2^2 \parallel Z_S^N \tag{4.16}$$

$Z_S^K, K = M, N$ represents the impedances provided by the microstrip ine stub and the NRD stub respectively at the center of the slot and $Z_0^K, K = M, N$ are their characteristic impedances.

As described in Chapter 2, slot self-impedance can be represented as the equivalent impedance of two parallel shorted slotlines with shorts at $\pm \frac{L_s}{2}$ from the center of the slot.

4.3 Results

The application of the NRD as shown in Figure 4.1 has been discussed in [54]. However the experimental analysis in this chapter focuses on NRD

plugs as depicted in Figure 4.2. The transmission line model of the NRD plug interconnect is essentially the same as the one for the geometry in Figure 4.1 with the distance between the slots taken to be zero. The dimensions of the NRD guide are (Figure 4.1 and 4.2) $b = 12$mm, $a = 12.7$mm. The NRD guide has been realized using substrate with a dielectric constant close to that of silicon ($\epsilon_r = 12$). The microstrip line has been implemented on Teflon substrate, $\epsilon_r = 2.52$). The NRD stub and microstrip line stubs are given by $L_N = 6$mm and $L_M = 8$mm. Slot dimensions are $W_s = 1.5mm$ and $L_s = 8$mm respectively. The coupling, S_{21} between the microstrip line and the NRD guide has been calculated using transmission line model and compared with experiments (see Figure 4.6). Since NRD guide is at cutoff below 4.9GHz we are not able to apply the transmission line model for the structure below 4.9GHz, however we can see from the experiment that the coupling cannot be neglected below 4.9 GHz. To study the behavior we have presented the results using TM parallel plate modes in connector assuming NRD is infinitely long along the slot and open $\pm b/2$ from the center of slot. It can be seen that the behavior of the calculated results agree well with experimental one.

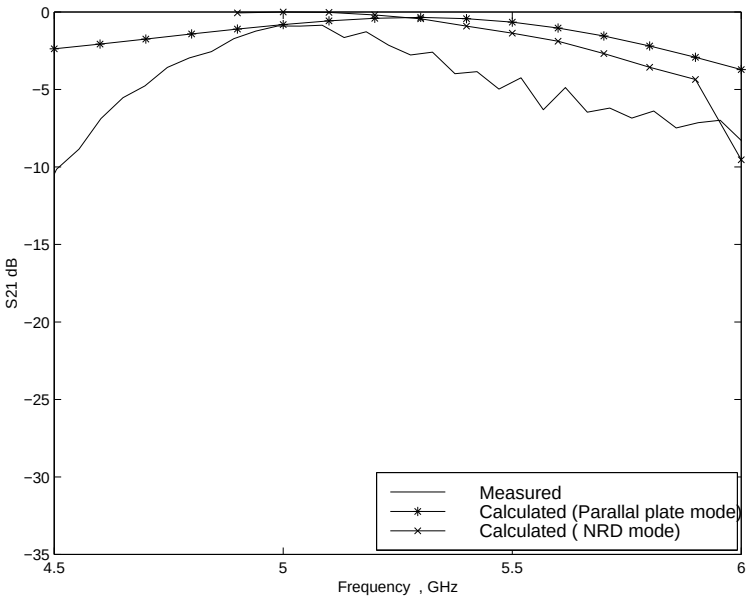

Figure 4.6: Results for the NRD interconnect seen in Fig. 3.

To efficiently utilise space, particularly between the ground planes, a new

way of using the dielectric interconnect is introduced, where a tail-ended tapered microstrip line has been used as the feed for the dielectric interconnect as shown in Figure 4.7. For this structure, the tapered line functions as

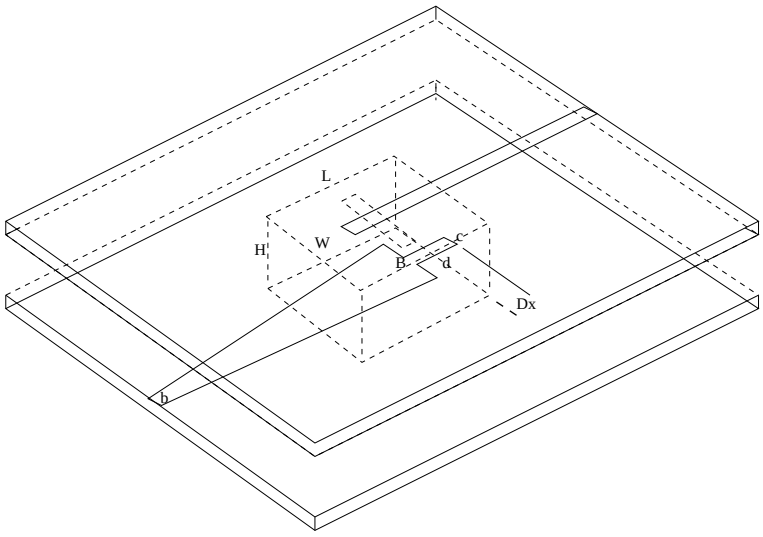

Figure 4.7: Microstrip-dielectric connector transition, Dielectric connector, W=12mm, H=12mm, L=16mm, Microstrip stub, line and substrate dimensions as same as in Fig. 3. Taper: b=2.26mm, B=10mm, Length =60mm, Tail: d=6.5mm, c=2.6mm.

an impedance transformer. Since the modes in the dielectric connector is no more nonradiative due to the absence of the second ground plane, there is a strong tendency for waves to propagate forward as in tapered line antennas thereby causing spurious radiation. The action of the tail is to efficiently prevent this radiation while at the same time providing the fringing fields necessary for coupling to the dielectric connector. The optimum position of the open end of the tail is at the connector end due to the fact that the maximum fringing field of open-ended microstrip line occurs at the air boundaries. In Figure 4.8, results of the tail ended tapered line fed connector is shown for various positions of the open end of the microstrip line. The signs + and - denotes the position of open end of the tail is outside and inside dielectric connector respectively. It can be seen that the optimum position of the tail is when $D_x = 0$ where the fringing fields are maximum and connector distance from fringing fields of open end is minimum. For $D_x < 0$ the high ϵ_r of the connector prevents fringing fields to be excited from tail, thus the coupling is less. For $D_x > 0$, even though the fringing

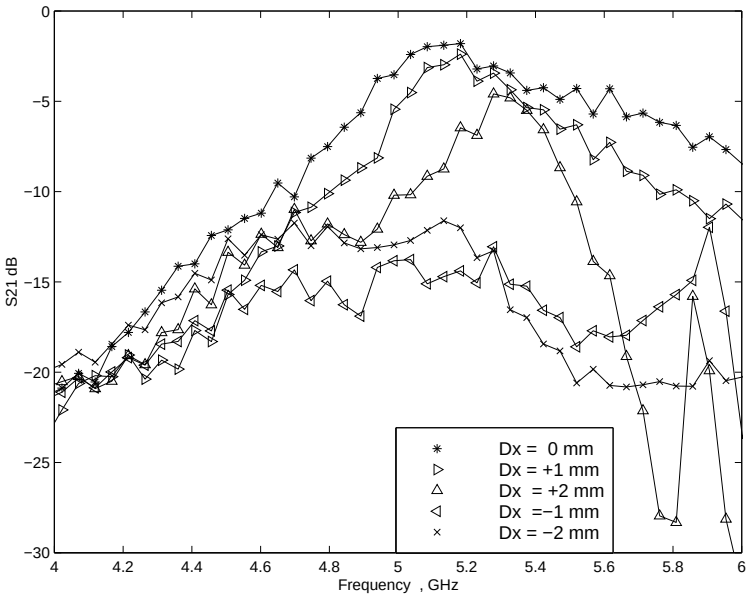

Figure 4.8: Dielectric connector fed by a tapered line with tail.

fields are stronger, the distance from the connector end prevents the fringing fields to couple to the NRD.

One of the critical requirements in using two or more NRD plugs is that there should be good isolation between different NRD plugs. Even though by theory the LSM/LSE modes are highly evanescent outside the NRD guide there has not been much effort in studying the finite ground effect on the characteristics of NRD guide and mismatches from transitions. In order to find an application for the NRD plugs at the same time studying the isolation between NRD plugs, a dual polarised antenna has been designed at 5.2 GHz (see Figure 4.9). The antenna uses an inset fed microstrip patch and two substrates. The experiment as shown in Figure 4.9 helps in studying the isolation between the NRD plugs. Figure 4.10 shows the measured return loss characteristics and isolation between the ports of the antenna. As can be seen from the diagram the return loss is well above 25dB at the tuning frequency. The isolation between the ports reduces from a low value and increases to about 13dB at the tuning frequency. This implies that isolation is affected more through the antenna rather than coupling between the NRD plugs itself.

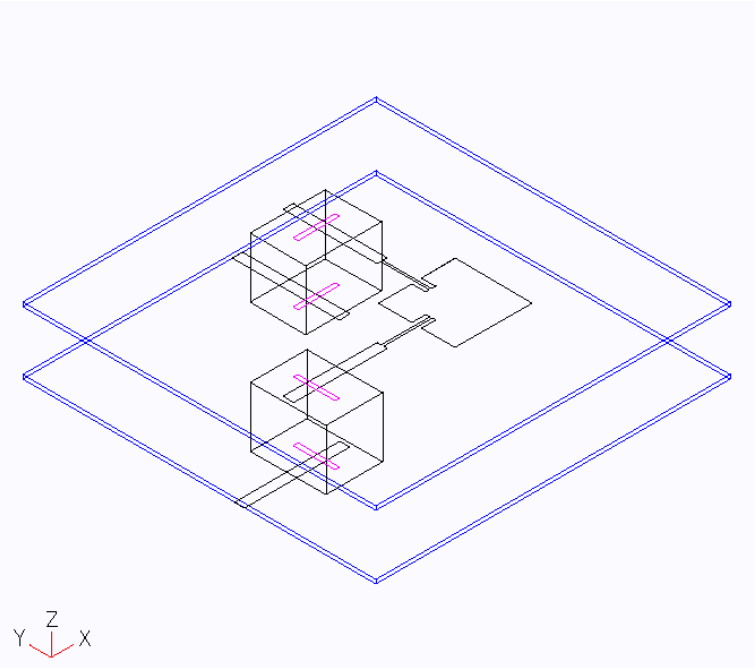

Figure 4.9: Dual polarised antenna using NRD plugs.

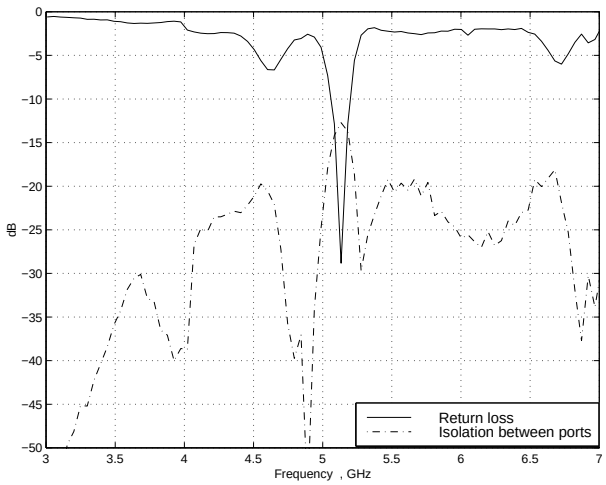

Figure 4.10: Return loss and isolation between the ports of antenna in Figure 4.10.

4.4 Conclusions

Two different dielectric connectors useful for multilayer RF integration has been considered in the paper. One such connector has been analysed using a simple transmission line model. The simulated results agree reasonably well with experiments. To further enhance the integration a novel tail ended tapered line feed has been introduced. A suitable explanation of its working concepts has been derived from experiments. To study typical isolation between different NRD plugs a dual polarised antenna has been implemented based on NRD plugs where it has been verified that the NRD plugs works well showing negligible coupling between different NRD plugs. Thus the experimental and simulated results of this chapter indicate that NRD guides can be an attractive option for passive structures not only for millimeter-wave frequency designs but also for complex designs at microwave ranges as well.

Appendix A

Spectral domain Green's functions for analysis of slots

Let $\tilde{G}(k_x, k_y)$ be the Fourier transform of a given Greeen's function $G(x, y)$. Then the spectral domain Greens function $\tilde{G}(k_x, k_y)$ and $G(x, y)$ are related by,

$$G(x,y) = \frac{1}{4\pi^2} \int_{kx=-\infty}^{\infty} \int_{ky=-\infty}^{\infty} \tilde{G}(k_x, k_y) e^{jk_x(x-x_0)} e^{jk_y(y-y_0)}\, dk_x\, dk_y \quad \text{(A.1)}$$

Green's function G_{yx}^{HJ} is defined as magnetic field component H_y at $(x, y, 0)$ due to a $\hat{x}$ directed electric currunt element at (x_0, y_0, d) where d is the thickness of the substrate of dielectric constant ϵ_r. $\tilde{G}_{yx}^{HJ}$ can be derived using (A.1) as,

$$\tilde{G}_{yx}^{HJ} = \frac{-jk_x^2(\epsilon_r - 1)\sin k_1 d}{T_e T_m} + \frac{k_1}{T_e} \quad \text{(A.2)}$$

Green's function G_{yy}^{HM} is defined as magnetic field component H_y at $(x, y, 0)$ due to a $\hat{y}$ directed magnetic current element (or $\hat{x}$ directed electric current element in a slot) at (x_0, y_0, d). $\tilde{G}_{yy}^{HM}$ can be derived using (A.1) as,

$$\tilde{G}_{yy}^{HM} = \frac{-j}{k_0 \eta_0} \left[\tilde{G}_{yy}^{HM(1)} + \tilde{G}_{yy}^{HM(2)} + \tilde{G}_{yy}^{HM(3)} \right] \quad \text{(A.3)}$$

where,

$$\tilde{G}_{yy}^{HM(1)} = \frac{j(k_1 \cos k_1 d + jk_2 \epsilon_r \sin k_1 d)(\epsilon_r k_0^2 - k_y^2)}{k_1 T_m} \quad \text{(A.4)}$$

$$\tilde{G}_{yy}^{HM(2)} = -\frac{jk_y^2 k_1(\epsilon_r - 1)}{T_e T_m} \tag{A.5}$$

$$\tilde{G}_{yy}^{HM(3)} = -\frac{(k_0^2 - k_y^2)}{jk_2} \tag{A.6}$$

where,

$$T_e = k_1 \cos k_1 d + jk_2 sin k_1 d \tag{A.7}$$

$$T_m = \epsilon_r k_2 \cos k_1 d + jk_1 \sin k_1 d \tag{A.8}$$

$$\beta^2 = k_x^2 + k_y^2, \qquad k_0 = 2\pi/\lambda_0, \qquad \eta_0 = \sqrt{\frac{\mu_0}{\epsilon_0}} \tag{A.9}$$

$$k_1^2 = \epsilon_r k_0^2 - \beta^2, \qquad k_2^2 = k_0^2 - \beta^2 \tag{A.10}$$

For $\beta^2 > \epsilon_r k_0^2$ and $\beta^2 > k_0^2$ then,

$$k_1 = -j\sqrt{\beta^2 - \epsilon_r k_0^2}, \qquad k_2 = -j\sqrt{\beta^2 - k_0^2} \tag{A.11}$$

Evaluation of integrals involving spectral domain Green's functions

Consider the integral,

$$I = \int_{k_x=-\infty}^{\infty} \int_{k_y=-\infty}^{k_y=\infty} F(k_x, k_y)\tilde{G}(k_x, k_y)\, dk_x\, dk_y \tag{A.12}$$

Substitute $k_x = \gamma\cos(\theta)$ and $k_y = \gamma\sin(\theta)$. Then,

$$I = \int_{\theta=0}^{2\pi} \int_{\gamma=0}^{\infty} F(\gamma, \theta)\tilde{G}(\gamma, \theta)\gamma\, d\gamma\, d\theta \tag{A.13}$$

The following case arise in the spectral domain analysis of slot,

$$I = \int_{\theta=0}^{2\pi} \int_{\gamma=0}^{\infty} \frac{N(\gamma, \theta)}{D(\gamma)}\, d\gamma\, d\theta \tag{A.14}$$

First we split the integrand into singular and nonsingular part. Numerical techniques can be applied to solve the non-singular part and analytical techniques can be applied to solve the singular part.

Singularity cases for the spectral domain analysis of slot are as follows:

Case1: Let $D(\gamma) = \sqrt{k_i^2 - \gamma^2}$ and consider the evaluation of following integral,

$$I = \int_{\theta=0}^{2\pi} \int_{\gamma=k_i-\delta}^{k_i+\delta} \frac{N(\gamma,\theta)}{\sqrt{k_i^2-\gamma^2}}\, d\gamma\, d\theta \tag{A.15}$$

Split the integral as

$$I = \int_{\theta=0}^{2\pi} \left[\int_{\gamma=k_i-\delta}^{k_i} \frac{N(\gamma,\theta)}{\sqrt{k_i^2-\gamma^2}}\, d\gamma\, d\theta + \int_{\gamma=k_i}^{k_i+\delta} \frac{jN(\gamma,\theta)}{\sqrt{\gamma^2-k_i^2}}\, d\gamma\, d\theta \right] \tag{A.16}$$

For removing the singularity, in the first part substitute $\gamma = k_i \sin(y)$ and in the second part substitute $\gamma = k_i + \sec(y)$. The resulting integrals are then adaptable for numerical evaluation.

Case2: Let $D(\gamma) = f(\gamma)$ and let there be a pole γ_0 in the limits of integration, $\gamma_0 - \delta$ to $\gamma_0 + \delta$. Let δ be very small.

To solve the integral apply Taylor series of $f(\gamma)$ at γ_0 and retain first non zero term then,

$$f(\gamma) = (\gamma - \gamma_0) f'(\gamma_0) \tag{A.17}$$

Now we use the following result from the theory of complex integration over the real axis pole in a half plane,

$$\int_{\gamma=\gamma_0-\delta}^{\gamma_0+\delta} \frac{F(\gamma)}{(\gamma-\gamma_0)f'(\gamma_0)} d\gamma = -\pi j \frac{F(\gamma_0)}{f'(\gamma_0)} \tag{A.18}$$

Appendix B

Analysis of Nonradiative Dielectric waveguide

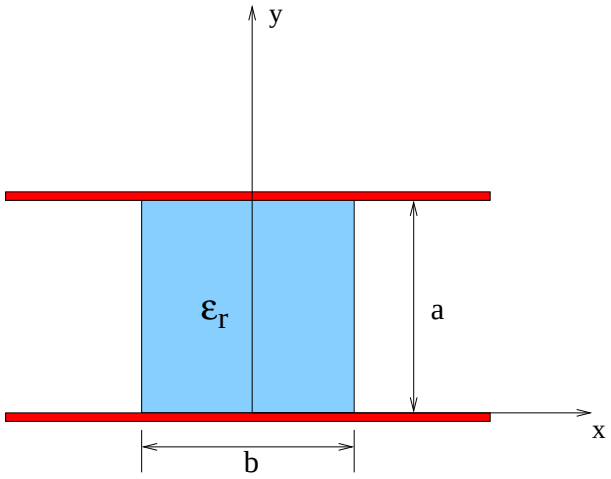

Figure B.1: Cross section of NRD guide.

Figure B.1 shows the cross section of NRD guide. Let $\mathbf{F}$ and $\mathbf{A}$ be the electric and magnetic potentials in a the region. Then $\mathbf{E} = -\nabla \times \mathbf{F}$ and $\mathbf{H} = \nabla \times \mathbf{A}$. Then from Maxwell's equations we can write,

$$\mathbf{E} = -\nabla \times \mathbf{F} - \mathrm{j}\omega\mu\mathbf{A} + \frac{\mathbf{1}}{\mathrm{j}\omega\epsilon}\nabla(\nabla \cdot \mathbf{A}) \tag{B.1}$$

$$\mathbf{H} = -\nabla \times \mathbf{A} - \mathbf{j}\omega\epsilon\mathbf{F} + \frac{\mathbf{1}}{\mathbf{j}\omega\mu}\nabla(\nabla \cdot \mathbf{F}) \tag{B.2}$$

The boundary conditions implies that the modes of the NRD guide to be considered are TM^y and TE^y modes. Pioneering paper in this field [49], refers to this modes as longitudinal-section magnetic (LSM) and longitudinal-section electric (LSE) modes.

LSM modes

For TM^y or LSM modes $\mathbf{F} = \mathbf{0}$ and $\mathbf{A} = \mathbf{j}\omega\epsilon_\mathbf{0}\phi^\mathbf{e}\hat{\mathbf{y}}$, where ϕ^e is the scalar potential function. Equations B.1 and B.2 reduces to,

$$\mathbf{E} = -\mathbf{j}\omega\mu_\mathbf{0}\mathbf{A} + \frac{\mathbf{1}}{\mathbf{j}\omega\epsilon}\nabla(\nabla \cdot \mathbf{A}) \tag{B.3}$$

$$\mathbf{H} = \nabla \times \mathbf{A} \tag{B.4}$$

The field components can be written in terms of scalar potential function as,

$$\begin{aligned}
E_x &= \frac{1}{\epsilon_r}\frac{\partial^2\phi^e}{\partial x \partial y} \\
E_y &= k_0^2\phi^e + \frac{1}{\epsilon_r}\frac{\partial^2\phi^e}{\partial y^2} \\
E_z &= \frac{1}{\epsilon_r}\frac{\partial^2\phi^e}{\partial y \partial z} \\
H_x &= -j\omega\epsilon_0\frac{\partial\phi^e}{\partial z} \\
H_y &= 0 \\
H_z &= j\omega\epsilon_0\frac{\partial\phi^e}{\partial x}
\end{aligned} \tag{B.5}$$

where, $k_0 = \omega\sqrt{\mu_0\epsilon_0}$ is the free space wave number.

LSM_{mn} symmetric modes

In this case,

$$\begin{aligned}
\phi^e &= A\sin(m\pi x/a)\cos(\beta_y y) && |y| < b/2 \\
&= A\cos(\beta_y b/2)\sin(m\pi x/a)e^{\zeta(b/2-|y|)} && |y| > b/2
\end{aligned} \tag{B.6}$$

The field has a $\cos(\beta_y y)$ variation along the cross-section hence the name symmetric mode. In the above equation A is an arbitrary constant, β_y is the y-directed propagation constant in the dielectric region, and ζ is the decay constant in the air region. For convenience the common factor $e^{j(\omega t-\beta z)}$ has been suppressed. The propagation parameters are related by,

$$\beta^2 = k_0^2\epsilon_r - (m\pi/a)^2 - \beta_y^2 = k_0^2 - (m\pi/a)^2 + \zeta^2 \tag{B.7}$$

where, β is the propagation constant of the wave.
The various field components are now given upon substitution in (B.5) as,

Dielectric region, $|y| < b/2$:

$$E_x = -A(\beta_y/\epsilon_r)(m\pi/a)\cos(m\pi x/a)\sin(\beta_y y) \tag{B.8}$$

$$E_y = -A(g^2/\epsilon_r)\sin(m\pi x/a)\cos(\beta_y y) \tag{B.9}$$

$$E_z = \pm jA(\beta_y/\epsilon_r)\beta\sin(m\pi x/a)\sin(\beta_y y) \tag{B.10}$$

$$H_x = -A\omega\epsilon_0\beta\sin(m\pi x/a)\cos(\beta_y y) \tag{B.11}$$

$$H_y = 0 \tag{B.12}$$

$$H_z = jA(\omega\epsilon_0)(m\pi/a)\cos(m\pi x/a)\cos(\beta_y y) \tag{B.13}$$

Air region, $|y| > b/2$:

$$E_x = \mp A\zeta(m\pi/a)\cos(m\pi x/a)\cos(\beta_y b/2)e^{\zeta(b/2-|y|)} \tag{B.14}$$

$$E_y = \pm Ag^2\sin(m\pi x/a)\cos(\beta_y b/2)e^{\zeta(b/2-|y|)} \tag{B.15}$$

$$E_z = \pm jA\beta\zeta\sin(m\pi x/a)\cos(\beta_y b/2)e^{\zeta(b/2-|y|)} \tag{B.16}$$

$$H_x = -A\omega\epsilon_0\beta\sin(m\pi x/a)\cos(\beta_y b/2)e^{\zeta(b/2-|y|)} \tag{B.17}$$

$$H_y = 0 \tag{B.18}$$

$$H_z = jA(\omega\epsilon_0)(m\pi/a)\cos(m\pi x/a)\cos(\beta_y b/2)e^{\zeta(b/2-|y|)} \tag{B.19}$$

upper and lower signs apply for air region in $\pm\hat{y}$ direction.
g is given by,

$$g^2 = \beta^2 + (m\pi/a)^2 = k_0^2\epsilon_r - \beta_y^2 = k_0^2 + \zeta^2 \tag{B.20}$$

Matching E_x at the air dielectric interface for the mn^{th} mode,

$$\beta_{yn}\tan\left(\frac{\beta_{yn}b}{2}\right) = \epsilon_r\zeta_n \tag{B.21}$$

where,

$$\begin{aligned} \zeta_n^2 &= k_0^2(\epsilon_r - 1) - \beta_{yn}^2 \\ \beta_{mn}^2 &= k_0^2\epsilon_r - (m\pi/a)^2 - \beta_{yn}^2 \end{aligned} \tag{B.22}$$

The modes are usually denoted by, $LSM_{m1}, LSM_{m3}, LSM_{m5}$.... The reference [49] refers to the above modes as LSM-even modes, denoted by, $LSM_{m0}, LSM_{m2}, LSM_{m4}$..... where $m = 1, 2...$

LSM_{mn} antisymmetric modes

In this case,

$$\begin{aligned} \phi^e &= B\sin(m\pi x/a)\sin(\beta_y y) && |y| < b/2 \\ &= +B\sin(m\pi x/a)\sin(\beta_y b/2)e^{\zeta(b/2-|y|)} && y > b/2 \\ &= -B\sin(m\pi x/a)\sin(\beta_y b/2)e^{\zeta(b/2-|y|)} && y < -b/2 \end{aligned} \tag{B.23}$$

The field has a $\sin(\beta_y y)$ variation along the crossection hence the name antisymmetric mode. The various field components are now given upon substitution in (B.5) as,

Dielectric region, $|y| < b/2$:

$$E_x = B(\beta_y/\epsilon_r)(m\pi/a)\cos(m\pi x/a)\cos(\beta_y y) \tag{B.24}$$

$$E_y = B(g^2/\epsilon_r)\sin(m\pi x/a)\sin(\beta_y y) \tag{B.25}$$

$$E_z = -jB(\beta_y/\epsilon_r)\beta\sin(m\pi x/a)\cos(\beta_y y) \tag{B.26}$$

$$H_x = -B\omega\epsilon_0\beta\sin(m\pi x/a)\sin(\beta_y y) \tag{B.27}$$

$$H_y = 0 \tag{B.28}$$

$$H_z = jB\omega\epsilon_0(m\pi/a)\cos(m\pi x/a)\sin(\beta_y y) \tag{B.29}$$

Air region, $|y| > b/2$:

$$E_x = -B\zeta(m\pi/a)\cos(m\pi x/a)\sin(\beta_y b/2)e^{\zeta(b/2-|y|)} \tag{B.30}$$

$$E_y = \pm Bg^2\sin(m\pi x/a)\sin(\beta_y b/2)e^{\zeta(b/2-|y|)} \tag{B.31}$$

$$E_z = jB\beta\zeta\sin(m\pi x/a)\sin(\beta_y b/2)e^{\zeta(b/2-|y|)} \tag{B.32}$$

$$H_x = \pm\omega\epsilon_0\beta\sin(m\pi x/a)\sin(\beta_y b/2)e^{\zeta(b/2-|y|)} \tag{B.33}$$

$$H_y = 0 \tag{B.34}$$

$$H_z = \mp B(\omega\epsilon_0)(m\pi/a)\cos(m\pi x/a)\sin(\beta_y b/2)e^{\zeta(b/2-|y|)} \tag{B.35}$$

In the above equations, upper and lower signs apply for air region in $\pm\hat{y}$ direction.
Matching E_x at the air dielectric interface for the mn^{th} mode,

$$\beta_{yn} \cot\left(\frac{\beta_{yn} b}{2}\right) = -\zeta_n \epsilon_r \tag{B.36}$$

where,

$$\begin{aligned} \zeta - n^2 &= k_0^2(\epsilon_r - 1) - \beta_{yn}^2 \\ \beta_{mn}^2 &= k_0^2 \epsilon_r - (m\pi/a)^2 - \beta_{yn}^2 \end{aligned} \tag{B.37}$$

The modes are usually denoted by, $LSM_{m2}, LSM_{m4}, LSM_{m6}$.....

The Reference [49] refers to the above modes as LSM-odd modes, denoted by, LSM_{m1}, LSM_{m3}.... where $m = 1, 2...$

LSE modes

For TE^y (LSE) modes $\mathbf{A} = \mathbf{0}$ and $\mathbf{F} = \mathbf{j}\omega\mu_\mathbf{0}\phi^\mathbf{h}\hat{\mathbf{y}}$, where ϕ^h is the scalar potential function. Equations B.1 and B.2 reduces to,

$$\mathbf{E} = -\nabla \times \mathbf{F} \tag{B.38}$$

$$\mathbf{H} = -\mathbf{j}\omega\epsilon\mathbf{F} + \frac{\mathbf{1}}{\mathbf{j}\omega\mu_\mathbf{0}} \nabla(\nabla \cdot \mathbf{F}) \tag{B.39}$$

The field components can be written in terms of scalar potential function as,

$$E_x = j\omega\mu_0 \frac{\partial \phi^h}{\partial z} \tag{B.40}$$

$$E_y = 0 \tag{B.41}$$

$$E_z = -j\omega\mu_0 \frac{\partial \phi^h}{\partial x} \tag{B.42}$$

$$H_x = \frac{\partial^2 \phi^h}{\partial x \partial y} \tag{B.43}$$

$$H_y = k_0^2 \epsilon_r \phi^h + \frac{\partial^2 \phi^h}{\partial y^2} \tag{B.44}$$

$$H_z = \frac{\partial^2 \phi^h}{\partial y \partial z} \tag{B.45}$$

$$\tag{B.46}$$

LSE_{mn} symmetric modes

In this case,

$$\begin{aligned} \phi^e &= C\cos(m\pi x/a)\cos(\beta_y y) && |y| < b/2 \\ &= C\cos(\beta_y b/2)\cos(m\pi x/a)e^{\zeta(b/2-|y|)} && |y| > b/2 \end{aligned} \tag{B.47}$$

The field has $\cos(\beta_y y)$ variation along the cross-section hence the name symmetric mode. The propagation parameters are related by,

$$\beta^2 = k_0^2\epsilon_r - (m\pi/a)^2 - \beta_y^2 = k_0^2 - (m\pi/a)^2 + \zeta^2 \tag{B.48}$$

The various field components are then given by,

Dielectric region, $|y| < b/2$:

$$E_x = C\omega\mu_0\beta\cos(m\pi x/a)\cos(\beta_y y) \tag{B.49}$$
$$E_y = 0 \tag{B.50}$$
$$E_z = jC\omega\mu_0(m\pi/a)\sin(m\pi x/a)\cos(\beta_y y) \tag{B.51}$$
$$H_x = C\beta_y(m\pi/a)\sin(m\pi x/a)\sin(\beta_y y) \tag{B.52}$$
$$H_y = Cg^2\cos(m\pi x/a)\cos(\beta_y y) \tag{B.53}$$
$$H_z = jC\beta_y\beta\cos(m\pi x/a)\sin(\beta_y y) \tag{B.54}$$

Air region, $|y| > b/2$:

$$E_x = C\omega\mu_0\beta\cos(m\pi x/a)\cos(\beta_y b/2)e^{\zeta(b/2-|y|)} \tag{B.55}$$
$$E_y = 0 \tag{B.56}$$
$$E_z = jC(\omega\mu_0)(m\pi/a)\sin(m\pi x/a)\cos(\beta_y b/2)e^{\zeta(b/2-|y|)} \tag{B.57}$$
$$H_x = \pm C\zeta(m\pi/a)\sin(m\pi x/a)\cos(\beta_y b/2)e^{\zeta(b/2-|y|)} \tag{B.58}$$
$$H_y = Cg^2\cos(m\pi x/a)\cos(\beta_y b/2)e^{\zeta(b/2-|y|)} \tag{B.59}$$
$$E_z = \pm jC\beta\zeta\cos(m\pi x/a)\cos(\beta_y b/2)e^{\zeta(b/2-|y|)} \tag{B.60}$$

$\pm$ apply for air region in $\pm\hat{y}$ direction.

g is given by,

$$g^2 = \beta^2 + (m\pi/a)^2 = k_0^2\epsilon_r - \beta_y^2 = k_0^2 + \zeta^2 \tag{B.61}$$

Matching E_x at the air dielectric interface for the mn^{th} mode,

$$\beta_{yn}\tan\left(\frac{\beta_{yn}b}{2}\right) = \zeta_n \tag{B.62}$$

where,

$$\begin{aligned} \zeta_n^2 &= k_0^2(\epsilon_r - 1) - \beta_{yn}^2 \\ \beta_{mn}^2 &= k_0^2\epsilon_r - (m\pi/a)^2 - \beta_{yn}^2 \end{aligned} \tag{B.63}$$

The modes are usually denoted by, $LSE_{m1}, LSE_{m3}, LSE_{m5}$.....
The reference [49] refers to the above modes as LSE-even modes, denoted by, $LSE_{m0}, LSEm2...$ where $m = 1, 2...$

LSE_{mn} antisymmetric modes

In this case,

$$\begin{aligned} \phi^e &= D\cos(m\pi x/a)\sin(\beta_y y) && |y| < b/2 \\ &= +D\cos(m\pi x/a)\sin(\beta_y b/2)e^{\zeta(b/2-|y|)} && y > b/2 \\ &= -D\cos(m\pi x/a)\sin(\beta_y b/2)e^{\zeta(b/2-|y|)} && y < -b/2 \end{aligned} \tag{B.64}$$

The field has a $\sin(\beta_y y)$ variation along the crossection hence the name antisymmetric mode. The various field components are then given by,
Dielectric region, $|y| < b/2$:

$$E_x = D\omega\mu_0\beta\cos(m\pi x/a)\sin(\beta_y y) \tag{B.65}$$
$$E_y = 0 \tag{B.66}$$
$$E_z = jD(\omega\mu_0)(m\pi/a)\sin(m\pi x/a)\sin(\beta_y y) \tag{B.67}$$
$$H_x = -D\beta_y(m\pi/a)\sin(m\pi x/a)\cos(\beta_y y) \tag{B.68}$$
$$H_y = Dg^2\cos(m\pi x/a)\sin(\beta_y y) \tag{B.69}$$
$$H_z = -jD\beta_y\beta\cos(m\pi x/a)\cos(\beta_y y) \tag{B.70}$$

Air region, $|y| > b/2$:

$$E_x = \pm D\omega\mu_0\beta\cos(m\pi x/a)\sin(\beta_y b/2)e^{\zeta(b/2-|y|)} \tag{B.71}$$
$$E_y = 0 \tag{B.72}$$
$$E_z = \pm jD(\omega\mu_0)(m\pi/a)\sin(m\pi x/a)\sin(\beta_y b/2)e^{\zeta(b/2-|y|)} \tag{B.73}$$
$$H_x = D\zeta(m\pi/a)\sin(m\pi x/a)\sin(\beta_y b/2)e^{\zeta(b/2-|y|)} \tag{B.74}$$
$$H_y = \pm Dg^2\cos(m\pi x/a)\sin(\beta_y b/2)e^{\zeta(b/2-|y|)} \tag{B.75}$$
$$H_z = jD\beta\zeta\cos(m\pi x/a)\sin(\beta_y b/2)e^{\zeta(b/2-|y|)} \tag{B.76}$$

In the above equations $\pm$ apply for air region in $\pm\hat{y}$ direction.
Matching H_x at the air dielectric interface for the mn^{th} mode,

$$\beta_{yn} \cot\left(\frac{\beta_{yn} b}{2}\right) = -\zeta_n \tag{B.77}$$

$$\begin{aligned} \zeta_n^2 &= k_0^2(\epsilon_r - 1) - \beta_{yn}^2 \\ \beta_{mn}^2 &= k_0^2 \epsilon_r - (m\pi/a)^2 - \beta_{yn}^2 \end{aligned} \tag{B.78}$$

The modes are usually denoted by, $LSE_{m2}, LSE_{m4}, LSE_{m6}$..... [49] refers to the above modes as LSE-odd modes, denoted by, $LSE_{m1}, LSE_{m3}, LSE_{m5}$..... where $m = 1, 2...$

Appendix C

Accurate CAD models for suspended substrate microstrip line

Consider the cross-section of suspended substrate microstrip line as shown in Figure C.1. From the spectral domain analysis and least square method

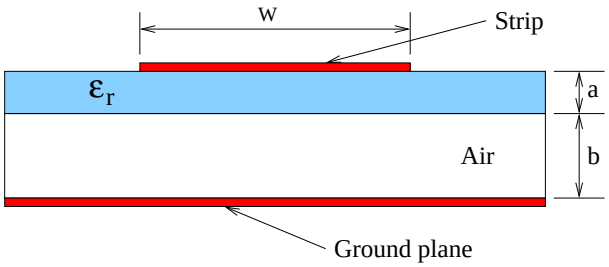

Figure C.1: Suspended-substrate micrfostrip line.

followed in [36], the effective ϵ_r of the suspended substrate microstrip line can be written as,

$$\epsilon_e = (1 - f_1 f_2)^{-1} \tag{C.1}$$

$$f_1 = 1 - \frac{1}{\sqrt{\epsilon_r}} \tag{C.2}$$

$$f_2 = \sum_{i=0}^{3} c_i \left(\frac{W}{b}\right)^i \tag{C.3}$$

$$c_i = \sum_{j=0}^{3} d_{ij} \left(\frac{b}{a}\right)^j \tag{C.4}$$

The polynomial coeffecients $d_{ij}, i = 0..3, j = 0..3$ are given as follows with $f = \ln \epsilon_r$.

$$\begin{aligned}
d_{00} &= (176.2576 - 43.1240f + 13.4094f^2 - 1.7010f^3)10^{-2} \\
d_{01} &= (4665.2320 - 1790.4f + 291.5858f^2 - 8.0888f^3)10^{-4} \\
d_{02} &= (-3025.5070 - 141.9368f - 3099.4700f^2 + 777.6151f^3)10^{-6} \\
d_{03} &= (2481.5690 + 1430.3860f + 10095.5500f^2 - 2599.1320f^3)10^{-8} \\
d_{10} &= (-1410.2050 + 149.9293f + 198.2892f^2 - 32.1679f^3)10^{-4} \\
d_{11} &= (2548.7910 + 1531.9310f - 1027.52f^2 + 138.4192f^3)10^{-4} \\
d_{12} &= (999.3135 - 4036.791f + 1762.4120f^2 - 298.0241f^3)10^{-6} \\
d_{13} &= (-1983.7890 + 8523.9290f - 5235.46f^2 + 1145.788f^3)10^{-8} \\
d_{20} &= (1954.0720 + 333.3873f - 700.7473f^2 + 121.3212f^3)10^{-5} \\
d_{21} &= (-3931.0900 - 1890.7190f + 1912.2660f^2 - 319.6794f^3)10^{-5} \\
d_{22} &= (-532.1326 + 7274.7210f - 4955.7380f^2 + 941.4134f^3)10^{-7} \\
d_{23} &= (138.2037 - 1412.4270f + 1184.27f^2 - 270.0047f^3)10^{-8} \\
d_{30} &= (-983.4028 - 255.1229f + 455.8729f^2 - 83.9468f^3)10^{-6} \\
d_{31} &= (1956.3170 + 779.9975f - 995.9494f^2 - 183.1957f^3)10^{-6} \\
d_{32} &= (62.855 - 3462.5f + 2909.9230f^2 + 614.7068f^3)10^{-8} \\
d_{33} &= (-32.2531 + 601.0291f - 643.0814f^2 + 161.2689f^3)10^{-9}
\end{aligned} \tag{C.5}$$

It has been proved that that the error of the above method is $< 6\%$ for the parameters: $1 \leq \epsilon_r \leq 20$, $.5 \leq \frac{W}{b} \leq 10$, $.06 \leq \frac{a}{b} \leq 1.5$

Appendix D

Transverse Resonance Technique for analysis of sandwich-slotline

The analysis follows a detailed study of [22][27] where we emphasise the derivations of the intermediate steps . Consider a slotline of width w sandwiched between two substrates of dielectric constants ϵ_{r1}, ϵ_{r2} and thicknesses d_1 and d_2. To make the analysis more general it is assumed that air filled gaps of heights h_1 and h_2 are present between the conducting strips and dielectrics. The widths of the conducting strips are b_1 and b_2 respectively. The geometry is shown in Figure D.1 where $\epsilon_i = \epsilon_{ri}\epsilon_0, i = 1, 2$. It is to

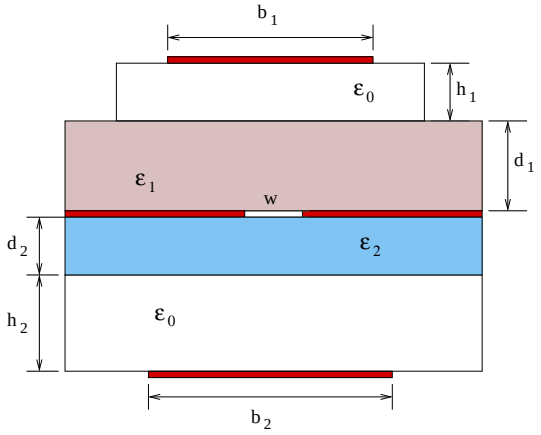

Figure D.1: Sandwich-slotline of width w between two dielectric substrates in the presence of parallel conducting strips of width b_1 and b_2.

be noted that the single substrate slotline is a special case of geometry in Figure D.1 with $b_1 = b_2 = d_2 = 0$.

In the application of the transverse resonance technique we notice that the electric fields along the slotline are periodically zero separated by half the slotline wave length. This means that two electric walls can be inserted perpendicular to the slots without disturbing the boundary conditions. In order to make the analysis simple (see Figure D.2), additional two walls are added on top and bottom separated by a distance b_1 and b_2. These walls can be of electric or magnetic type and the addition of these walls transforms the analysis into an analysis of the intersection of two rectangular waveguides. For convenience let a denote the distance between the side walls. The

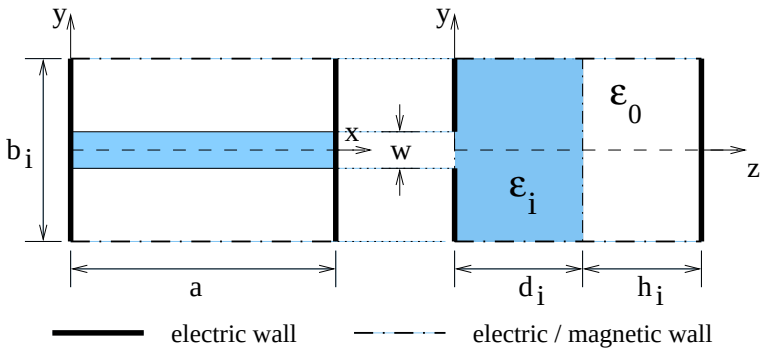

Figure D.2: The conversion of each half of the sandwich-slotline into a waveguide problem.

interpretation in terms of rectangular waveguides will simplify the slotline analysis but b_1 and b_2 has to be sufficiently large for accuracy.

The total suceptance at the slot plane ie. the junction between the two waveguides can be written as, $B_t = B_1 + B_2$. The slot wavelength can be derived from the transverse resonance condition ie. $B_t = 0$. Therefore we have to derive the expressions for B_1 and B_2. An approximation for B_i, $i = 1, 2$ is shown in Figure D.3, where B_i is the suceptance offered by the large guide $z \geq 0$ to the tiny air-filled waveguide, $z \leq 0$ of height w. Since $\delta_i = w/b_i$ is very small, we can approximate the only mode present in the tiny guide with TE_{10}. The application of the transverse resonance technique consists of three steps:

- The representation of electromagnetic fields in the two guides.

- The Matching of the fields in the slot plane by which the wave amplitudes in the large guide can be derived.
- Deriving an expression for B_i using the transmission line model.

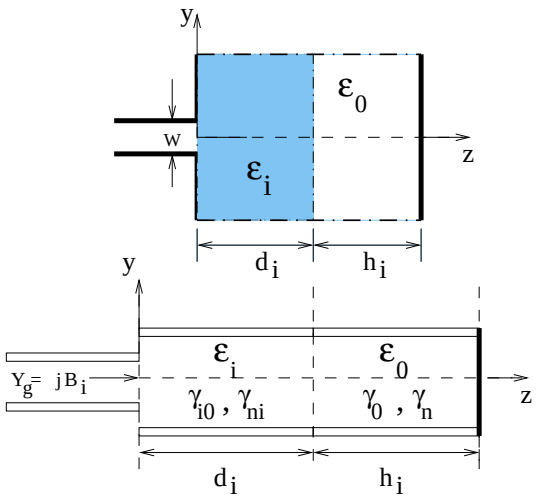

Figure D.3: The input suceptance of each half of the slotline seen by the TE_{10} mode in the guide of height w.

Representation of the fields

Consider the rectangular waveguide $z \geq 0$ (see Figure D.2). With the maximum electric field at $x = \frac{a}{2}$ for the slot and because of the symmetry the waveguide modes to be considered are $TE_{1,2n}$ and $TM_{1,2n}$, for magnetic walls at $y = \pm\frac{b}{2}$, where $n = \frac{1}{2}, \frac{3}{2}, \frac{5}{2}$.... In the case of electric walls at $y = \pm\frac{b}{2}$, the waveguide modes to be considered are TE_{10}, $TE_{1,2n}$ and $TM_{1,2n}$, $n = 1, 2, 3$... Thus the electric and magnetic fields (E_y and H_x) are proportional to $\sin\frac{\pi x}{a}\cos\frac{n\pi y}{b}$. This means that total fields at the slot plane, $z = 0$ for the large guide can be written as,

$$E_y = R_0 + \sum_{n>0} R_n \cos\frac{2n\pi y}{b_i} \tag{D.1}$$

$$H_x = y_{w0}R_0 + \sum_{n>0} y_{wn}R_n \cos\frac{2n\pi y}{b_i} \tag{D.2}$$

The wave admittances, y_{wn}, $n \geq 0$ can be written as,

$$y_{w0} = \left(\frac{H_x}{E_y}\right)_{TE_{1,0}} \tag{D.3}$$

$$y_{wn} = \left(\frac{(H_x)_{TE_{1,2n}} + (H_x)_{TM_{1,2n}}}{(E_y)_{TE_{1,2n}} + (E_y)_{TM_{1,2n}}}\right) \tag{D.4}$$

Now consider the tiny guide shown in Figure D.3. Since w is very small, the only mode present in the guide can be assumed to be TE_{10} whose fields at the slot center can be assumed as,

$$E_y^a = \begin{cases} C_0 & \text{for } |y| \leq w/2, \\ 0 & w/2 < |y| \leq b_i/2 \end{cases} \tag{D.5}$$

$$H_x^a = E_y y_w^{'} \tag{D.6}$$

Matching the fields at the slot plane

The matching of the electric fields of large guide (D.1) and tiny one (D.5) at the slot plane can be expressed as,

$$E_y^a = E_y = R_0 + \sum_{n>0} R_n \cos\frac{2n\pi y}{b_i} \tag{D.7}$$

The above equation has the form of a Fourier expansion. The coefficients R_0 and R_n can be readily written as,

$$R_0 = \int_{-w/2}^{w/2} C_0\, dy = C_0\delta_i \tag{D.8}$$

$$R_n = \frac{2C_0}{b_i}\int_{-w/2}^{w/2} \cos\frac{n\pi y}{b_i}\, dy = 2C_0\delta_i \frac{sin(n\pi\delta_i)}{n\pi\delta_i} \tag{D.9}$$

where, $\delta_i = w/b_i$. Similarly matching the magnetic fields of the large guide (D.2) and tiny one (D.6) at the slot plane,

$$C_0 y_w^{'} = y_{w0}R_0 + \sum_{n>0} y_{wn}R_n \cos\frac{2n\pi y}{b_i} \tag{D.10}$$

Integrating the above equation between the limits $y = \pm w/2$ and using (D.8) and (D.9) gives,

$$\frac{y_w^{'}}{\delta_i} = y_{w0} + 2\sum_{n>0} y_{wn}\left(\frac{sin(n\pi\delta_i)}{n\pi\delta_i}\right)^2 \tag{D.11}$$

Expression for the suceptance using the transmission line model

The input power P_i of the tiny guide can be written as,

$$P_i = \frac{1}{2}\int_{-w/2}^{w/2}\int_0^a E_y^a H_x^a \, dx \, dy = \frac{C_0^2 wa}{2} y_w^{'} \tag{D.12}$$

The guide admittance of the various modes can now be derived in terms of the wave admittances. Guide admittance of tiny guide Y_g in terms of the voltage, V can be written as,

$$Y_g = \frac{P_i}{V^2} \tag{D.13}$$

where,

$$V = \int_{-w/2}^{w/2} E_y^a \, dy = C_0 w \tag{D.14}$$

From(D.12) and (D.13) $y_w^{'}$ can be written as,

$$y_w^{'} = \frac{2w}{a} Y_g \tag{D.15}$$

Similarly the guide admittances of the large guide corresponding to wave admittances y_{w0} and y_{wn} becomes,

$$y_{w0} = \frac{2b_i}{a} Y_{g0} \tag{D.16}$$

$$y_{wn} = \frac{2b_i}{a} Y_{gn} \tag{D.17}$$

This means that (D.11) becomes,

$$Y_g = Y_{g0} + 2\sum_{n>0} Y_{gn} \left(\frac{sin(n\pi\delta_i)}{n\pi\delta_i}\right)^2 \tag{D.18}$$

Let the characteristic impedance of the TE_{10} mode in the dielectric filled guide be Y_{i0} and that of air filled waveguide be Y_0. For the case considered in [27] the air filled guide is assumed to be of infinite extent resulting in load impedance of the dielectric filled guide. But for the case considered here[28], (see Figure D.3), the load impedance of the dielectric filled guide becomes, $Y_0 \coth \gamma_0 h_i$. Thus, the guide admittance of the TE_{10} with load $Y_0 \coth \gamma_0 h_i$ can be written from transmission line formula as,

$$Y_{g0} = Y_{i0}\left[\frac{Y_0 \coth \gamma_0 h_i + Y_{i0} \tanh \gamma_{i0} d}{Y_{i0} + Y_0 \coth \gamma_0 h_i \tanh \gamma_{i0} d}\right] \tag{D.19}$$

where, γ_{i0} and γ_0 are the propagation constant of TE_{10} mode in the dielectric filled waveguide and air filled guide respectively.
Dividing the numerator and denominator by Y_{i0} (D.19) becomes,

$$Y_{g0} = Y_{i0}\left[\frac{\frac{Y_0}{Y_{i0}}\coth\gamma_0 h_i + \tanh\gamma_{i0}d}{1+\frac{Y_0}{Y_{i0}}\coth\gamma_0 h_i\tan\gamma_{i0}d}\right] \tag{D.20}$$

which can be modified as:

$$Y_{g0} = Y_{i0}\tanh\left(\gamma_{i0}d + \tanh^{-1}\frac{Y_0\coth(\gamma_0 h_i}{Y_{i0}}\right) \tag{D.21}$$

where

$$\gamma_0 = \frac{2\pi}{\lambda_0}\sqrt{1-\left(\frac{\lambda_0}{2a}\right)^2} \tag{D.22}$$

The wave impedances of the TE modes is related to the propagation constant as,

$$y_{w0} = \frac{\gamma_{i0}}{j\omega\mu} \tag{D.23}$$

Using (D.16) the characteristic admittance of the dielectric filled waveguide can be written as,

$$Y_{i0} = \frac{a}{2b_i}\frac{\gamma_{i0}}{j\omega\mu} \tag{D.24}$$

Substituting But $j\omega\mu = jk_0\eta_i$ with $\eta_i = \frac{120\pi}{\sqrt{\epsilon_{ri}}}$ in the above expression gives,

$$Y_{i0} = \frac{a}{2b_i}\frac{\gamma_{i0}}{j\eta k_0} \tag{D.25}$$

where the propagation constant, γ_{i0} is given by,

$$\gamma_{i0} = j\beta_{i0} = j\frac{2\pi}{\lambda_0}\sqrt{\epsilon_{ri}-\left(\frac{2\pi}{\lambda_0}\right)^2} = \frac{j2\pi}{\lambda_{gi0}} \tag{D.26}$$

Substituting $\epsilon_{ri} = 1$ in the above equations we get the expressions for the admittance of air filled waveguide,

$$Y_0 = \frac{a}{2b_i}\frac{\gamma_0}{j\omega\mu} \tag{D.27}$$

where

$$\gamma_0 = j\beta_0 = j\frac{2\pi}{\lambda_0}\sqrt{1-\left(\frac{2\pi}{\lambda_0}\right)^2} = \frac{a}{2b_i\eta}\frac{\lambda_0}{\lambda_{g0}} \tag{D.28}$$

Now consider the $TE_{1,2n}$ and $TM_{1,2n}$ modes. The field distribution of these modes are such that $E_x = 0$ at $z = 0$. By dividing the numerator and the denominator of (D.4) by $(E_y)_{TM_{1,2n}}$ and changing the notations from $TX_{1,2n}$ to TX_n, where $X = E, H$, we get,

$$\begin{aligned} Y_{wn} &= \left(\frac{\frac{(H_x)_{TE_n}}{(E_y)_{TE_n}} + \frac{(H_x)_{TM_n}}{(E_y)_{TM_n}}}{\frac{(E_y)_{TE_n}}{(E_y)_{TM_n}} + 1}\right) \\ &= \left(\frac{\frac{(H_x)_{TM_n}}{(E_y)_{TM_n}} + \frac{(H_x)_{TE_n}}{(E_y)_{TE_n}}\frac{(E_y)_{TE_n}}{EY_{TM_n}}}{\frac{(E_y)_{TE_n}}{(E_y)_{TM_n}} + 1}\right) \\ &= \frac{Y_{wTM_n} + D_n Y_{wTE_n}}{1 + D_n} \end{aligned} \tag{D.29}$$

where, $D_n = \frac{(E_y)_{TE_n}}{(E_y)_{TM_n}}$ when $(E_x)_{TM_n} + (E_x)_{TE_n} = 0$.
From the theory of rectangular waveguides the y components of the TE and TM electric fields are related by $D_n = \left(\frac{b}{2an}\right)^2$

Similar to (D.21) for the TE_{10} case, the expressions for the guide impedances for $TE_{1,2n}$ and $TM_{1,2n}$ are given by,

$$Y_{gTM_n} = Y_{iTM_n}\tanh\left(\gamma_{n_i}d_i + \tanh^{-1}\left[\frac{Y_{0TM_n}}{Y_{iTM_n}}\coth(\gamma_n h_i)\right]\right) \tag{D.30}$$

$$Y_{gTE_n} = Y_{iTE_n}\tanh\left(\gamma_{n_i}d_i + \coth^{-1}\left[\frac{Y_{0TE_n}}{Y_{iTE_n}}\coth(\gamma_n h_i)\right]\right) \tag{D.31}$$

where,

$$\gamma_n = \sqrt{\left(\frac{2n\pi}{b_i}\right)^2 + \left(\frac{\pi}{a}\right)^2 - \left(\frac{2\pi}{\lambda_0}\right)^2} \tag{D.32}$$

$$\gamma_{n_i} = \sqrt{\left(\frac{2n\pi}{b_i}\right)^2 + \left(\frac{\pi}{a}\right)^2 - \left(\epsilon_{ri}\frac{2\pi}{\lambda_0}\right)^2} \tag{D.33}$$

$$Y_{0TM_n} = \frac{a}{2b_i}\frac{jk_0}{\eta\gamma_n}, \qquad Y_{iTM_n} = \frac{a}{2b_i}\frac{jk_0\epsilon_{ri}}{\eta\gamma_{ni}} \tag{D.34}$$

$$Y_{0TE_n} = \frac{a}{2b_i}\frac{\gamma_n}{j\eta k_0}, \qquad Y_{iTE_n} = \frac{a}{2b_i}\frac{\gamma_{n_i}}{j\eta k_0} \tag{D.35}$$

(D.30) and (D.31) can be written as,

$$Y_{gTM_n} = \frac{jak_0\epsilon_{ri}}{2b_i\eta\gamma_{ni}} \tanh r_{ni} \tag{D.36}$$

$$Y_{gTE_n} = \frac{a\gamma_{ni}}{2jb_i\eta k_0} \coth q_{ni} \tag{D.37}$$

where,

$$r_{ni} = \gamma_{ni}d_i + \tanh^{-1}\left(\frac{\gamma_{ni}}{\gamma_n\epsilon_{ri}} \coth(\gamma_n h_i)\right) \tag{D.38}$$

$$q_{ni} = \gamma_{ni}d_i + \coth^{-1}\left(\frac{\gamma_n}{\gamma_{ni}} \coth(\gamma_n h_i)\right) \tag{D.39}$$

Substituting (D.38) and (D.39) in (D.29) we get,

$$\eta Y_{gn} = \frac{jak_0}{2b_i\gamma_{ni}} \frac{\epsilon_{ri}\tanh r_{ni} - \left(\frac{\gamma_{ni}b_i}{2ak_0n}\right)^2 \coth q_{ni}}{1 + \left(\frac{b_i}{2an}\right)^2} \tag{D.40}$$

Using (D.28) and (D.26) in (D.21) we get,

$$\eta Y_{g0} = \frac{a\lambda_0}{2b_i\lambda_{gi0}} \tanh\left(\frac{j2\pi d_i}{\lambda_{gi0}} + \tanh^{-1}\left[\frac{\lambda_{gi0}}{\lambda_0}\coth\gamma_0 h_i\right]\right) \tag{D.41}$$

Let $p = \frac{\lambda_0}{2a}$. Then (D.26) and (D.28) becomes,

$$\gamma_0 = jk_0\sqrt{1-p^2}, \qquad \gamma_{i0} = jk_0\sqrt{\epsilon_{ri}-p^2} \tag{D.42}$$

Let,

$$u_i = \sqrt{\epsilon_{ri}-p^2} = \frac{\lambda_0}{\lambda_{gi0}} \tag{D.43}$$

$$v = \sqrt{p^2}-1 = \frac{\gamma_0}{k_0} \tag{D.44}$$

$$F_{nni} = \frac{b_i\gamma_i}{2\pi n} = \sqrt{1+\left(\frac{b_i v}{2nap}\right)^2} \tag{D.45}$$

$$F_{ni} = \frac{b\gamma_{ni}}{2n\pi} = \sqrt{1-\left(\frac{b_i u_i}{2nap}\right)^2} \tag{D.46}$$

(D.40) and (D.41) can now be simplified as,

$$\eta Y_{gn} = \frac{j}{4p}\left(\frac{\epsilon_{ri}\tanh r_{ni} - p^2 F_{ni}^2 \coth q_{ni}}{\left[1+\left(\frac{b_i}{2an}\right)^2\right] nF_{ni}}\right) \tag{D.47}$$

$$\eta Y_{g0} = \frac{jau_i}{2b_i}\tan\left(\frac{\pi u_i d_i}{pa} - \tan^{-1}\left[\frac{v}{u_i}\coth(\gamma_0 h_i)\right]\right) \tag{D.48}$$

Using the last two expressions in (D.18) we get,

$$\begin{aligned} Y_g = \eta B_i =& \frac{au_i}{2b_i}\tan\left(\frac{\pi u_i d_i}{pa} - tan^{-1}\left[\frac{v\coth(vk_0h_i)}{u_i}\right]\right) \\ &+ \sum_{n>0}\frac{1}{2p}\left[\frac{\epsilon_{ri}\tanh r_{ni} - p^2F_{ni}^2\coth q_{ni}}{\left[1+\left(\frac{b_i}{2an}\right)^2\right]F_{ni}}\right]\frac{\sin^2(n\pi\delta_i)}{n\left(n\pi\delta_i\right)^2} \end{aligned} \tag{D.49}$$

where,

$$r_{ni} = \frac{2n\pi}{b_i}F_{ni}d_i + \tanh^{-1}\left[\frac{F_{ni}}{F_{nni}\epsilon_{ri}}\coth\left(\frac{n\pi}{b_i}F_{nni}h_i\right)\right] \tag{D.50}$$

$$q_{ni} = \frac{2n\pi}{b_i}F_{ni}d_i + \coth^{-1}\left[\frac{F_{nni}}{F_{ni}}\coth\left(\frac{n\pi}{b_i}F_{nni}h_i\right)\right] \tag{D.51}$$

For $\delta \to 0$ following approximations can be made,

$$\sum_{n=1,2..}\frac{\sin^2(n\pi\delta_i)}{n\left(n\pi\delta_i\right)^2} \approx \ln\frac{2}{\pi\delta_i} \tag{D.52}$$

$$\sum_{n=\frac{1}{2},\frac{3}{2}..}\frac{\sin^2(n\pi\delta_i)}{n\left(n\pi\delta_i\right)^2} \approx \ln\frac{8}{\pi\delta_i} \tag{D.53}$$

For the case of the magnetic walls at $y = \pm b_i/2$, the modes to be considered are $TE_{1,2n}$ and $TE_{1,2n}$, where $n = \frac{1}{2}, \frac{3}{2}, \frac{5}{2}...$
Equation (D.49) for magnetic wall case becomes,

$$\eta B_i = \sum_{n=\frac{1}{2},\frac{3}{2}..} \frac{1}{2p} \left[\frac{\epsilon_{ri} \tanh r_{ni} - p^2 F_{ni}^2 \coth q_{ni}}{1 + \frac{b_i}{2anF_{ni}}} \right] \frac{\sin^2(n\pi\delta_i)}{n\left(n\pi\delta_i\right)^2} \tag{D.54}$$

For the case of the electric walls at $y = \pm b_i$, the modes to be considered are $TE_{1,0}$, $TE_{1,2n}$ and $TE_{1,2n}$, where $n = 1, 2, 3....$ The equation (D.49) fo electric walls case then becomes,

$$\begin{aligned} \eta B_i =& \frac{au_i}{2b_i} \tan\left(\frac{\pi u_i d_i}{pa} - tan^{-1}\left[\frac{v \coth(vk_0h_i)}{u_i} \right] \right) \\ &+ \sum_{n=1,2,3..} \frac{1}{2p} \left[\frac{\epsilon_{ri} \tanh r_{ni} - p^2 F_{ni}^2 \coth q_{ni}}{\left[1 + \left(\frac{b_i}{2an}\right)^2\right] F_{ni}} \right] \frac{\sin^2(n\pi\delta_i)}{n\left(n\pi\delta_i\right)^2} \end{aligned} \tag{D.55}$$

For convenience the above equations can be written as,

$$\eta B_i = \frac{u_i^2}{2p} \ln \frac{8}{\pi d_i} + \frac{1}{2p} \sum_{n=\frac{1}{2},\frac{3}{2}..} M_{ni} \frac{\sin^2(n\pi\delta_i)}{n\left(n\pi\delta_i\right)^2} \text{ (magnetic wall case)} \tag{D.56}$$

$$\eta B_i = \frac{au_i}{2b_i} \tan\left(\frac{\pi u_i d_i}{pa} - \tan^{-1}\left[\frac{v \coth(vk_0h_i)}{u_i} \right] \right) + \frac{1}{2p} \sum_{n=1,2,3..} M_{ni} \frac{\sin^2(n\pi\delta_i)}{n\left(n\pi\delta_i\right)^2}$$

(electric wall case) (D.57)

If F_{ni}, (D.46) is real then M_{ni} is given by,

$$M_{ni} = \frac{\epsilon_{ri} \tanh r_{ni} - p^2 F_{ni}^2 \coth q_{ni}}{\left[1 + \left(\frac{b_i}{2an}\right)^2\right] F_{ni}} - u_i^2 \tag{D.58}$$

where,

$$r_{ni} = \frac{2n\pi}{b_i} F_{ni} d_i + \tanh^{-1}\left[\frac{F_{ni}}{F_{nni}\epsilon_{ri}} \coth\left(\frac{2n\pi}{b_i} F_{nni} h_i \right) \right] \tag{D.59}$$

$$q_{ni} = \frac{2n\pi}{b_i} F_{ni} d_i + \coth^{-1}\left[\frac{F_{nni}}{F_{ni}} \coth\left(\frac{2n\pi}{b_i} F_{nni} h_i \right) \right] \tag{D.60}$$

If F_{ni} is imaginary then,

$$M_{ni} = \frac{\epsilon_{ri} \tan r'_{ni} - p^2 |F_{ni}|^2 \coth q'_{ni}}{\left[1 + \left(\frac{b_i}{2an}\right)^2\right] |F_{ni}|} - u_i^2 \tag{D.61}$$

where,

$$r'_{ni} = \frac{2n\pi}{b_i} |F_{ni}| d_i + \tan^{-1}\left[\frac{|F_{ni}|}{F_{nni}\epsilon_{ri}} \coth\left(\frac{2n\pi}{b_i} F_{nni} h_i\right)\right] \tag{D.62}$$

$$q'_{ni} = \frac{2n\pi}{b_i} |F_{ni}| d_i + \cot^{-1}\left[\frac{F_{nni}}{|F_{ni}|} \coth\left(\frac{2n\pi}{b_i} F_{nni} h_i\right)\right] \tag{D.63}$$

The slotline wavelength is given by the transverse resonance condition when total suceptance is zero,

$$\eta B_t = \eta B_1 + \eta B_2 = 0 \tag{D.64}$$

Thus, to find the solution for λ_g we can solve (D.64) using an iterative procedure such as the Newton Raphson method. The characteristic impedance is then given by [27],

$$Z_c = 376.7 \frac{v}{v_g} \frac{\pi}{p} \frac{\triangle p}{\eta B_t} \tag{D.65}$$

where,

$$\frac{v}{v_g} = 1 + \frac{f}{\lambda_0/\lambda_g} \frac{\triangle(\lambda_0/\lambda_g)}{\triangle f} \tag{D.66}$$

If b_i is sufficiently large it can be seen that the electric wall case and magnetic wall case gives the same results.

Practical variations

Since for all practical cases electric and magnetic walls at $y = \pm\frac{b_i}{2}$ yields the same results (b_i large), for all practical cases we discuss only the magnetic wall case here after.

(1) Consider radiation boundary condition on one side of the slotline ($b_i =$

$0 = d_i = 0$ and $h_i = \infty$). This case has been previously been analyzed in [27]. ηB_i is them given by,

$$\eta B_i = \ln \frac{8}{\pi \delta_i} + \frac{1}{2p} \sum_{n=\frac{1}{2},\frac{3}{2}..} v_i^2 \left(1 - \frac{1}{F_{nni}}\right) \frac{\sin^2(n\pi\delta_i)}{n\left(n\pi\delta_i\right)^2} \tag{D.67}$$

(2) Consider the case when $h_i = \infty$ and $b_i = 0$. (Note that this case together with boundary condition of (1) on opposite sides of the slot resembles ordinary slotline [27]). The results are given as follows.

$$\eta B_i = \frac{1}{2p} \left(u_i^2 \ln \frac{8}{\pi \delta_i} + \sum_{n=\frac{1}{2},\frac{3}{2}..} M_{ni} \frac{\sin^2(n\pi\delta_i)}{n\left(n\pi\delta_i\right)^2} \right) \tag{D.68}$$

If F_{ni} is real then,

$$M_{ni} = \frac{\epsilon_{ri} \tanh r_{ni} - p^2 F_{ni}^2 \coth q_{ni}}{1 + \left(\frac{b_i}{2an}\right)^2 F_{ni}} - u_i^2 \tag{D.69}$$

$$r_{ni} = \frac{2n\pi}{b_i} F_{ni} d_i + \tanh^{-1} \left[\frac{F_{ni}}{F_{nni}\epsilon_{ri}}\right] \tag{D.70}$$

$$q_{ni} = \frac{2n\pi}{b_i} F_{ni} d_i + \coth^{-1} \left[\frac{F_{nni}}{F_{ni}}\right] \tag{D.71}$$

If F_{ni} is imaginary then,

$$M_{ni} = \frac{\epsilon_{ri} \tan r_{ni}^{'} - p^2 |F_{ni}|^2 \coth q_{ni}^{'}}{1 + \left(\frac{b_i}{2an}\right)^2 |F_{ni}|} - u_i^2 \tag{D.72}$$

where,

$$r_{ni}^{'} = \frac{2n\pi}{b_i} |F_{ni}| d_i + \tan^{-1} \frac{|F_{ni}|}{F_{nni}\epsilon_{ri}} \tag{D.73}$$

$$q_{ni}^{'} = \frac{2n\pi}{b_i} |F_{ni}| d_i + \cot^{-1} \frac{F_{nni}}{|F_{ni}|\epsilon_{ri}} \tag{D.74}$$

(3) Consider the case $h_i = 0$. This case has been studied in [28].

$$\eta B_i = \frac{1}{2p}\left(u_i^2 \ln\frac{8}{\pi\delta_i} + \sum_{n=\frac{1}{2},\frac{3}{2}..} M_{ni}\frac{\sin^2(n\pi\delta_i)}{n\left(n\pi\delta_i\right)^2}\right) \tag{D.75}$$

If F_{ni} is real then,

$$M_{ni} = u_i^2\left[\frac{\coth\left(\frac{2n\pi d_i F_{ni}}{b_i}\right)}{F_{ni}} - 1\right] \tag{D.76}$$

If F_{ni} is imaginary then,

$$M_{ni} = -u_i^2\left[\frac{\cot\left(\frac{2n\pi d_i |F_{ni}|}{b_i}\right)}{|F_{ni}|} + 1\right] \tag{D.77}$$

Appendix E

Selected publications

[1] Design of microwave amplifier using nonresonant slot matching

Dhanesh G-Kurup and Anders Rydberg
Electronics Letters, Vol.36, No 7, pp.602-603, March 2000

Abstract

A study into the application of nonresonant slots for impedance matching in microwave circuits is presented based on an evaluation of a low noise microwave transistor amplifier. Results show improved gain and noise figure characteristics for slot matched amplifier compared to microwave amplifier designed using transmission line stubs. Since the slots we propose appear in the ground plane of the active circuits, the size of the overall circuit is lower compared to that of an amplifier designed using transmission line stubs.

Introduction

The desire for integrated systems in which RF circuits including antenna are placed close together has increased the complexity of RF designs [1,2]. Active circuits such as amplifiers and oscillators are usually implemented using transmission line matching circuits which occupy a significant portion of the total area for the circuit. Other disadvantages of transmission line matching methods are its increased conductor and radiation losses at high

frequencies.

We propose slot matching as an alternative method to ameliorate some of the problems encountered in distributed matching circuits using transmission lines. Slots have been widely used in different passive microwave circuits such as the design of multilayer couplers, slot coupled antenna and waveguide transitions [3,4]. In [5,6] an analysis of the impedance transformation properties of slots was presented based on a transmission line model for slot coupled patch antenna. The results of [4] points to the fact that the resistance for a given reactance value of the slot impedance can be very low provided the slot is operated in the non-resonant region. Similar results for wide rectangular slots is reported in [7]. The low resistive part of the slot impedance at the operating frequency ensures minimum radiation losses. In the present work we utilize this property of slot in impedance matching of transistors. The design we consider is that of a low noise microwave transistor amplifier.

Design of low noise amplifier based on slot matching

A transverse rectangular slot in the ground plane of the microstrip line can be represented as an impedance in series with the micostrip line [4-6]. If the resistive part of the slot impedance at the operating frequency is very small, we can thus implement series reactance matching for circuits using slots. This is the principle of slot matching. It should be noted that for the usual transmission lines used such as microstrip lines, it is not possible to obtain a corresponding series stub matching. In the present work the series slot matching is implemented at the output and input for designing a low noise amplifier for operation at a frequency of 1GHz. The transistor used is ATF-10136 in a common source configuration [8] and the slots are etched in the ground plane of microstrip line. The layout representation of the transistor amplifier using slot matching is shown in Figure 2. Since the rectangular slot or I-slot is limited by the range of reactance values achievable in the non-resonant region, we instead considered L-slot and dog bone slots for matching the input and output respectively. Similar slots has been used for designing slot coupled antennas in [6].

The optimum dimensions of the slot were derived from the design criteria of the amplifier where a gain of 18dB at a noise-figure of 1.5dB was expected. The characterisation of the slots were done using a method of moments based CAD program [9]. The dembedded S-parameters of slot is

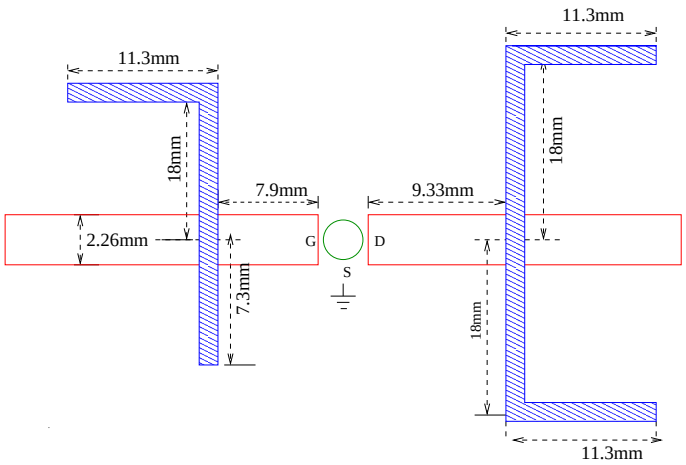

Figure E.1: Layout representation of the common source LNA (hatched portion is slots used for matching) width of slots=0.6mm, substrate:-Teflon, $\epsilon_r = 2.53, thickness = 0.8mm.$

then implemented in a microwave circuit simulator for the analysis of the amplifier.

Results

Figure E.2 shows the simulated results of the slot impedances used for the input and output matching. It can be seen that the resistance is very small at the operating frequency of 1GHz for both the slots. As has been discussed earlier this property ensures minimum radiation losses from the circuit.

To compare the performance of the slot based amplifier, a microstrip shunt stub matched amplifier was also designed for the same specifications. It is noted that overall size of the slot based amplifier is only about half that of traditional microstrip stub amplifier. Figure E.3 shows the comparison of performance of the LNA designed using slot matching and shunt stub matching. It can be seen from Figure E.3 that there is close agreement between simulated and experimental results of gain for the slot amplifier as well as the microstrip stub amplifier. It can also be seen that the bandwidth and noise-figure characteristics of slot amplifier are better than those of stub amplifier.

Conclusions

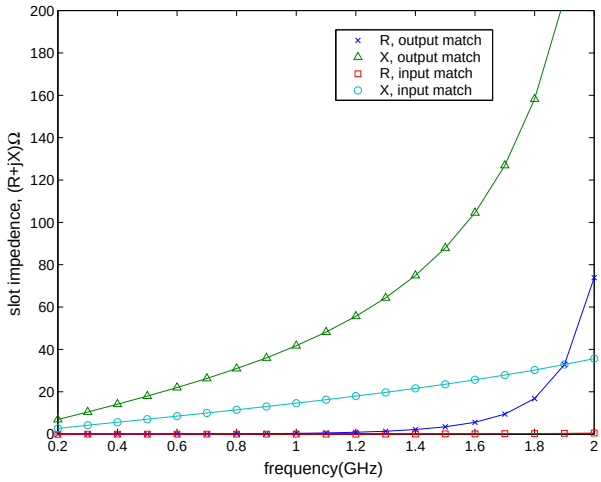

Figure E.2: Impedance of slots for input and output match as a function of frequency.

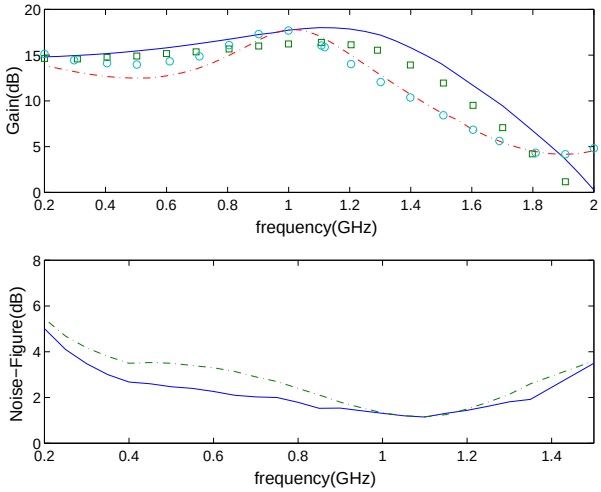

Figure E.3: Performance characteristics of LNA.: solid line:= slot amplifier (simulated), dashed line:= stub amplifier (simulated) , ∘ ∘:=stub amplifier (measured) and □ □:=slot amplifier (measured).

Low noise microwave amplifier designed based on slot matching has shown improved characteristics in terms of both gain and noise-figure. The matching technique is based on series addition of reactance compared to the usual

parallel stub matching using microstrip stubs. Since the resistance of slots is very small in the operating band the radiation losses are negligible. It is also seen that layout size of the slot amplifier is smaller in size than that of an equivalant microstrip stub matched amplifier.

Acknowledgement: The authors wish to acknowledge the research support of the Foundation for Strategic Research, Sweden through the Personal Computing and Communications program (PCC).

References

[1] J.Lin, T.Itoh, "Active integrated antennas" *IEEE Trans. in Microwave Theory and Techniques* Vol.-42, No 12 pp.2186-2194, Dec 1994.
[2] Howe.H, "Microwave integrated circuits- a historical perspective " *IEEE Trans. in Microwave Theory and Techniques* Vol.-32, pp.991-996, Sep 1984.
[3] J. S. Rao, K. K. Joshi, B. N, Das "Analysis of small aperture coupling between rectangular waveguide and microstrip line" *IEEE Trans. in Microwave Theory and Techniques* Vol.-29 pp 150-154, Feb 1981.
[4] D.M Pozar "Reciprocity method of analysis for printed slot and slot-coupled microstrip antennas" *IEEE Trans. Antennas and propagation* Vol.-34, pp.1439-1446, Dec.1986.
[5] M. Himdi , J. P. Daniel"Transmission line analysis of slot coupled microstrip antenna"*Electronic letters* Vol.-25, pp1229-1230,31 Aug 1989.
[6] M. El Yazidi, M.Himdi, J.P. Daniel, "Transmission line analysis of nonlinear slot coupled microstrip antenna"*Electronic letters* Vol.-28, pp1406-1408, 16 Aug 1992.
[7] Kahirizi, M., Sarkar, T. K. and Maricevic, Z. A., "Analysis of a Wide Radiating Slot in the Ground Plane of a Microstripline", *IEEE Trans. Microwave Theory and Techniques*, Vol.-41, pp.29-37, Jan 1993.
[8] Hewlett Packard, "*Communication Components Designer's Catalog*", 1997.
[9] *Momentum software*, Hewlett Packard, P.O. Box 10395, Palo Alto, CA 94303, USA.

[2] Dielectric Connectors for multilayered RF integration

Dhanesh G-Kurup and Anders Rydberg
Microwave and optical technology letters
Vol.23 No.4, pp. 230-233, November 1999

Abstract

Dielectric connectors for multilayered hybrid integration technology are considered in this paper. Design of one of the connectors which is working on Non Radiative Dielectric (NRD) waveguide mode has been carried out using a transmission line model. For this connector since the slots for the microstrip NRD guide coupling lie directly above one another, considerable space is released compared to traditional way of using NRD guide. To further enhance the integration, a novel way of feeding the dielectric connector using a tail ended tapered microstrip line has also been designed and tested.

Introduction

Renewed interest in millimeter wave range applications today stimulate researchers to seek new types of guided wave structures more suitable for integrated systems compared to conventional waveguides. Non radiative dielectric waveguide proposed by Yoneyama and Nishida [1] is an attractive transmission medium at these frequencies particularly because of its extremely low loss and low cost fabrication. The NRD waveguide has been used in the design of feed network for antennas [2] design of leaky wave antennas [3] and oscillators [4]. NRD guide based interconnects may be extremely useful for the obvious reason that it is non radiative compared with traditional interconnects which are radiative unless carefully designed and posing challenges to EMC. Also since the interconnect is three dimensional considerable space is released for mounting active components between different layers. One of the key problems in the design of active circuits involving NRD is the coupling of energy to and from the NRD waveguide. A hybrid integration technology proposed in [5] where NRD guide serves as an interconnect between two different layers is an attractive option for millimeter wave system designs. In the present work we propose a transmission line model for the design of NRD microstrip line transitions. The transmission line model has earlier been applied for fast analysis and design of antennas such as rectangular microstrip patch antennas and aperture coupled microstrip patch antennas [6] and [7]. Apart from being computationally

simple, transmission line model is also well adapted to active circuit simulators for system level optimization as the model basically consists of lumped electrical components.

Analysis

The transition between microstrip line and NRD guide is depicted in Figure 1. The transmission line model of the structure is shown in Fig.2. As can be seen in the transmission line model, the slots have been efficiently replaced by two transformers and the self impedance across the slot. For the develop-

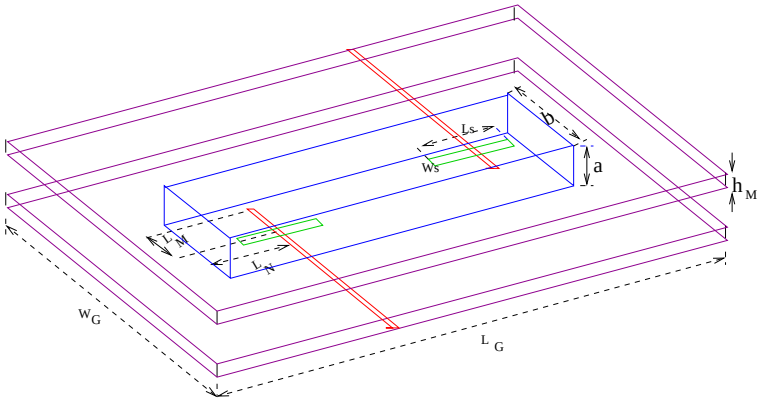

Figure E.4: NRD waveguide based multilayer structure.

ment of the transmission line model of the structure it is assumed that the dominant LSM_{10} is the propagating mode of NRD guide. Transformation ratios of the slots, N_1 and N_2 can be found as the ratio of modal voltage induced in microstrip line and NRD to slot voltage respectively. jX in Fig.2 account for stored energy at the slot due to higher order modes of NRD guide.
The following electric field representation has been assumed in the slot for deriving the transformer ratios.

$$\bar{E}_s = \frac{V_0 \sin(K_a(\frac{L_s}{2} - |y|))}{W_s \sin(\frac{K_a L_s}{2})}\hat{y} \tag{E.1}$$

Where V_0 represents the voltage at the center of the slot. W_s and L_s are the width and length of the slot. Slot wave number (K_a) which is different from free space wave number (K) can be found out applying the Cohn's method

[10] modified to account for the presence of a conducting strip of NRD guide at the distance H_N from slot [7].

Then transformer ratio from slot to NRD guide and from slot to mi-

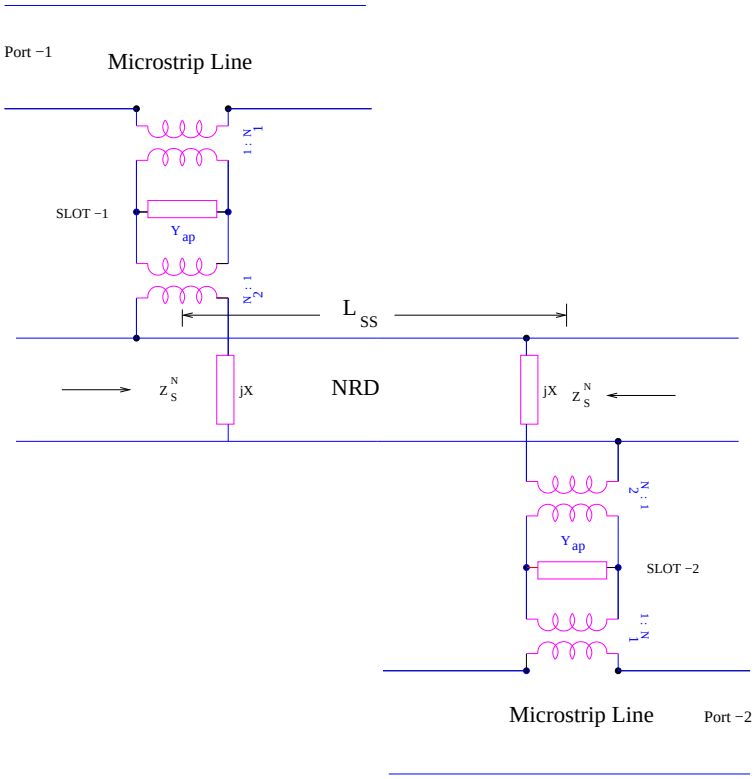

Figure E.5: Equivalent network model NRD guide - microstrip line transition of Figure 1.

crostripline can be found as follows,

$$N_g = \frac{V_g}{V_0} \tag{E.2}$$

where g=1 and 2 for microstrip line and NRD guide respectively. V_g represents the modal voltage induced in guide 'g ' which can be found by the following equation, [8].

$$V_g = \int\int_S \hat{n} \times \bar{E}_s \cdot \bar{h_w}\, dS \tag{E.3}$$

From the representation of LSM_{10} fields in the case of NRD guide [1] and representation of quasi TEM fields for microstrip line [9] the normalised modal magnetic field $\bar{h_w}$ can be determined satisfying the following normalization criteria,

$$\int\int_{S_g} \bar{e_N} \cdot \bar{e_N}\, dS_g = 1 \tag{E.4}$$

Here $\bar{e_N}$ represents the orthogonal electric modal vector in the coupled guide which is NRD or microstrip line. S_g denotes the guide cross section. The transformation ratios can thus be derived as,

$$N_1 = \frac{\cos\left(K_a Ls/2 - K_a W_{eff}/2\right) - \cos\left(K_a L_s/2\right)}{W_s K_a \sqrt{W_{eff} H_M} \sin\left(K_a L_s/2\right)} \tag{E.5}$$

$$N_2 = \frac{4\pi K_a \sin\left(W_s q_0/2\right)\left(\cos\left(\beta_0 L_s/2\right) - \cos\left(K_a L_s/2\right)\right)}{THW_s\beta_0 q_0\left({\beta_0}^2 - {K_a}^2\right)\cos\left(W q_0/2\right)\sin\left(K_a L_s/2\right)} \tag{E.6}$$

As shown in Fig.1. H_M represents the height of microstrip line substrate and W and H are the width and height of NRD guide. W_{eff} is the effective width of microstrip line. T which is essentially a normalization term that can be derived as,

$$T = \sqrt{\frac{H(Wq_0 + \sin(Wq_0))}{4q_0\cos^2(Wq_0/2)} + \frac{{\epsilon_r}^2 H}{2p_0}} \tag{E.7}$$

p_0 and q_0 represents the transverse wave numbers of fundamental NRD mode satisfying the eigen system [1],

$$q_0 \tan(Wq_0/2) = \epsilon_r p_0 \tag{E.8}$$

β_0 the fundamental LSM_{10} mode propagation constant is given by,

$${\beta_0}^2 = \epsilon_r {k_0}^2 - {q_0}^2 \tag{E.9}$$

A similar analysis can be found in the development of a transmission line model of two layer aperture coupled antenna,[7].

Open ends of the NRD guide in the present analysis has been modeled as a a perfect open, however for precise design of the structure using transmission line model, the open ends should be analysed using the Modal analysis as a transition from LSM_{10} mode to parallel plate mode.
Finally, the input impedance of the structure can be written as,

$$Z_i = \left(\frac{Z_S^N \parallel Z_{SS}}{N_2^2} \parallel Z_{ap} \right) N_1^2 + Z_S^M \tag{E.10}$$

where,

$$Z_i \parallel Z_j = Z_i Z_j / (Z_i + Z_j) \tag{E.11}$$

Z_{ap} is the slot self impedance across the transformers and Z_{SS} is a function of distance between the slots L_{SS}, (see Fig.1) as follows,

$$Z_{SS} = Z_0^N \frac{Z_T + j Z_0^N \tan(\beta_0 L_{SS})}{Z_0^N + j Z_T \tan(\beta_0 L_{SS})} \tag{E.12}$$

where Z_T is given by,

$$Z_T = \left(\frac{Z_S^M + Z_0^M}{N_1^2} \parallel Z_{ap} \right) N_2^2 \parallel Z_S^N \tag{E.13}$$

$Z_S^K, K = M, N$ represents the impedance provided by microstripline stub and NRD stub respectively at the center of slot and $Z_0^K, K = M, N$ are their characteristic impedances. As described in [7], slot self-impedance can be represented as the equivalent impedance of two parallel shorted slotted lines with shorts at $\pm \frac{L_s}{2}$ from the center of the slot.

Results

The application of the NRD as shown in Fig.1, has been discussed elsewhere,[5] and is not repeated here. To make space utilization most efficiently for integration applications, an interconnect directly between two slots may be more beneficial than the NRD interconnect shown in Fig.1. Geometry of such an NRD interconnect is shown in Fig.3. The transmission line model of this interconnect is essentially the same as the one for the geometry in Fig. 1 with distance between the slots taken to be zero. The dimensions

of NRD guide are, see Fig.1 $W = 12$mm, $H = 12.7$mm. The NRD guide has been realized using substrate with dielectric constant close to that of silicon ($\epsilon_r = 12$). Microstrip line has been implemented on Teflon substrate, $\epsilon_r = 2.52$). NRD stub and microstrip line stubs are respectively given by $L_N = 6$mm and $L_M = 8$mm. Slot dimensions are: $W_s = 1.5mm$ and $L_s = 8$mm, (see Fig.3). The coupling, S_{21} between the microstrip line and NRD guide has been calculated using transmission line model and compared with experiments, see Fig.4. Since NRD guide is at cutoff below 4.9GHz we are not able to apply the transmission line model for the structure below 4.9GHz, however we can see from the experiment that the coupling cannot be neglected below 4.9 GHz. To study the behavior we have presented the results using TM parallel plate modes in connector assuming NRD is infinitely long along the slot and open $\pm W/2$ from the center of slot (See Fig.1). It can be seen that the behavior of the calculated results agree well with experimental one.

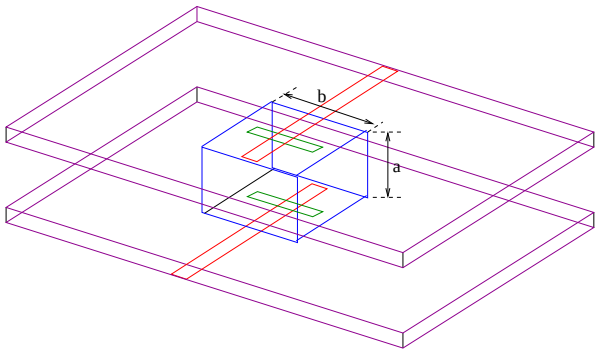

Figure E.6: NRD interconnect between multilayers.

The NRD guide as shown in Fig.1 and 3 is attractive for a number of reasons as described earlier. But to efficiently utilise space, particularly between the ground planes, a new way of using dielectric interconnect is introduced, where a tail ended tapered microstrip line has been used as the feed for the dielectric interconnect as shown in Fig.6. For this structure, the tapered line functions as an impedance transformer. Since the modes in the dielectric connector is no more nonradiative due to absence of the second ground plane, there is a strong tendency for waves to propagate forward as in tapered line antennas there by causing spurious radiation. The action of

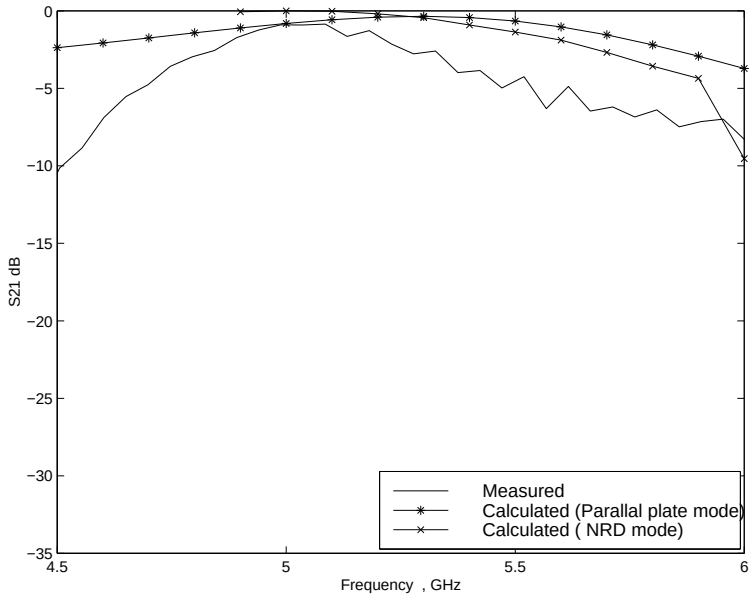

Figure E.7: Results for the NRD interconnect seen in Fig.3.

the tail is to efficiently prevent this radiation at the same time providing fringing fields necessary for coupling to the dielectric connector. The optimum position of the open end of the tail is at the connector end due to the fact that maximum fringing field of open ended microstrip line occurs at the air boundaries. In Fig.7 results of the tail ended tapered line fed connector (see Fig. 6) is shown for various positions of the open end of the microstrip line. The signs + and - denotes position of open end of the tail is outside and inside dielectric connector. It can be seen that the optimum position of the tail is when $D_x = 0$ where fringing fields are maximum and connector distance from fringing fields of open end is minimum. For $D_x < 0$ the high ϵ_r of the connector prevents fringing fields to be excited from tail, thus the coupling is less. For $D_x > 0$, even though the fringing fields are stronger, the distance from the connector end prevents the fringing fields to couple to the NRD.

Conclusions

Two different dielectric connectors useful for multilayer RF integration is considered in the paper. One such connector has been analysed using a simple transmission line model showing results that agree reasonably well

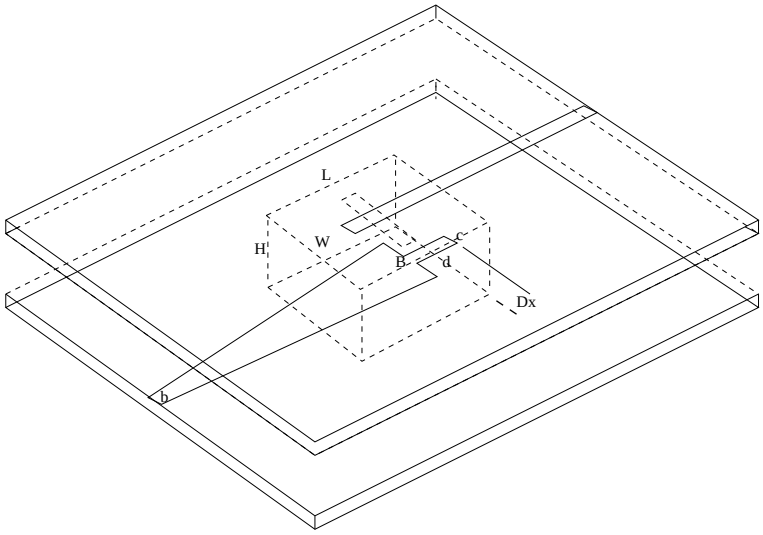

Figure E.8: Microstrip-dielectric connector transition, Dielectric connector, W=12mm, H=12mm, L=16mm, Microstrip stub, line and substrate dimensions as same as in Fig. 3. Taper: b=2.26mm, B=10mm, Length =60mm, Tail: d=6.5mm, c=2.6mm.

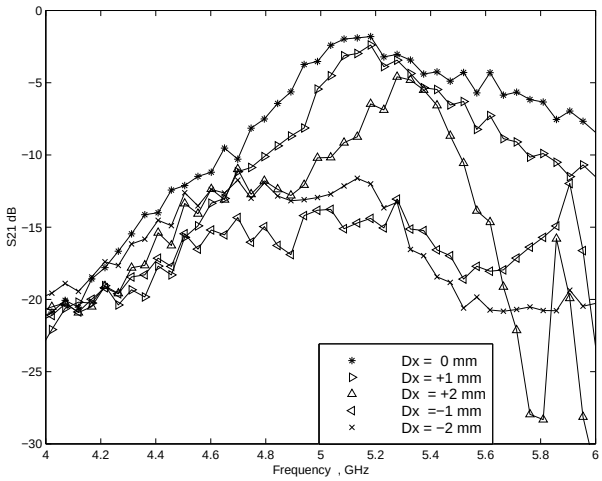

Figure E.9: Dielectric connector fed by a tapered line with tail.

with experiments. To further enhance the integration a novel tail ended tapered line feed has been introduced. A suitable explanation of its working concepts has been derived from experiments.

Acknowledgement

The authors wish to acknowledge the Foundation for Strategic Research through the program Personal Computing and Communications(PCC) for financial support.

References

[1] T. Yoneyama "Non radiative Dielectric Waveguides for millimeter wave integrated circuits" *IEEE Trans. in Microwave Theory and Techniques* Vol.-29 pp 1188-1192 , Nov 1981.
[2] C. J. Reddy, A Ittipiboon, A Cuhaci "Admitance Charecteristics of narrow radiating slots in NRD guide" *IEE Proceedings-H* Vol.-140, No 5, pp 407-413, Oct 1993.
[3] K. Maamria, T. Wagatsuma, T. Yoneyama "Leaky NRD guide as a feeder for Microwave Planar Antennas " *IEEE Trans. in Microwave Theory and Techniques* Vol.-41 pp 1680-1686, Dec 1993.
[4] K. Wu, L. Han "Integrated planar NRD Oscillator suitable for millimeter wave applications" *IEEE Microwave and guided wave letters* Vol.-6 pp 126-128 Sept 1996.
[5] K Wu, L. Han "Hybrid integration technology of planar circuits and NRD guide for cost effective Microwave and Millimeter wavde applications" *IEEE Trans. in Microwave Theory and Techniques* Vol.-45 pp 946-953, June 1997.
[6] H. Pues, A. Van de Capelle "Accurate transmission line model for rectangular microstrip antenna" *IEE Proceedings* Vol.-131 pp 334-340 , Dec 1984.
[7] M. Himdi , J. Daniel "Transmission line analysis of aperture coupled microstrip antenna" *Electronics letters* Vol.-25 pp 1229-1220 Aug 1989.
[8] J S Rao, B N Das "Impedence of off centered Strip Line fed series slot" *IEEE Trans. on Antennas and Propagation* Vol.-20 pp 893-895, Nov 1978.
[9] J. S. Rao, K. K. Joshi, B. N, Das "Analysis of small aperture coupling between rectangular waveguide and microstrip line" *IEEE Trans. in Microwave Theory and Techniques* Vol.-29 pp 150-154, Feb 1981.
[10] S. B. Cohn "Slotline on Dielectric Substrate" *IEEE Trans. Microwave Theory and Techniques* Vol.-17 pp 768-778 Oct 1969.
[11] M. Himdi , J. Daniel"Charecteristics of Sandwitch-slotline in front of a parallel microstrip" *Electronic letters* Vol.-27 pp 455-457 Feb 1991. 1996.

Bibliography

[1] Donald C. Cox, "Wireless personnel communications: What is it?," *IEEE Personnel Communications, Magazine*, vol. 2, pp. 20–35, April 1995.

[2] Randy H. Katz, "Adaptation and mobility in wireless information systems," *IEEE Personnel Communications, Magazine*, vol. 1, pp. 6–17, First Quarter 1994.

[3] M. Decina and V. Trecordi, "Convergence of telecommunications and computing to networking models for integrated services and applications," *Proceedings of the IEEE*, vol. 85, pp. 1887–1914, December 1997.

[4] V. Tralli O. Adrisano and R. Verdone, "Millimeter waves for short range multimedia communication systems," *Proceedings of the IEEE*, vol. 86, pp. 1383–1401, July 1998.

[5] Lal C. Godora, "Applications of antenna arrays in mobile communications, part 2: Beam forming and direction of arrival considerations," *Proceedings of the IEEE*, vol. 85, pp. 1195–1245, August 1997.

[6] Asad A. Abidi, "Low power radio frequency IC's for portable communications," *Proceedings of the IEEE*, vol. 83, pp. 544–569, April 1995.

[7] Stephen D. Gedney and Umesh Navsariwala, "A comparison of the performance of the finite difference time-domain, finite element time-domain, and planar generalized yee-algorithms on high performance parallel computers," *International Journal on Numerical Modeling (Electronic Networks, Devices and Fields)*, vol. 8, pp. 265–276, May 1995.

[8] J.Lin and T.Itoh, "Active integrated antennas," *IEEE Transactions on Microwave Theory and Techniques*, vol. 42, pp. 2186–2194, December 1994.

[9] T.Itoh A.Mortazawi and J.Harvey, editors, *Active Antennas and Quasi Optical Arrays*. New York: IEEE Press, 1998.

[10] Frank Demmerle and Werner Wiesbeck, "A biconical multi-beam antenna for spatial division multiple access," *IEEE Transactions on Antennas and Propagation*, vol. 46, pp. 782–787, June 1998.

[11] I. Bahl and Prakash Bhartia, editors, *Microwave solid state circuit design*: Wiley, 1988.

[12] H. Dave W.Y. Ali-Ahmad, G.M Rebeiz and G. Chin, "802GHz integrated horn antennas imaging array," *Int. J. Infrared and Millimeter Waves*, vol. 12, pp. 481–486, May 1991.

[13] A. Rydberg E. Öjefors, J. Lindblom and D.G.Kurup, "High gain micromachined slot coupled antenna for a 60GHz wireless LAN application," in *Cost 260 proceedings, Rennes, France*, October 1-3 2000.

[14] D.M Pozar and D.H Schaubert, editors, *Microstrip Antennas*. New York: IEEE Press, 1995.

[15] D.M Pozar, "Microstrip antenna aperture coupled to a microstrip line," *Electronics Letters*, vol. 21, pp. 49–50, January 1985.

[16] G.L. Creech Q.J. Zhang and Wright-Patterson, editors, *Special issue: Applications of Artificial Neural Networks to RF and Microwave Design*, vol. 9: Wiley, 1999.

[17] A. Van de Capelle H.Pues, "Accurate transmission line model for rectangular microstrip antenna," *IEEE Proceedings, Pt. H*, vol. 131, pp. 334–340, December 1984.

[18] A.G Derneryd, "A theoretical investigation of rectangular microstrip antenna element," *IEEE Transactions on Antennas and Propagation*, vol. 27, pp. 532–535, 1978.

[19] D.Thouroude M.Himdi and J.P Daniel, "CAD-oriented cavity model for rectangular patches," *Electronics Letters*, vol. 26, pp. 842–844, June 1990.

[20] Peter Lindberg, "Optimization of microstrip patch antennas using Genetic Algorithms," *Masters degree thesis, Signals and Systems, Uppsala University, Sweden*, September 2000.

[21] J.R James and P.S Hall, *Handbook of Microstrip antennas, Chapter 10.* London: IEE, 1989.

[22] M.Himdi, "Private correspondance,", 1999.

[23] N.H.L Koster and R.H Jansen, "The microstrip step discontinuity: A revised description," *IEEE Transactions on Microwave Theory and Techniques*, vol. 34, pp. 213–223, February 1986.

[24] K.J Webb Q. Xu and R. Mittra, "Study of model solution procedures for microstrip step discontinuities," *IEEE Transactions on Microwave Theory and Techniques*, vol. 37, pp. 381–387, February 1989.

[25] D. Solomon Y. Lo and W. Richards, "Theory and experiment of microstrip antennas," *IEEE Transactions on Antennas and Propagation*, vol. 27, pp. 137–145, January 1979.

[26] M.Himdi J.P Daniel and C.Terret, "Transmission line analysis of aperture coupled microstrip antenna," *Electronics Letters*, vol. 25, pp. 1229–1230, August 1989.

[27] S.B Cohn, "Slot line on a dielectric substrate," *IEEE Transactions on Microwave Theory and Techniques*, vol. 10, pp. 768–778, October 1969.

[28] M.Himdi and J.P Daniel, "Characteristics of sandwich-slotlines in front of parallel microstrip," *Electronics Letters*, vol. 27, pp. 455–457, February 1991.

[29] M.Himdi J.P Daniel and C.Terret, "Analysis of aperture coupled microistrip antenna using cavity method," *Electronics Letters*, vol. 25, pp. 391–392, March 1989.

[30] P.L Sullivan and D.H Schaubert, "Analysis of an apertureå coupled microstrip antenna," *IEEE Transactions on Antennas and Propagation*, vol. 34, pp. 977–984, August 1986.

[31] Jan Lindbolm and Erik Öjefors, "Micro-machined RF-components for a 60GHz wireless LAN," *Masters degree thesis, Signals and Systems, Uppsala University, Sweden*, May 2000.

[32] R. F. Drayton I. Papapolymerou and L. P. B. Katehi, "Micro-machined patch antennas," *IEEE Transactions on Microwave Theory and Techniques*, vol. 46, pp. 275–283, February 1998.

[33] P. Pramanik and P. Bhartia, "Computer-aided design models for millimeter-wave finlines and suspended-substrate microstrip lines," *IEEE Transactions on Microwave Theory and Techniques*, vol. 33, pp. 1429–1435, December 1985.

[34] P. Pramanik and P. Bhartia, "CAD models for millimeter-wave suspended substrate microstrip lines and finlines," *IEEE MTT-Symposium digest*, pp. 453–456, 1985.

[35] D.M Pozar, "Microwave engineering,", 1990.

[36] R.S Tomar and P. Bhartia, "New quasi-static models for the CAD of suspended and inverted microstrip lines," *IEEE Transactions on Microwave Theory and Techniques*, vol. 35, pp. 453–457, April 1987.

[37] M.El Yazidi M.Himdi and J.P Daniel, "Transmission line analysis of nonlinear slot coupled microstrip antenna," *Electronics Letters*, vol. 28, pp. 1406–1408, July 1992.

[38] S. Labonte L. Roy, M. Li and N. Simons, "Measurement techniques for integrated circuit slot antennas," *IEEE Transactions on Instrumentation and Measurement*, vol. 46, pp. 1000–1004, August 1997.

[39] R. F. Drayton and L. P. B. Katehi, "Development of self-packaged high-frequency circuits using micro-machining," *IEEE Transactions on Microwave Theory and Techniques*, vol. 43, pp. 2073–2080, September 1995.

[40] D.M Pozar, "Reciprocity method for analysis for printed slot and slot coupled microstrip antennas," *IEEE Transactions on Antennas and Propagation*, vol. 34, pp. 1439–1446, December 1986.

[41] Dhanesh G-Kurup and Anders Rydberg, "Design of microwave amplifier using non resonant slot matching," *Electronics Letters*, vol. 36, pp. 602–603, March 2000.

[42] T.K Sarkar M. Kahirizi and Z.A Maricevic, "Analysis of wide radiating slot in the ground plane of microstrip line," *IEEE Transactions on Microwave Theory and Techniques*, vol. 41, pp. 29–37, .. 1999.

[43] T.Itoh and R.Mittra, "Dispersion characteristics of slot lines," *Electronics Letters*, vol. 7, pp. 364–365, 1972.

[44] R. F. Drayton and L. P. B. Katehi, "Development of self-packaged high-frequency circuits using micro-machining," *IEEE Transactions on Microwave Theory and Techniques*, vol. 43, pp. 2073–2080, September 1995.

[45] D. Laurie R. Cools and L. Pluy, "A C++ package for automatic two-dimensional cubature," *ACM Trans. Math. Software*, vol. 23, pp. 1–15, 1997.

[46] M. Kisliuk A. Axelrod and J. Maoz, "Broadband microstrip-fed slot radiator," *Microwave Journal*, pp. 81–94, June 1989.

[47] Hewlett Packard, "Communication components designers catalog,", 1997.

[48] Hewlett Packard, "Momentum- method of moments based electromagnetic simulator,", 1998.

[49] T. Yoneyama, "Non radiative dielectric waveguides for millimeter wave integrated circuits," *IEEE Transactions on Microwave Theory and Techniques*, vol. 29, pp. 1188–1192, November 1981.

[50] A Cuhaci C.J Reddy, A. Ittipiboon, "Admittance characteristics of narrow radiating slots in NRD guide," *IEE Proceedings-H*, vol. 140, pp. 407–413, October 1993.

[51] T. Wagatsuma K. Maamria and T. Yoneyama, "Leaky NRD guide as a feeder for microwave planar antennas," *IEEE Transactions on Microwave Theory and Techniques*, vol. 41, pp. 1680–1686, December 1993.

[52] K. Wu and L. Han, "Integrated planar NRD oscillator suitable for millimeter wave applications," *IEEE Microwave and Guided wave letters*, vol. 6, pp. 126–128, September 1996.

[53] D. Dawn and M. Sachidananda, "Analysis and design of strip line to NRD guide transition," in *Proceedings of the third Asia Pacific Microwave Conference, In*, Tokyo, Japan, 1990, pp. 15–18.

[54] K. Wu and L. Han, "Hybrid integration technology of planar circuits and NRD guide for cost effective microwave and millimeter wave applications," *IEEE Transactions on Microwave Theory and Techniques*, vol. 45, pp. 946–953, June 1997.

[55] Dhanesh G-Kurup and Anders Rydberg, "Dielectric connectors for multilayered RF integration," *Microwave and Optical Technology Letters*, vol. 23, pp. 230–233, November 1999.